Imperial College London
Department of Grantham Institute of Climate Change

Solar Electricity from Concentrator Photovoltaic Systems

Ngai Lam Alvin Chan

April 2013

Submitted in part fulfilment of the requirements for the degree of
Doctor of Philosophy in Grantham Institute of Climate Change of
Imperial College London
and the Diploma of Imperial College London

I declare that all work contained in this thesis is my own, except in cases where works by others are clearly identified and fully sreferenced.

The copyright of this thesis rests with the author and is made available under a Creative Commons Attribution Non-Commercial No Derivatives licence. Researchers are free to copy, distribute or transmit the thesis on the condition that they attribute it, that they do not use it for commercial purposes and that they do not alter, transform or build upon it. For any reuse or redistribution, researchers must make clear to others the licence terms of this work.

Abstract

This thesis examines the prediction of concentrator photovoltaic system performance, and a model is presented where estimates are made using basic, fundamental material and atmospheric parameters, and successfully validated against measurements from a deployed system, to within 2% accuracy.

A method to characterise the impact of individual atmospheric parameters on concentrator photovoltaic system performance is detailed and results are presented for potential deployment locations around the globe, demonstrating substantial differences in energy yield prediction accuracy if insufficient information is available, with up to 75% relative difference in energy yield and levelised cost of energy between basic and detailed simulations. In addition, the competitiveness of concentrator photovoltaic systems in different locations are benchmarked against existing technologies, showing significant geographical variation in their financial viability.

The material quality in single and multijunction solar cells and its effect on the selection of optimal solar cell designs is investigated and the radiative efficiency of a device is proposed as a figure of merit to evaluate material quality. The optimal band gaps are shown to vary substantially depending on material quality at low solar concentrations, by hundred of milli-electron-volts, with ramifications for future solar cell designs.

The impact of photon management, through radiative coupling, on cell performance is quantified for current and future high efficiency multijunction solar cell structures. Up to 5% enhancement due to radiative coupling can be expected for quad-junction solar cells, but current designs can expect below 1% enhancement.

The work covered in this thesis has investigated and highlighted the po-

tential problems associated with not fully understanding the atmospheric conditions in which concentrator photovoltaic systems operate, providing evidence and impetus for additional ground measurements or a drastic improvement in satellite-based measurement of atmospheric conditions. By integrating atmospheric parameters into an existing concentrator photovoltaic system modelling tool, new methods to characterise these conditions has been developed rigorously and accurately simulate system behaviour, a valuable resource to the field.

In the design of optimal band gaps for multijunction solar cells, the work in this thesis shows that the material quality must be carefully considered in any design. A novel method has been developed to quantify material quality and provide a benchmark of state-of-the-art achieved values. The role of photon management in the form of radiative coupling is quantified, through the first examination of enhancement due to the effect, under realistic atmospheric conditions. This gives cell designers realistic expectations for performance enhancement.

Contents

List of Tables

List of Figures

1 Introduction

1.1 A Short History of Energy and Implications for the Climate

Access to energy is a key driver of growth, going back to the earliest human societies, where the collection of food, and the chemical energy stored within from photosynthetic processes, was converted to mechanical energy in the form of working muscles. Progressively, humans began to harness the energy in their surroundings with greater effectiveness, first with simple biomass fuels and using animate energy (domesticating animals and harnessing their potential for work, or using animal products), progressing to more processed biomass energy such as charcoal, the use of water and wind, and finally modern fossil fuels [1].

The discovery of fossil fuels and production of its related products (such as tar, plastics, lubricants) was crucial for rapid industrialisation, first with coal, and then oil and gas. These high energy density fuels allowed for access to new resources, products and markets, and enabled rapid travel around the globe, and underpin the current global economy. It is clear that fossil fuels will play a key role in the decades to come, as there are no clear substitutes for many oil-derivative products which are suitable and economical [1].

Since the industrial revolution the demand for and consumption of energy has increased year-on-year, linked to the rapid increase in global population. In many scenarios [2, 3] the world's human population will continue its rise for the foreseeable future, up to a peak of 10 billion in the worst-case scenario, indicating that the world's energy requirements will only increase [4].

The latest figures from the International Energy Agency [5] have shown a significant increase in world total primary energy consumption from 1971 to 2010, increasing from 6,107 MTOE (Millions Tonnes Oil Equivalent) to 12,717 MTOE. Specifically, electricity generation reached 20,132 Tera Watt-hours (TWh or 10^{12}Wh) in 2009 [6], with oil, gas, coal and peat generation making up 66.8% of this total, with almost all of the remainder provided by nuclear and hydro-electric power.

Formed by the heat and pressure over million of years in the Earth's crust, fossil fuels by their nature are non-renewable as the time required for their formation is many orders of magnitude greater than the usage time. Comprised of hydrocarbon chains, the use of these fuels emits carbon dioxide (CO_2) into the atmosphere, amongst other gases . There is unequivocal evidence to suggest that the emission of CO_2 [7] is responsible for a change in global climate, often presented as global warming, where the average global mean surface temperature has risen rapidly since the industrial revolution in the 19th Century, beyond the natural variation experienced in the past [8]. State-of-the-art climate models predict that unless our rate of increase in emission of green house gases - including methane, nitrogen dioxide and sulphur dioxide, but in particular carbon dioxide (CO_2) - is drastically reduced, large-scale, destructive and transformational changes to climates across the globe will take place, affecting our food supply, livelihoods and use of land [7]. The latest findings from the Intergovermental Panel on Climate Change show that electricity generation is the largest contributor to carbon dioxide emissions worldwide, at around 10 Gigatonnes per year [4].

There are two primary approaches to addressing the challenges resulting from climate change:

- **Mitigation** - actions taken to decrease the intensity of radiative forcing of the Earth due to anthropogenic factors, where radiative forcing is defined as the *"change in net (down minus up) irradiance (solar plus longwave; in W m2) at the tropopause after allowing for stratospheric temperatures to readjust to radiative equilibrium, but with surface and tropospheric temperatures and state held xed at the unperturbed values"* [4]. This is expected to result in reduced effects of global warming in both the short (by 2030) and long (post 2030) term. Practically this can take the form of improving the efficiency with which resources are used - reducing resource inputs and emissions per unit of output. Other methods include increasing the sinks for greenhouse gases through afforestation and improved management of existing forests. Key examples of short term mitigation range from switching to different fuels for energy generation to methods that sequester carbon in natural systems [4].

- **Adaptation** - policies implemented and actions taken to reduce the vulnerability of both natural and human systems to both current and expected climate change. Examples range from the design of crops better suited for changing climates to raising coastal and river flood defences [9].

1.2 Climate Change Mitigation - Energy Considerations

In order to address both the expected increase in demand for energy, in particular electricity, and the need to reduce CO_2 emissions globally, there have been three main types of mitigation solutions for energy proposed to date:

- **Energy Efficiency** - reduce energy demand for a given task or unit of output. This can take the form of building more energy efficient transportation, lighting and electronic devices, more efficient industrial processes and designing buildings that require less energy to heat and/or cool [4].
- **Carbon Capture and Sequestration** - capture the CO_2 emitted from combustion of fossil fuels and store them in appropriate storage facilities. This can be a natural underground cavern, or a cavity created by the extracting of fossil fuels, for example [10, 11].
- **Changing the Energy Supply** - decarbonising the energy used. For certain uses, such as electricity generation, fossil fuels can be replaced by renewable energy sources. By reducing the amount of CO_2 emitted per unit of energy used, the global CO_2 emission can in turn be lowered. The increased adoption of technologies such as electric vehicles,

when coupled with a lower carbon intensity grid, can further change the energy supply landscape [4].

Renewable energies include energy from illumination by the sun (Solar), movement of air across the Earth's surface (Wind), movement of water (Hydro, Tidal), temperature difference between the Earth's surface and its crust (Geothermal), use of plant material and products (Biomass). Nuclear is not included as a renewable energy, despite its occasional inclusion in other studies - the fuel is continuously being used up and cannot be replaced. For example, uranium is used in fission reactors, but cannot be generated at the same rate as it is depleted.

1.3 Solar Energy Conversion

Solar energy is attractive for several reasons - firstly, it is ubiquitous - all areas of the globe receive sunlight at some point during the year. Secondly, wind, hydro and biomass all require solar illumination as a pre-requisite - none of these energies would be available without sunlight, and the process of conversion incurs losses, thus reducing the theoretical potential of these energy sources [12]. It is therefore logical to attempt to convert the solar energy at the earliest opportunity possible, and ensure that it can be done so in as many locations as possible. On average, solar irradiance delivers $3.9\text{x}10^{24}$ Joules of energy to the Earth over the course of a year [13], enough to satisfy the planet's electricity demand of $7.7\text{x}10^{19}$ Joules many times over [5]. This illustrates the Sun's great potential as an energy source, provided suitable technologies are used to exploit it. The solar resource is highest in warm, arid regions such as deserts, with many locations suitable for adopting solar energy technologies [14].

There are two main types of conversion from solar energy to useful work - solar thermal and solar photovoltaics. Solar thermal conversion creates energy by increasing the temperature of a fluid using the sun's energy, and either using the liquid to transfer the heat directly to its application (heated water generation, for example) or to generate electricity, using a turbine in a similar fashion to a fossil fuel power plant. The underlying concept was first demonstrated in 1767 by Horace de Saussure, and there are modern versions of both application types [15,16].

Solar hot water heaters are are common sight in many communities across the world and are mounted on rooftops [17,18], whilst centralised solar thermal electricity generation plants, often referred to as Concentrating Solar Power (CSP) can be found in the Iberian peninsula and southwestern United States, with more in the planning process for similar locations [19]. These centralised plants use a large array of mirrors to reflect and concentrate sunlight onto a small area where a fluid is pumped through, with the heated fluid then converting water into steam to operate a turbine, which in turn generates electrical energy. An advantage of this approach is its use of turbines, a mature technology with many years of optimisation and refinement. This approach does require large volumes of feedwater to drive the turbines, with the latest CSP systems demonstrating overall solar-to-electric conversion efficiencies of around 20% [20].

The second example, solar photovoltaic conversion, from now on abbreviated as PV, is the direct generation of electricity from solar illumination with no intermediate steps. This involves the use of material which exhibits the photovoltaic effect, first observed by Alexandre-Edmond Becquerel in 1839 using a silver coated platinum electrode, in an electrolyte solution [21]. Later, the effect was also observed in selenium by Adams and Day in 1876 [22], with arguably the first large area solar cell produced by Fritts in 1894, by sandwiching selenium between gold and another metal [23].

By the 1950s, the discovery of a method to manufacture p-n junctions in silicon led to its widespread use in the electronics industry, but also prompted the development of the first silicon solar cell in 1954 with an efficiency of 6% by Chapin, Fuller and Pearson [24]. Despite their high cost (US$200 per Watt) the possibility of supplying power in remote locations was opened up, with the most obvious use being on satellites that had previously relied on other fuel sources. Throughout the latter half of the 20th Century, interest in photovoltaics was raised by political and economic events, such as the oil-crisis of the 1970s, but a sustained effort in the 2000s to increase the deployment of alternative energy generation technologies drove the cost of photovoltaics downwards and expanded production significantly. In performance terms, beginning from low initial solar to electric efficiencies of 6%, state-of-the-art silicon solar cells manufactured in laboratories have reached 25% efficiency [25], whilst most modules produced on a commercial scale offer conversion efficiencies of around 17% and can be found for close to USD$1 per Watt [26].

1.4 Silicon-based photovoltaics and alternative approaches

The first practical photovoltaic cell was developed in 1954 using silicon, and remains the most mature technology to date. Modern silicon solar cells are usually single junction devices, and can be classified as monocrystalline (high quality), multi crystalline (lower quality) or amorphous (low efficiency), each with its own distinctive manufacturing methods [27]. In 2010, silicon technologies made up 85% of global PV cell and module shipments, demonstrating its dominance in the market [28], due in part to relatively low cost, good material availability and technological maturity.

Despite its attractiveness, the efficiency limit for single junction solar cells [29] provides an upper ceiling to the performance that can be expected from silicon solar cells, and concerns regarding the availability of silicon feedstock and associated material availability remains an issue [30]. In response to these issues, a number of photovoltaic technologies exist today based on materials other than silicon, all looking to provide low-cost, renewable energy. Those that are in or near commercial production can be divided into the following categories:

- **High Efficiency** - using inorganic semiconductors with properties that allow for high absorption of the incoming solar spectrum. High conversion efficiencies can be achieved by using multiple materials in a single solar cell stack, called a multijunction solar cell, that absorbs in different parts of the solar spectrum and allows for increased power production. Each junction is usually a compound of some combination of Group III and Group V elements. The high conversion efficiency has led to adoption in space power systems, where weight is of paramount importance [31–33].

Due to their material composition and the recombination mechanisms involved, such devices also perform well under a large amount of sunlight. This can be achieved through the use of optical elements to collect sunlight from a large area and concentrate it onto a small solar cell. In terrestrial systems on Earth, high efficiency solar cells usually operate under concentrated sunlight and are referred to as concentrator photovoltaics (CPV), with notable exceptions [34].

- **Thin-films** - these solar cells are fabricated by depositing thin layers of active semiconductor material on a substrate [35], including amorphous and microcrystalline silicon [36], Cadium Telluride (CdTe) [37], Copper Indium Gallium diSelenide (CIGS) [38]. The more mature thin-film (CdTe) technologies have the advantage of lower cost, with efficiencies comparable to crystalline silicon, and have been observed to perform better under low-light conditions. Conventionally, these systems are operated under 1-sun concentration (i.e. no focal optics are present), and are referred to as "flat-plate" photovoltaic systems, like silicon.
- **Organic and Dye-Sensitised** - molecular or organic materials containing carbon are used to make flexible solar cells with a band gap that can be changed by varying the material composition. There is a large potential for low production cost in large volumes [39, 40]. The main challenge, particularly with organic solar cells, is ensuring performance stability is achieved over a sufficiently long period under illumination and minimising degradation [41, 42].

1.5 Motivations

In this thesis, the discussion focuses on the performance of concentrator photovoltaic systems, which provide a route to utility-scale production of electricity from the solar resource with potentially low cost.

One of the key factors that determines the success of a new energy generation system is the ability to predict the amount of output, and hence the cost of energy. There is currently insufficient awareness of how CPV systems will perform in regions with complex atmospheric conditions.

/hl The optimal design of the solar cells used in CPV systems do not accurately account for material quality, leading to deviations between expected and actual performance. The concept of using photon management techniques, to enhance solar cell and system performance has been investigated in the past on a theoretical and in laboratory testing. The potential enhancement that could results from realising these techniques have not been rigorously examined for designs that operate under realistic atmospheric conditions.

In light of this, in this thesis, the importance of controlling material quality in high efficiency solar cells is established and the implications for optimal solar cell designs are identified in Chapter 4. The response of concentrator photovoltaic system performance to varying atmospheric conditions is also examined, and a model is developed to predict performance from fundamental physical parameters in Chapter 5. In Chapter 6, the impact of atmospheric parameter knowledge on the cost of electricity is quantified for different locations, highlighting potential issues for wider deployment of CPV systems in places where atmospheric conditions vary significantly. The concept of enhancing power output by coupling light between junctions, which would normally be lost, is explored and the enhancement calculated for devices with practical material quality in Chapter 7.

2 Concentrator Photovoltaics and Atmospheric Effects

CPV differs from conventional PV systems by the inclusion of optical elements that focus the solar irradiance incident on an area to a significantly smaller area, concentrating the light. From a thermodynamic perspective, concentration reduces the Boltzmann loss (associated with an increase in entropy caused by an expansion of photon modes, related to the solid angles of emission and absorption) [43], observed in practice as a reduced drop in voltage from the theoretical value. Such an approach also leads to reduced use of semiconductor material - relatively inexpensive optics replace much of the area previously covered by active material. These systems in almost all instances track the position of the sun, to make full use of their focal optics and ensure maximum conversion efficiencies.

2.1 Solar Irradiance and Atmospheric Parameters

The solar radiation incident on the Earth before encountering the atmosphere is referred to as extraterrestrial irradiance, and can be calculated by the Planck approximation for a black body, but has also been measured by a variety of instruments, a review of which is given in [44]. The solar spectrum can be expressed as the distribution of the number of photons as a function of the photon energy, but more conventionally this is converted to the power density per unit wavelength (W/m^2/nm) as a function of wavelength (nm). Knowledge of the solar spectrum allows solar cell designers to determine the current generated in each junction of a solar cell, and a good understanding of the solar spectrum is crucial when considering cell design.

As the solar beam passes through the Earth's atmosphere, it can be transmitted, scattered or absorbed. Radiation that is transmitted directly to the observer is referred to as direct irradiance, whilst radiation that has undergone scattering is referred to as diffuse. Qualitatively, short wavelength radiation from the solar disk can be considered direct, and short wavelength radiation from other parts of the sky can be considered diffuse.

The transmission of solar radiation can be described by the Beer Lambert Bouger Law [45]:

$$I_\lambda = I_{0\lambda} e^{-AM(\tau_\lambda)} \tag{2.1}$$

where I_0 is the extraterrestrial irradiance, I is the irradiance incident on the photovoltaic system, AM is the air mass and τ is the total optical depth of the atmosphere. Air mass is defined in a later section. The subscript λ indicates the dependence on wavelength of the relevant quantities.

Over the wavelength range considered here the total optical depth of the atmosphere will consist of contributions from molecular scattering (so called Rayleigh scatter), aerosol, water vapour and other trace gases such as ozone. Under clear conditions, where clouds are absent and explicitly accounting for the effects of the various extinction processes on the atmospheric optical depth, the Beer Lambert Law becomes:

$$I_\lambda = I_{0\lambda} e^{-AM(\tau_{R\lambda}+\tau_{A\lambda}+\tau_{W\lambda}+\tau_{O\lambda}+\tau_{G\lambda})} \tag{2.2}$$

where τ_R, τ_A, τ_W, τ_O and τ_G are the optical depths associated with molecular scattering, aerosol, water vapour, ozone and other trace gases respectively and each of these quantities is a function of wavelength, λ .

CPV systems track the position of the sun in the sky - this is often referred to as 2-axis tracking - to ensure that the optics capture the maximum amount of sunlight available. Due to the use of concentrating focal optics, the acceptance angle is small, and hence only light from the solar disk is accepted. In all modern concentrator systems, the module is oriented such that its plane is always perpendicular, or normal, to the direction of incoming irradiance. Hence, the solar radiation accepted by CPV systems is referred to as *direct normal irradiance (DNI).*

An alternative measure of solar irradiance for photovoltaic systems is

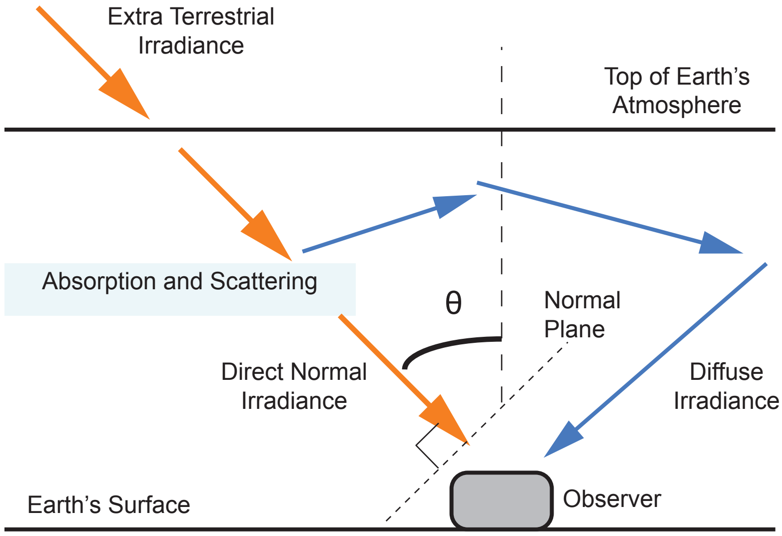

Figure 2.1: Diagram of Solar Geometry Relevant to CPV systems. Only Direct Normal Irradiance (DNI) is used in energy conversion, due to the use of focal optics.

given by the *Global Horiztonal Irradiance (GHI)* - this is a measure of all solar radiation incident on a horizontal plane on the Earth's surface, and is the sum of direct and diffuse irradiance incident on the horizontal plane. GHI is not relevant for calculations for CPV performance, but are commonly used for calculations with flat-plate photovoltaic systems. A graphical representation of the geometry is given in Figure 2.1.

By understanding the effect of atmospheric parameters highlighted in 2.2, one can estimate the solar spectrum given a certain set of atmospheric conditions, the prediction accuracy of the spectrally-resolved DNI spectrum is enhanced, providing better estimates for CPV system performance under operating conditions.

2.1.1 Air mass

Air mass is a way of expressing the pathlength of solar radiation through the Earth's atmosphere, and is a function of the solar zenith angle, itself a measure of the solar position. Air mass can be expressed as:

$$AM = \{cos\,(\theta) + a_1 \theta^{a_2}\,(a_3 - \theta)^{a_4}\}^{-1} \tag{2.3}$$

The equation has been taken from [46], where θ is the solar zenith angle, a_1 = 4.5665^{-1}, a_2 = 0.07, a_3 = 96.4836 and a_4 = -1.6970, where $a_{1,2,3,4}$ are fitting values that account for curvature of the Earth and refractive effects, and closely resemble older methods. An air mass of 1 (AM=1) implies the Sun is directly overhead, with a solar zenith angle of zero and typical atmospheric path length of 100km. Air mass zero is defined as extraterrestrial solar radiation that has not passed through the atmosphere.

The attenuation of DNI in clear and clean atmospheres, where there is an absence of clouds and aerosols, is primarily attributable to molecular scattering. Molecules are much smaller in size than the wavelength of the light, and Rayleigh scattering due to molecules can be described by:

$$I = I_0 \frac{8N\pi^2\alpha^2}{\lambda^4 R^2}\left(1 + cos^2\theta\right) \tag{2.4}$$

where N is the number of molecules, α the polarisability, R the distance between the observer and scattering, and θ the scattering angle. λ represents the wavelength of the radiation being examined, and from the λ^4 dependence is is clear that photons with shorter wavelengths will be more strongly attenuated than those with longer wavelengths. This attenuation depends strongly on its pathlength, represented by air mass - the longer the pathlength, the greater the attenuation. The calculation of Rayleigh scattering is well understood [47] and is implemented in all tools simulating solar spectra. A graphical example of the impact on spectral irradiance caused by a change in air mass is given in Figure 2.2 for reference conditions used in CPV performance rating, defined in Table 3.1.

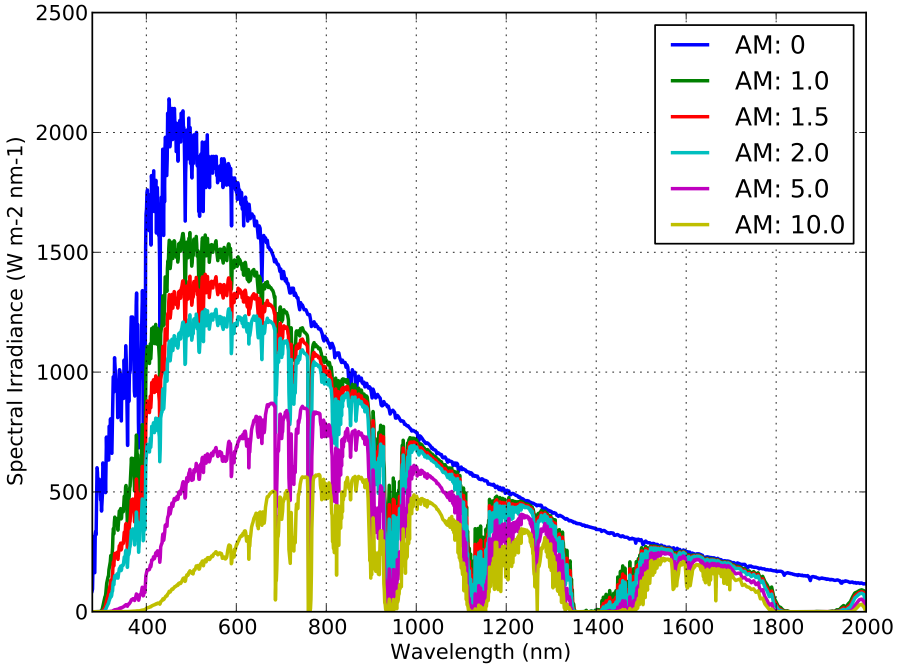

Figure 2.2: Direct Normal Irradiance as a function of air mass. Attenuation is strongest at shorter wavelengths. Spectra simulated using SMARTS v2.9.5, with AM1.5D reference conditions (specified in Table 3.1) for all variables other than air mass. Air mass zero spectrum is given by the ASTM E-490 standard [48]

2.1.2 Aerosols

Aerosols are particles or liquid droplets suspended in the air that absorb and scatter at a wide range of wavelengths. Although natural and anthropogenic aerosols often have different size distributions, consisting fine and coarse modes [49], they are much larger than the molecules considered in Rayleigh scattering and as such interact in a different fashion with solar radiation. The amount of aerosol present in the atmosphere is often referred to as the *aerosol loading*, and is expressed in 2.2, where the influence on DNI can be characterized by the aerosol optical depth (AOD) τ_A, the vertical integral of the extinction coefficient (absorption plus scattering) due to aerosols over the full atmospheric height.

The extinction of aerosols varies depending on the aerosol optical properties and the wavelength of light, and hence the aerosol optical depth must be known for all wavelengths relevant to the operation of a CPV system. In an ideal scenario, the AOD at all wavelengths would be measured by a spectroradiometer, but this capability is currently rarely available and expensive. Hence, AOD is measured for specific wavelengths, and the values for other wavelengths are calculated from these measurements. This can be achieved through use of the Angström Relation, detailed in Equation 2.5.

$$\tau_{\lambda_1}\lambda_1^{\alpha} = \tau_{\lambda_2}\lambda_2^{\alpha} \tag{2.5}$$

where τ is the aerosol optical depth, α the Angström Exponent, and λ_1, λ_2 denote two different wavelengths.

Depending on the size distribution of the aerosol particles, the attenuation due to aerosols can vary significantly with wavelength. This effect is captured by α - in general, the smaller the extinction Angström Exponent, the larger the aerosol particles, and vice versa. Large aerosol particles are usually associated with sea-salt and mineral dust, particularly relevant along coastlines and in deserts, whilst small aerosol particles are indicative of urban pollutants and biomass combustion [50]. In some radiative transfer codes, there is an option for selecting an aerosol *"model"* - this changes the Angström Exponent values, scattering direction and optical properties of the aerosols.

In Figure 2.3, the difference between simulated DNI spectra with significantly different aerosol loading is given.

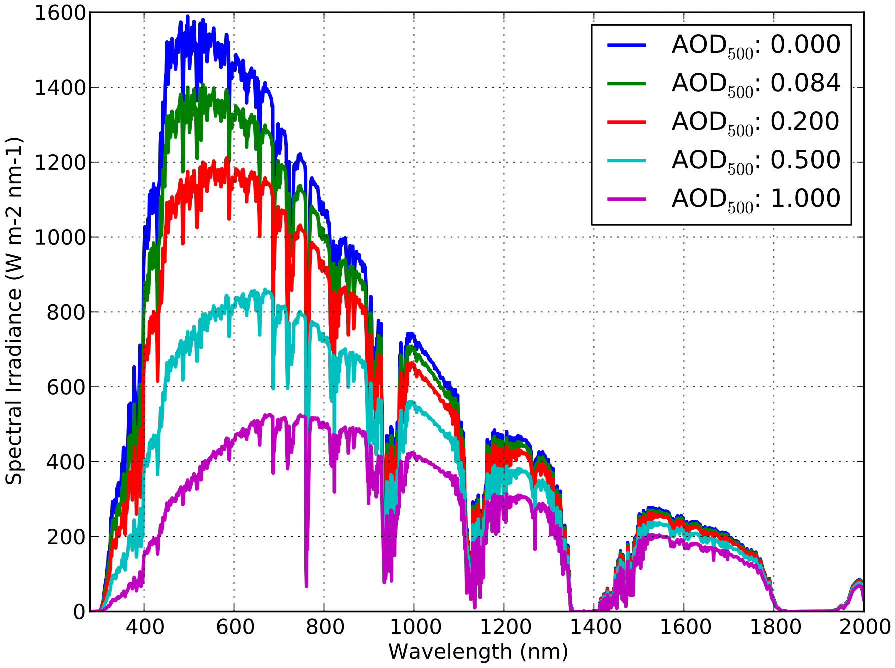

Figure 2.3: Direct Normal Irradiance as a function of aerosol optical depth. Spectra simulated using SMARTS v2.9.5, with AM1.5D reference conditions for all variables other than AOD, identified in Table 3.1. With the Angström Exponents under reference conditions, attenuation is strong at short wavelengths.

In areas of potential deployment for CPV systems, where the solar resource is high, significant differences exist in the aerosol loading [51]. In a later section, the differences in atmospheric parameters encountered at locations of interest is quantified and their impact on CPV performance is examined.

2.1.3 Precipitable Water

Precipitable water is the depth of water vapour that would be precipitated out at a given location from the full atmospheric column above the location. In the wavelength range relevant to multijunction solar cell performance, water vapour has absorption bands in the solar spectrum, centred on 960, 1100, 1400 and 1900nm [52]. The attenuation is highly dependent on wavelength and can be measured by spectroradiometers, which give a value for the integrated column water vapour but no information on how the distribution varies as a function of altitude. Alternatively a radiosonde can be used, where the water vapour profile is measured as a function of altitude and transmitted to a computer on the ground, after being launched vertically in a balloon. The recorded water vapour profile can then be integrated to provide the total precipitable water in a vertical column. In either case, the calculated value can then be used in atmospheric models to predict the absorption due to precipitable water (PW). An example of the impact of PW on the spectral irradiance is given in Figure 2.4.

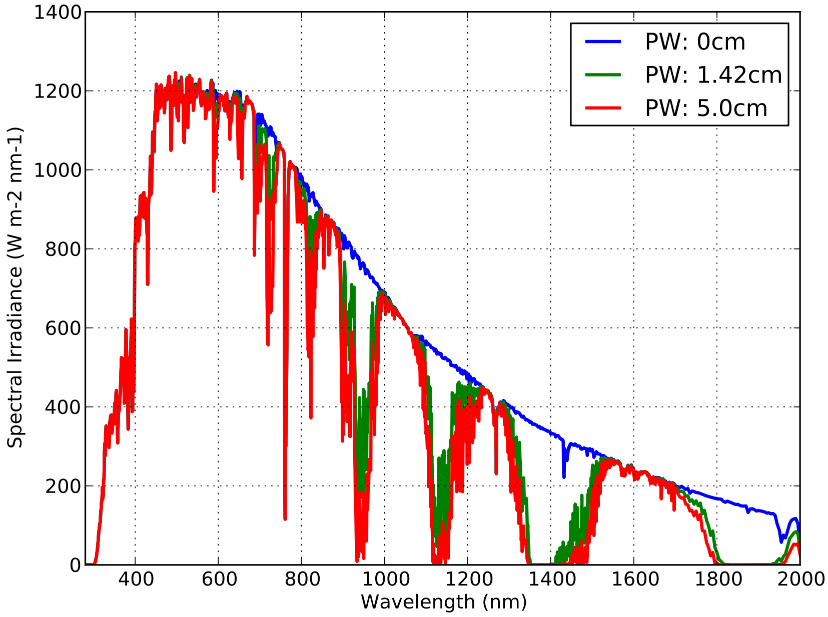

Figure 2.4: Direct Normal Irradiance as a function of precipitable water. Spectra simulated using SMARTS v2.9.5, with AM1.5D reference conditions for all variables other than PW. Attenuation occurs in very specific bands, centred on 960, 1100, 1400 and 1900nm.

2.1.4 Ozone, Gaseous Pollutants and Uniform Mixed Gases

The extinction from ozone and trace gases, which include gaseous pollutants such as Nitrogen Dioxide (NO_2), can also be described by the Beer Lambert Bouger Law [45]. Each element has its own unique absorption profile; ozone absorbs strongly in the ultraviolet (UV) region (≈195-345nm) [53], but also weakly in the visible Chappuis bands (375-650nm); NO_2 absorbs from ≈260-650nm and is responsible for the brown haze associated with pollution clouds in urban areas, and is known to be highly variable in both temporal and spatial terms [46, 54, 55]; other uniform mixed gases, such as oxygen (O_2) and Carbon Dioxide (CO_2), do not vary greatly with location and absorb in very specific wavelength ranges, which are linked to the bonds in the molecules.

2.2 Basic Photovoltaic Principles

The photovoltaic principle is the conversion of light energy to electrical energy in a single step, through the excitation of electrons to higher energy levels by photons, where they are then free to move through the material. In most materials, promoted electrons quickly relax to the lower energy level, but a photovoltaic device extracts that electron to perform useful work in an electronic circuit, using semiconductors. These materials have electrical conductivity performance between insulators and conductors.

2.2.1 Photogeneration

For a semiconductor material, its band structure means that there is a single finite energy gap between the valence and conduction bands, hereafter referred to as the *band gap.* A photon with sufficient energy (i.e. greater than this energy gap) will be able to promote an electron from the valence band to the conduction band, generating an electron-hole pair. A photon that possesses lower energy than the band gap is unabsorbed and transmitted through the material, whilst an absorbed photon with higher energy than the band gap excites an electron, and in most materials this quickly relaxes down to the conduction band. This promotion of the electron creates a hole (the lack of an electron) in the valence band. These processes are summarised in Figure 2.5. The flow of charge resulting from this generation and extraction of carriers is referred to as a *photocurrent*. Given sufficient time inside the semiconductor, the electron-hole pair generated will recombine, hence it is important to extract these carriers to perform useful work in an electronic circuit.

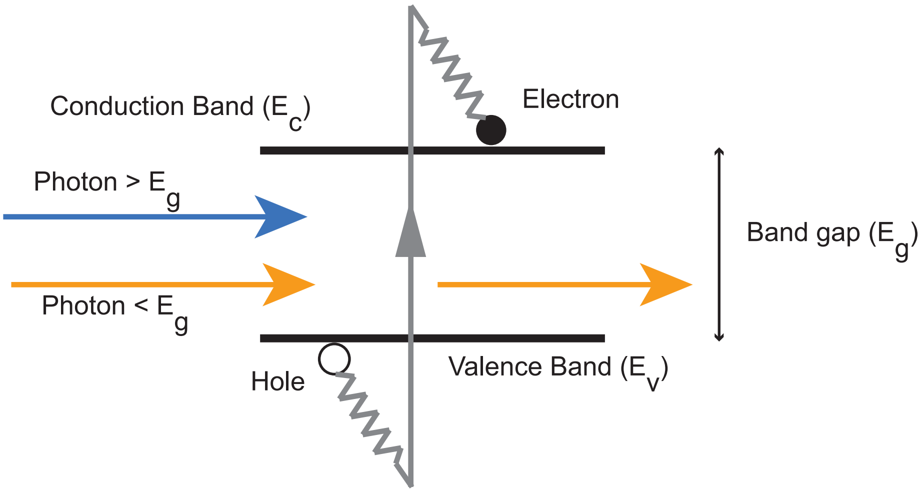

Figure 2.5: Photogeneration in a semiconductor at equilibrium.

The *quantum efficiency (QE)* of the junction provides a way to evaluate the spectral dependence of the photocurrent of a device. The QE at a particular wavelength describes the efficiency with which a photon is converted into an electron - e.g. a QE of 75% indicates that for every 100 incident photons, 75 electrons are generated. Alternatively, QE can be expressed in fractional form (e.g. 75% = 0.75).

There is a distinction to be made between the *internal* quantum efficiency (IQE) and the *external* quantum efficiency (EQE). IQE gives the ratio between charge carriers and photons *absorbed* by the solar cell, whilst EQE gives the equivalent value for photons *incident* on the cell. In the characterisation of device performance, EQE is usually published. An example for the EQE of a Gallium Arsenide device is shown in Figure 2.6, with the data extracted from [56].

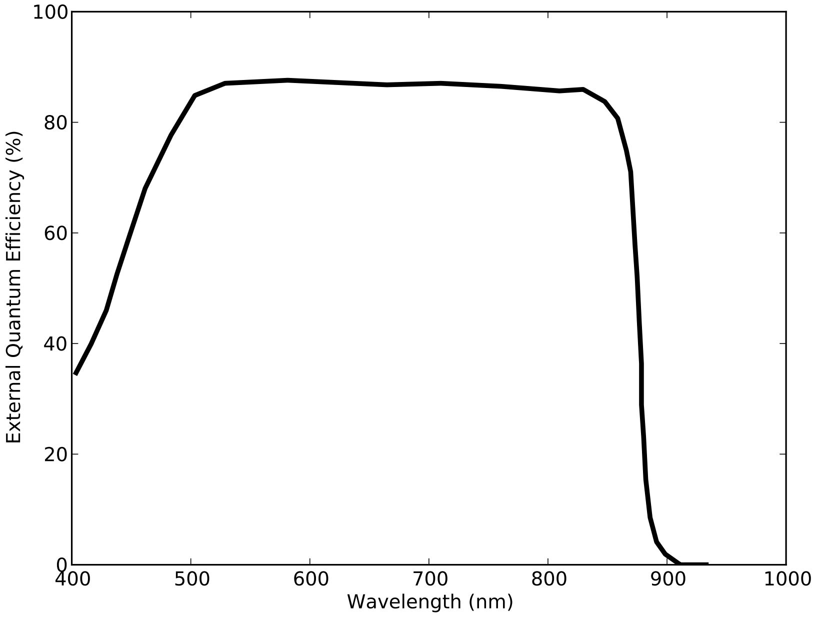

Figure 2.6: External quantum efficiency of a single junction Gallium Arsenide solar cell, data extracted from [56].

The calculation for photocurrent can be expressed mathematically, as in Equation 2.6.

$$J_\lambda = \Phi_\lambda \times EQE_\lambda \times q \tag{2.6}$$

where J is the photocurrent, Φ the photon flux, q the electric charge. The λ subscripts denotes the wavelength dependence of these quantities.

2.2.2 p-n junctions

Power generation is achieved with the use of a p-n junction in many photovoltaic devices. This allows for the photogenerated carriers (electrons and holes) to be extracted from the semiconductor material into the electrical circuit to perform useful work. A p-n junction consists of two layers of the same material (a homojunction) - the p-type layer will have a greater density of holes compared to electrons, whilst the n-type layer will have a greater density of electrons than holes.

This is accomplished through the introduction of dopants - elements that have more/less electrons than the semiconductor material. For p-type material, this is often Group II elements such as Beryllium or Magnesium, whilst the n-type often uses Group IV elements.

A p-n junction is created by bringing together a p-type and n-type layer, and as free carrier diffusion takes place across the junction, a region of fixed charge is set up due to the ionised dopant atoms. This is referred to as the space charge region (SCR) and an electrostatic field is produced from the separation of ionised dopants, facilitating the extraction of free carriers to the neutral regions away from the SCR and eventually to the metal contacts.

Under equilibrium conditions, no there is no current flow in a p-n junction and all charge carriers (electrons and holes) recombine at the same rate as generation. In the operation of a solar cell, this equilibrium is disturbed by exposure to photons with energy greater than the band gap, increasing the number of holes and electrons above the equilibrium values. This results in a change in the carrier distributions, and the energy up to which states are occupied, represented by the *Fermi energy* E_F, for each region of the p-n junction, E_{Fp} and E_{Fn}. The difference between E_{Fp} and E_{Fn} is the voltage, or bias. Alternatively, a bias V can be applied to the junction to modulate the current flow. An example of a p-n structure is given in Figure 2.7, at equilibrium and under illumination. Further details of the precise workings of a p-n junction can be found in [57].

By applying different voltages, the current reaching the contacts changes, due to a change in the electrostatic potential and the rate of carrier recombination. This can be represented as a *current-voltage (IV) curve*, an example of which is shown in Figure 2.8. At zero bias, where V=0, this is referred to as short-circuit condition, the associated current flow is referred to as short-circuit current (I_{SC}). Because electrical power generated is the product of current and voltage, the power generated is zero.

At a bias of $V = V_{bi}$, no current flow occurs as the electronic potential

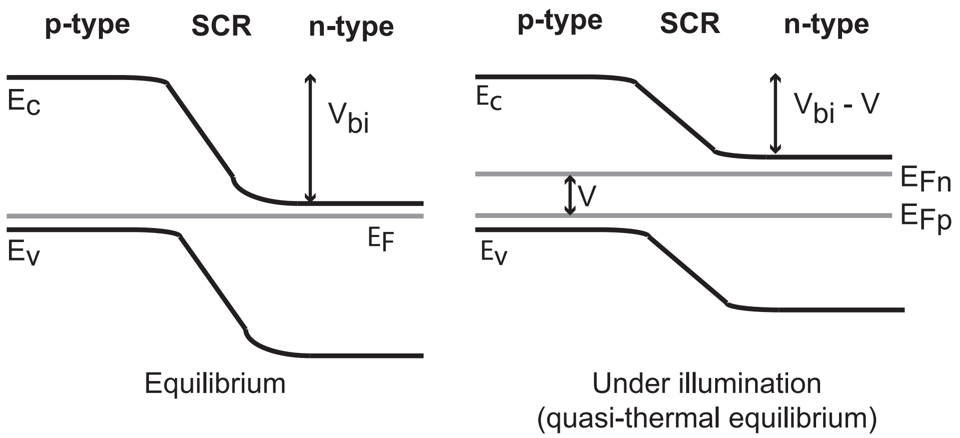

Figure 2.7: An example of a p-n junction, at equilibrium and under illumination.

is now zero - the conduction bands are at the same energy level. This bias is referred to as the open-circuit voltage (V_{OC}). Due to the lack of current flow, again the power generated is zero at this point.

At an intermediate point between these the open-circuit and short-circuit conditions, the power generated reaches a maximum. This is referred to as the maximum power point (MPP). The locations of these points are illustrated in Figure 2.8 for a GaAs solar cell with arbitrary short circuit current and open circuit voltage.

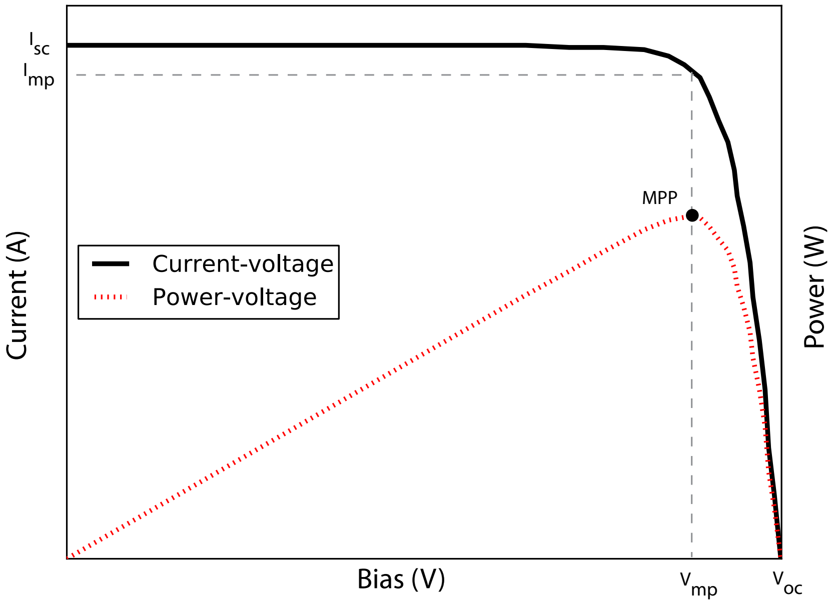

Figure 2.8: Current-voltage and power-voltage curve for an example GaAs solar cell. Units are arbitrary.

The electronic behaviour of the solar cell can be well represented by an electronic circuit as outlined in Figure 2.9. The current source I_{sc} represents photogeneration, which is dependent on the device bias. Two separate recombination processes are represented by two diodes, and are discussed in a later section. Parasitic resistances in the device are represented by the resistors connected in series and parallel, representing series (R_{series}) and shunt resistance (R_{shunt}) respectively.

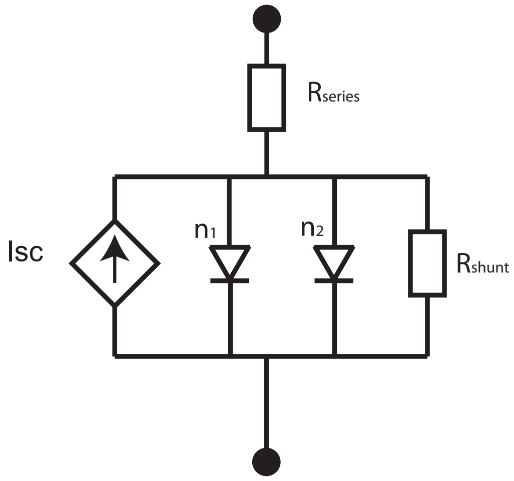

Figure 2.9: A single-junction solar cell, represented with electronic components in a circuit.

2.2.3 Design considerations and limiting efficiency

In addition to the photocurrent, a voltage is generated from the material's exposure to photons, but this is limited by the material's band gap. In a single junction device, a low band gap will lead to a high photocurrent, but a correspondingly low voltage, whereas a high band gap will produce a high voltage but low photocurrent, due to the relative scarcity of high energy photons. The solar spectrum contains photons with a wide range of energies and a specific distribution, an example of which is shown in Figure 2.10 for the solar irradiance reaching the top of Earth's atmosphere. This trade-off is illustrated in Figure 2.11 and is well understood for single junction solar cells under the standard reference spectrum, and the band gap where the optimum balance between photocurrent and voltage occurs (giving the highest output power) is referred to as the *optimum band gap.*

This effect allows one to calculate an efficiency limit for the single junction solar cell - the fraction of incident solar energy that can be converted to electrical energy by the solar cell. This has been identified as occuring at a band gap of ≈1.35 electronVolts (eV) and offers an efficiency of 31% under 1-Sun concentration, assuming absorption of all light above the band gap [58].

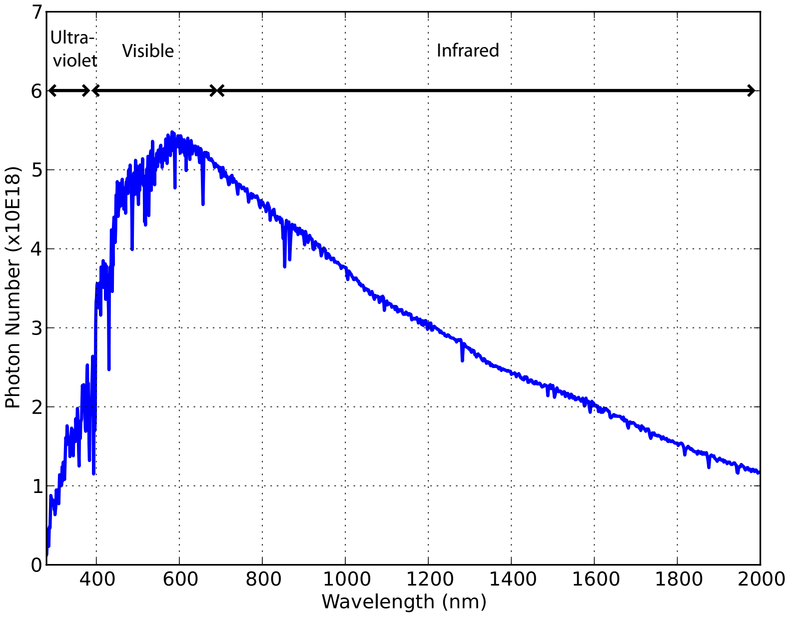

Figure 2.10: Number of photons as a function of wavelength, with appropriate wavelength ranges labelled, for an extraterrestrial air mass zero spectrum.

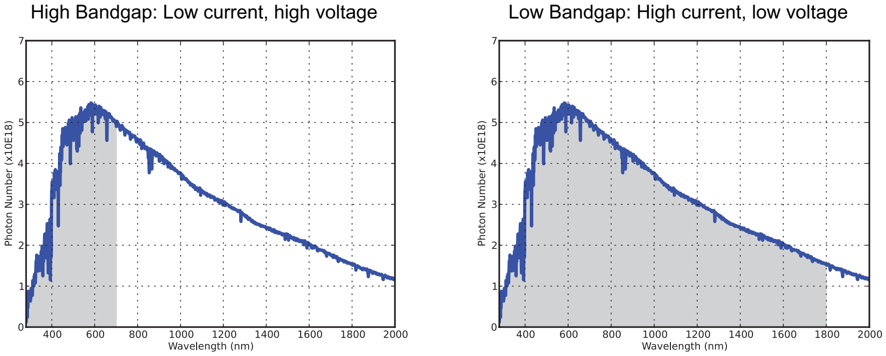

Figure 2.11: Trade-off between voltage and current production. High band gap devices have high voltage and low current, and vice versa.

2.3 Multijunction Solar Cells

To overcome the limiting efficiency of single junction solar cells, an alternative design was proposed for solar cells - this cell would contain two or more junctions, each with their own distinct band gaps, as shown in Figure 2.12. By doing so, the solar spectrum is effectively "split up" to be absorbed by each of the junctions with band gaps that result in reduced thermalisation loss (a result of absorbed photons possessing more energy than the band gap of the absorbing junction, and thus needing to thermalise to the band gap energy), and below band gap loss (where the photons are not absorbed) [43]. Individually, these junctions produce a lower photocurrent, but the sum of their generated power is larger than that obtainable by a single junction. The theoretical maximum efficiency of a multijunction solar cell (MJSC), with an infinite number of junctions, has been calculated as 86% under maximum concentration and detailed balance conditions [59]. In a practical device, there is a finite number of junctions, each with their distinct quantum efficiencies. An example for a triple-junction solar cell is given in Figure 2.13.

Photovoltaic conversion is also achieved by p-n junctions in multijunction solar cells. In the vast majority of designs, these p-n junctions are electrically connected in series. In order to ensure low electrical resistance between two junctions of different band gaps, and because of doping in each junction, a tunnel junction is required between two p-n junctions. This is usually a highly doped, large band gap III-V semiconductor, allowing electrons to tunnel easily from the valence band of one junction to the conduction band of the next, increasing electrical conductivity and hence minimising resistive and voltage losses. This tunnelling region is typically narrow and has a large current density, ensuring all photocurrent from the junctions can be extracted. The basic band structure for the tunnel junction region in a 2-junction MJSC is given in Figure 2.14.

The industry-standard multijunction cell can be represented in an electrical circuit diagram, as in Figure 2.15 for a triple-junction device. A controlled current source represents the photogeneration of each junction, whilst the two diodes represent different loss mechanisms [60]. Shunt and

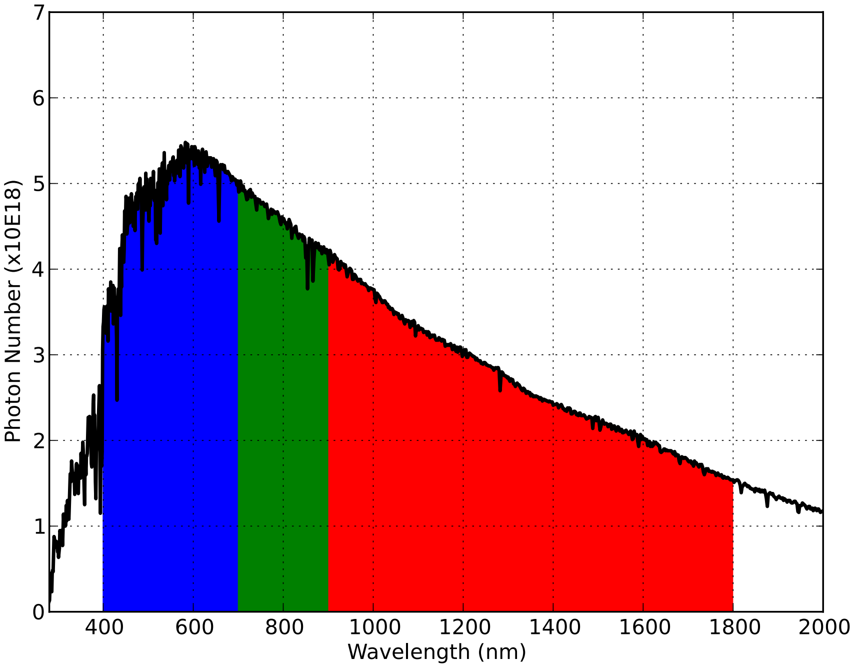

Figure 2.12: Splitting the solar spectrum to enhance solar cell efficiency. Each junction has a different band gap and absorbs in a different part of the spectrum, resulting in a lower photocurrent in each junction, but higher voltage. Spectral splitting minimises the thermalisation and below band gap losses.

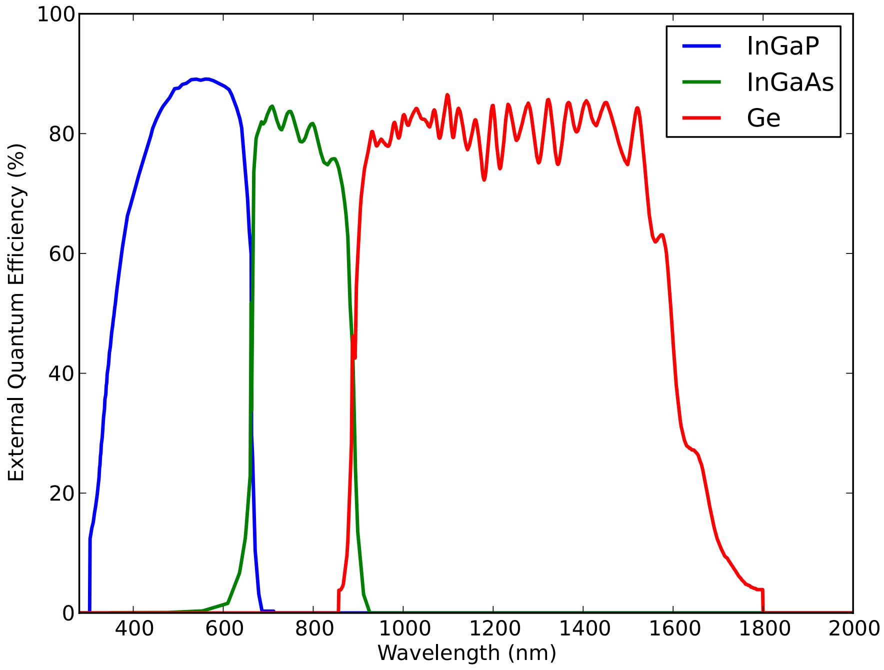

Figure 2.13: External Quantum Efficiency for a triple-junction solar cell, with Indium (1%) Gallium Phosphide/Indium Gallium Arsenide/Germanium junctions.

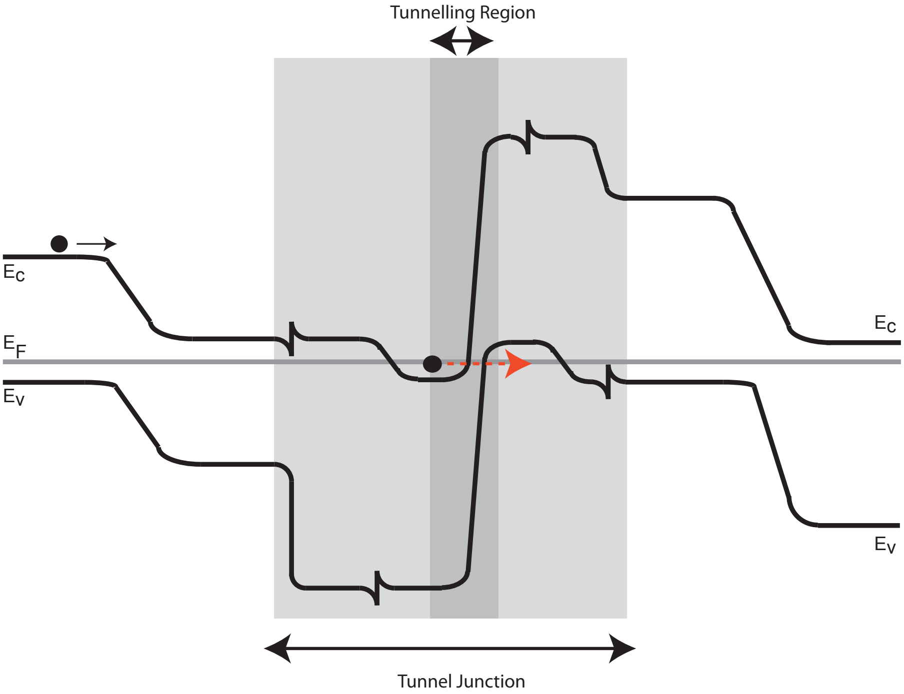

Figure 2.14: The band structure for the p-n junction and tunnel junction interface of a 2-junction multijunction solar cell. Electrons represented by black dot, tunnelling occurs in the dark-grey shaded region, indicated by the red-dotted arrow.

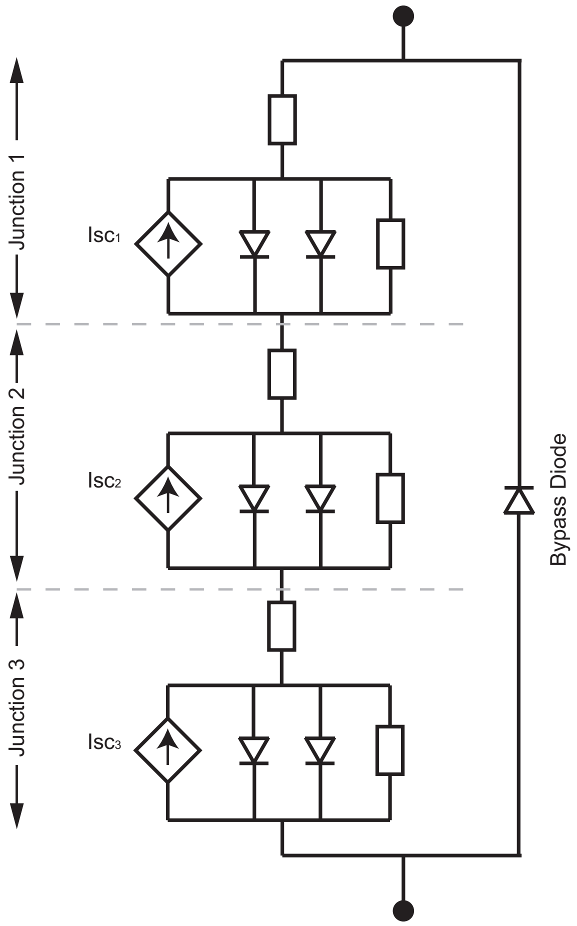

Figure 2.15: A monolithic, 2 terminal, triple-junction multijunction solar cell, represented with electronic components in a circuit.

series resistive losses are represented by the two resistors in parallel and series with the current source, respectively.

By considering Kirchoff's Current Law, the current passing through the entire circuit must be identical - hence band gaps for each junction must be carefully selected. The sum of voltages generated in each junction will give the voltage for the entire device. A bypass diode allows for the failure of one cell to be bypassed in a series connected string of MJSCs.

In modern designs, the junctions are grown either molecular chemical vapour deposition (MOCVD) or molecular beam epitaxy (MBE) techniques in a monolithic stack - these are electrically conductive and the resulting product is a monolithic device.

The MJSC stack concept can also be composed of mechanically-stacked junctions, where the junctions are grown separately and bonded with semiconductor contacts to form a two-terminal monolithic MJSC [61–63]. This approach aims to minimise the propagation of defects and dislocations, but the processing complexity is increased, due to the wafer-bonding process required.

Other methods of achieving the multijunction effect can include spectral splitting using optical elements, with the split photons directed towards multiple single junction devices (in a non-monolithic structure) that are externally electrically connected [64–66].

Each junction in a multijunction solar cell possesses a different band gap. In monolithic stacks, the junctions are internally electrically connected in series with two terminals at the top and bottom of the device. Because all the components in a series connection carry an identical current, the current passing through the device is limited by the junction producing the lowest current. This introduces an issue commonly referred to as "current limiting" problem, in that the performance of the multijunction solar cell is constrained by the lowest performing junction - characterised by low current production. There is, however, another consideration - for a gain in current, the band gap is lowered, resulting in lower voltage. Hence, fabricating multijunction solar cells that minimises the difference in current between junctions is crucial for enhanced performance. This can be achieved through a careful selection of each junction's band gap and control of its thickness, as detailed in [67].

Early approaches to fabricating monolithic MJSCs began in the 1970s and initially achieved an efficiency of 13.9% in a 2-junction device [68], in the years that followed saw a rapid rise in efficiency, with a variety of materials tested in an attempt to enhance performance [69–71]. In 1990, a 2-junction device with an efficiency of 27.3% was fabricated at the Solar Energy Research Institute [72], with a material system (Indium Gallium Phosphide, Gallium Arsenide, or InGaP/GaAs) that is still widely in use today. It is important to note that the InGaP junction is commonly thinned, as to provide a balance between the photocurrent generation between the InGaP and GaAs junctions, as detailed in [72].

State-of-the-art MJSCs have achieved 43.5% conversion efficiency (418X concentration, AM1.5D spectrum) using a triple-junction structure using Group III and Group V elements (III-V) [73]. Although the precise composition of the junctions and the growth techniques involved are commercially sensitive, the types of materials are often well known. There exist various constraints limit the materials that can be used to fabricate MJSCs - these include cost, availability, band gap, lattice-constant, suitability for a given substrate and growth processes. Given these factors, the standard cell in the CPV industry is the lattice-matched (LM) Indium Gallium Phosphide/Indium Gallium Arsenide/Germanium (InGaP/InGaAs/Ge) design where the lattice constants for all junctions are very similar, with band gaps of 1.88/1.41/0.67eV, fabricated on a Germanium substrate with the lowest band gap grown first. These standard lattice-matched designs offer efficiencies of ≈39% on average [74, 75].

Other notable variations on the standard MJSC design all aim to improve the efficiency under realistic operating conditions. Upright metamorphic (MM) devices are normally fabricated on Ge substrates and aim to achieve different band gaps, although these the lattice constant in these devices undergo relaxation [76, 77]. Such lattice-mismatch can lead to defects and dislocations during growth, complicating growth processes and impacting power output, but the latest results show a small advantage in efficiencies with the latest generation of MM cells [75].

Similarly, inverted metamorphic (IMM) devices aim to access band gaps with lattice constants that differ from the substrate (InGaP/GaAs/InGaAs), which theoretically offer greater efficiency. Key differences compared to the MM approach are the substrate used (GaAs) and the growth order is inverted, e.g. the junction with highest band gap is grown first, with the lowest band gap junction last. The top two junctions have lattice constants well-matched to GaAs and can be grown with ease. A photovoltaically inactive layer, referred to as a buffer, with a gradually changing lattice spacing is then deposited between the second and third junction, whose lattice constants differ substantially, as illustrated in Figure 2.16. The final junction is then grown with some dislocations, and the GaAs substrate is etched off, the wafer lifted off (to be reused) and the structure is "flipped" and mounted onto a support structure. By inverting the growth, the dislocations are limited to the bottom junction, allowing for higher performance in the top two junctions. Such approaches have shown an increase in performance over the standard lattice-matched triple-junction structure, and offer greater mechanical flexibility due to the absence of a thick substrate as in the LM design [78, 79].

Aside from using only one material in each junction, a concept originally developed at Imperial College used quantum mechanics to create quantum well multijunction solar cells (QWSC) [80–84]. These solar cells insert quantum wells into the bulk junctions, enhancing the absorption at wavelengths beyond than the band gap of the bulk material and increasing current generation in the junction, without a large penalty in voltage. Recently, efforts have been made to fabricate quantum dot multijunction solar cells (QDSC), which rely on a similar concept but use quantum dots to extend the absorption range instead [85, 86]. An illustration of the solar cell structures discussed in this section is given in Figure 2.16.

Although most solar cells terrestrial use fabricated from III-V materials are implemented in concentrator PV systems due to their high cost, a notable exception is the recent effort from Alta Devices [73, 87], which is not expected to be used in concentrators. These thin-film GaAs solar cells offer the highest conversion efficiency for a single junction solar cell to date (28.8%) [87], and are marketed as flexible devices.

The sizes of MJSCs are much smaller than those of silicon and thin-film devices, a reflection of their higher cost, but also far higher efficiency. Depending on the concentration ratio, typically each MJSC varies from 5x5mm^2 to 10x10mm^2 (producing ≈20-40W per cell, depending on concentration), compared to 200x200mm^2 for monocrystalline silicon cells, and

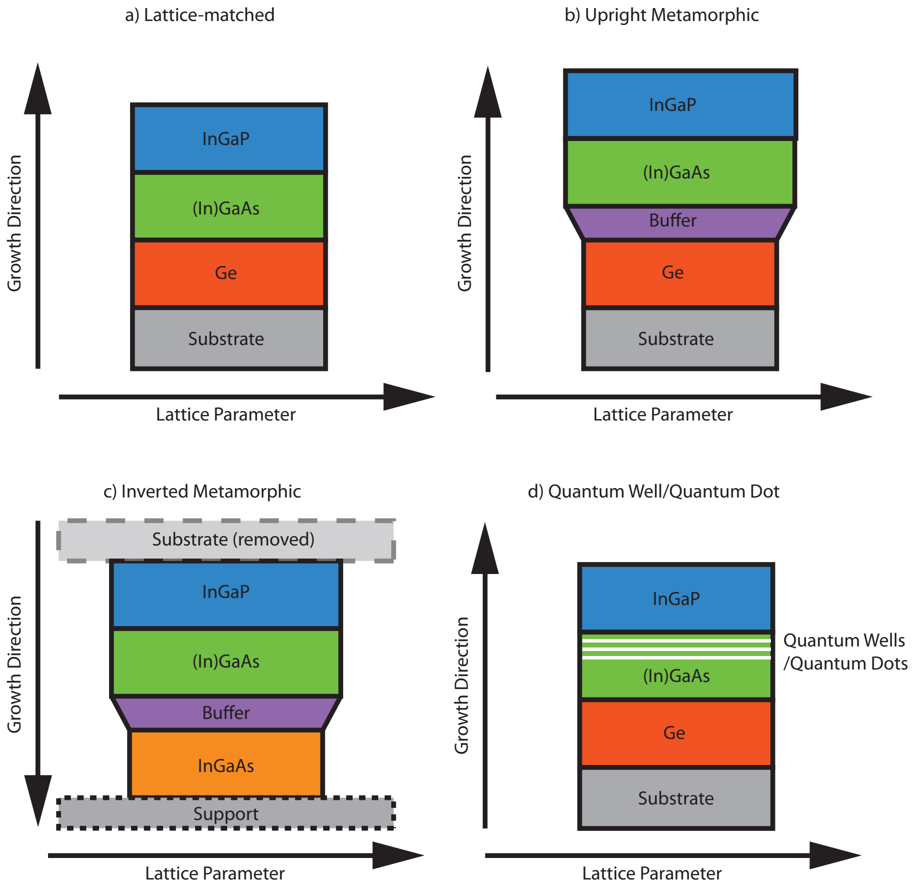

Figure 2.16: Examples of Multijunction Solar Cell Structures

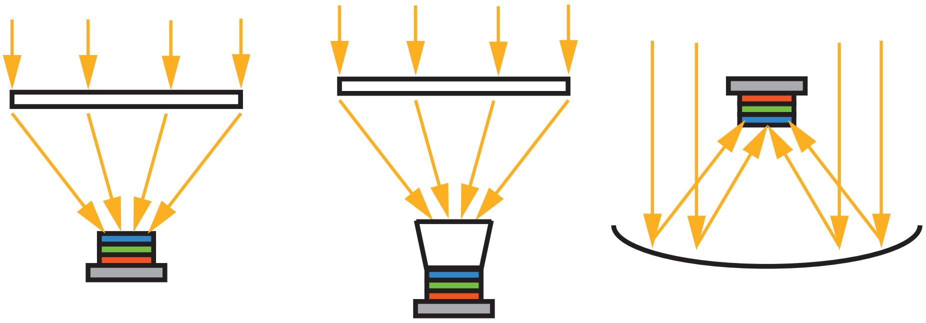

Lens illumination (No homogeniser)

Lens illumination (With homogeniser)

Parabolic Reflective Dish

Figure 2.17: Examples of common CPV system optics - lenses (with [89] and without homogenisers [90]) and parabolic reflective dishes [91].

larger still for thin-film cells with lower efficiencies. Examples of MJSCs with even smaller sizes (0.6x0.6mm^2) exist, and aim to reduce complications from heat dissipation and simplifying optical elements [88].

2.4 Concentrator Photovoltaic System Designs

A typical CPV system will consist of three main parts: the cell, the concentrating optics and the tracking mechanism, illustrated by Figure 2.17 and 2.18.

A range of optical elements and materials are in use to achieve the required concentration of solar irradiance, such as domed and flat fresnel lenses [89, 90, 92, 93], small individual reflectors [94] and large parabolic reflective dishes [91]. In some systems, a homogenizer is installed as a secondary element to ensure that light reaching the solar cell is evenly distributed spatially. The transmission profile of the material used, such as PMMA, glass or silicone-on-glass, is a particularly important consideration, as it changes the solar spectrum incident on the cell. Optical aberrations and changes in temperature can often affect the effectiveness of the optics, often by changing the position of the focal point [95–100].

The maximum achievable concentration ratio is often limited by the heat

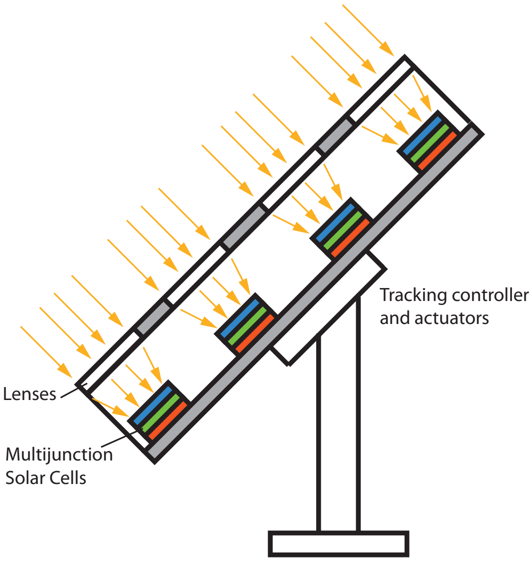

Figure 2.18: Example of a fresnel lens CPV system with tracking controller and actuators, in a pedestal mount.

dissipation required from the solar cell. Most systems employ passive cooling, commonly heatsinks and fins at the rear of modules to provide a larger surface area for heat to be transferred to the environment. Some systems types, particularly parabolic dish optical structures with a central receiver, often required active cooling [101, 102]. In addition, tracking systems with higher precision must be used due to the greater accuracy demands. With greater concentration comes smaller devices, where thermal dissipation becomes more challenging. Systems where active cooling is present are deployed [103] - it is likely that there will be large utility-scale uses for heat, such as district heating or hot water and desalination in the future [104,105].

Tracking mechanisms orientate the module so that the maximum amount of DNI is captured. For high concentration ratios, the accuracy requirement becomes much more stringent. An electronic tracker controller supplies information to actuators which allow for movement of the module (cells and optics).

CPV technology has been commercialised in recent years, with module manufacturers all competing for market share and constructing different system types as highlighted in Figure 2.17: Lens illumination (Soitec, Amonix, Daido Steel, Semprius); Parabolic Reflective Dish, central receiver (Solar Systems Pty, Zenith Solar); Parabolic Reflective Dish, receiver array (SolFocus); and other less common types, such as tilt and roll (Emcore). With a few exceptions, most module manufacturers and installers do not manufacture their own solar cells and instead purchase MJSCs from cell-makers such as Spectrolab, Sharp, Solar Junction, JDSU and Azur Space.

A number of 2-axis tracking module designs have been trialled, but most have opted for a pedestal-based tracking system - a central pole is sunk into a foundation, with flat panels mounted onto the support structure and tracking is driven by hydraulic actuators. A pedestal dish system is used by Solar Systems, where a parabolic dish is mounted on a pedestal and tracks the sun's position, with an array of MJSCs placed at the dish's focal point.

2.5 Rating CPV Systems

In order to standardise the measurement of performance, photovoltaic cells and systems are rated under specific reference conditions. This allows for ease of comparison across systems of different designs, sizes.

In flat-plate systems, the Standard Test Conditions are used to provide a rating for a specific system, consisting of the Air Mass 1.5 Global spectral distribution, 1000Wm^{-2} integrated irradiance, a module temperature of 25^0C, as defined in IEC 61215. This spectrum considers both direct and diffuse irradiance, which can both be accepted by flat-plate PV systems due to their lack of focal optics. By contrast, CPV systems accept only direct irradiance.

It was recognised that due to the difference in accepted irradiance between flat-plate and CPV systems, the standard test conditions (STC) applicable to the former cannot be suitably applied to the latter. In response to this, the Concentrator Standard Test Conditions (CSTC) were introduced in IEC 62670-1 [106], and all CPV rating tests are performed under the AM1.5 Direct solar spectrum. Figure 2.19 illustrates the quantitative difference between the AM1.5 Global and Direct solar spectra, characterised

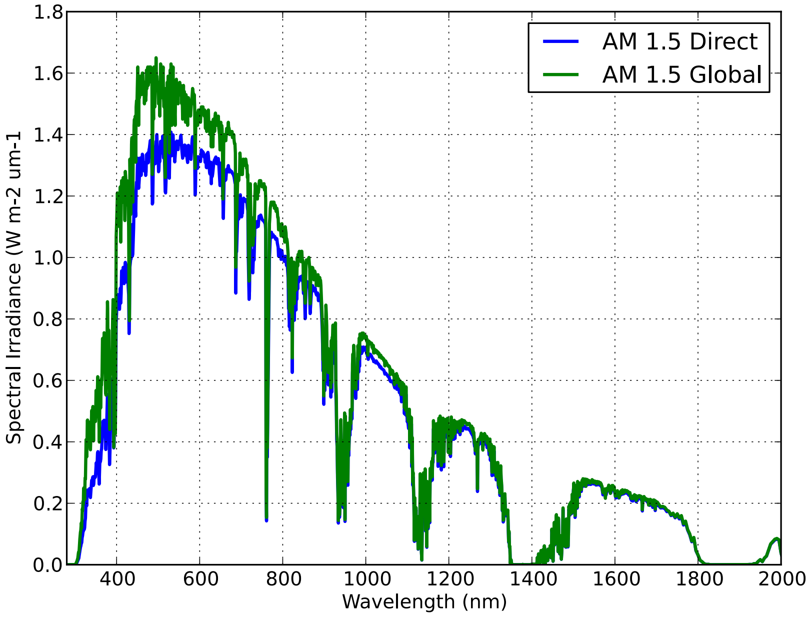

Figure 2.19: A comparison between the AM1.5 Global and Direct Spectra, as defined in IEC 61215 and 60904 respectively.

Test Parameter	**CSTC**	**CSOC**
Irradiance	1000Wm^{-2} Direct Normal Irradiance	900Wm^{-2} Direct Normal Irradiance
Temperature	25^0C	20^0C
Temperature Location	Cell	Ambient
Spectrum	AM1.5 Direct Normal Scaled to 1000Wm^{-2}	AM1.5 Direct Normal
Wind Speed	0ms^{-1}	2ms^{-1}

Table 2.1: Concentrator Standard Testing Conditions (CSTC) and Concentrator Standard Operating Conditions (CSOC) for rating CPV systems.

by higher irradiance at low wavelengths.

To better represent the operating conditions of CPV systems, a second standard was developed, the Concentrator Standard Operating Conditions (CSOC), again defined in IEC 62670-1 [106]. This standard recognised the difficulty in obtaining cell temperature measurements in operating systems, and instead requires a measurement of ambient temperature. DNI is also lower to better match realistic conditions, and a specific wind speed is introduced to account for cooling in outdoor conditions. The conditions and numerical values for both standards are given in Table 2.5. For CPV, there are three laboratories certified to make these measurements and provide a rating: the National Renewable Energy Laboratory, Golden, Colorado, United States; Fraunhofer Institute for Solar Energy Systems, Freiburg, Germany; and the National Institute of Advanced Industrial Science and Technology (AIST) in Japan.

Another important metric is the energy produced by the CPV system over the course of its deployment. There is currently no technical standard on assessment of CPV module performance over a time period, but it is expected that this will be published in the near future as IEC 62670-2 [107, 108]. The existing methodologies proposed for rating energy production is discussed in a later section.

2.6 Advantages of CPV

A key advantage of a CPV system over other types of photovoltaic technologies is its higher efficiency. For a given peak power rating, a CPV power plant should theoretically require less land area than other photovoltaic technologies. It is recognised that there are practical constraints such as minimising shading of modules leads that cause the actual area used to increase from this theoretical value. Although currently per-Watt-peak installed prices for CPV systems are above that of crystalline-Silicon and CdTe, the levelised cost of energy (LCOE) of CPV is expected to be competitive with these other technologies in locations with good DNI irradiance [109, 110]. This metric gives the cost per unit of energy generated, and better reflects the amount of energy produced by CPV over flat-plate PV systems.

In order to meet the challenge of climate change mitigation, new energy sources must emit substantially less CO_2 per unit of energy, referred to as specific carbon emissions, than existing fuel sources. In this respect, CPV has been noted to only emit 27g CO_2-eq. per kWh of electricity generated in locations with high DNI resource [111] , compared to harmonised values of 45g CO_2-eq/kWh for crystalline Silicon [112] and as low as 14g CO_2-eq//kWh for CdTe modules [113]. The harmonisation approach attempts to address inconsistencies in different LCA studies [114], through converting published values into numbers that use identical performance parameters. In comparison to traditional fuel sources, photovoltaic systems of any type have much lower specific carbon emissions - coal for example emits 1001g CO_2-eq/kWh of electricity generated [115].

2.7 Technical Developments in Concentrator Photovoltaics

The theoretical limit associated with solar-to-electricity conversion efficiency with bulk (each junction is made from a single material, though doped into p and n regions) MJSCs is 86% [59], and >60% with three junctions [116]. When compared to the attained efficiencies, it is clear that there is greater scope for performance improvement than silicon, which is much closer to the single-junction theoretical limit. Ways in which this can be achieved include:

- **More junctions** - Adding more junctions to the MJSC will produce cells with a lower current, but higher voltage output across the entire device [117, 118]. Devices with a greater number of junctions become more sensitive to changes in the solar spectrum, and may require materials such as antimony (Sb) and nitrogen (N) to be introduced [119]. A junction with a band gap of 1eV and good material quality that can be incorporated easily within existing structures is seen as the next hurdle to higher efficiency.

- **Increased Concentration** - Use of optical elements with a higher concentration ratio. This is limited by heat dissipation from the solar cells and by ohmic heating during in the metallic contacts of MJSCs. Higher concentration leads to smaller solar cells, higher photon flux and enhanced current production, but also a lower volume of metal contacts with which to conduct the current produced.

- **Reduced substrate use** - The substrate used in production can be greatly reduced, through techniques such as epitaxial lift-off [78, 79] and substrate re-use, which has been shown to have negligible impact on the quality of the solar cells manufactured after multiple growths, provided appropriate treatment is applied to the substrate [120]. Such approaches have the potential to drastically lower the cost of MJSC devices.

- **Use of alternative materials** - Alternative materials such as Indium Phosphide (InP) [121], the use of InP as a substrate and growth of quaternary materials [122, 123], potentially allowing more optimal band gaps to be accessed. Potential problems include the ability to reach high band gaps in the top junction and high cost of InP substrates, necessitating substrate reuse techniques.

- **Nanostructures** - Inclusion quantum wells (QW) and quantum dots (QD) in devices to extend their absorption range [82–84, 124–127] ; plasmonic structures that enhance absorption [128–131]; and hot carrier solar cells. These approaches are at various stages of implementation, with QWSCs and QDCSs already on the market, whilst the plasmonic techniques at a very much laboratory stage.

- **CPV-Thermal** - Due to its concentrating optics, CPV systems have the theoretical potential to generate heat as well as electricity, raising their energy conversion efficiency [104, 132, 133]. Additional complexity introduced in the cooling system and the associated transport of the heat, along with the quality of the heat (i.e. its temperature) place constraints on energy conversion efficiency.

Compared to crystalline silicon and thin-film technologies, there is a number of achievable ways in which the efficiency can be improved and hence the cost lowered through technological improvements, instead of simply cost reduction in the manufacturing process.

2.8 Challenges to Concentrator Photovoltaics

Despite the technological advantages, CPV faces financial challenges to becoming widely adopted. Aside from a rise during 2008-10, the cost of crystalline silicon PV modules have maintained a year-on-year decrease since 2008 [134], and have been joined by the thin-film CdTe PV modules, with both offering low cost per Watt-peak (USD\$1.10/W$_p$ and \$0.74/W$_p$ in 2011, for crystalline silicon and CdTe respectively [135]).

The reliability any photovoltaic system is of great importance to investors, as it has a large role in determining the return on their investment. As a developing technology, the reliability of CPV systems needs to be further substantiated and proven, evidenced by the publications in the area [136–139].

Material abundance can also be an issue for CPV - in the production process, MJSCs use rare-earth elements such as Gallium and Indium, which are also in demand from other electronics industries [140]. Such issues are however not exclusive to CPV - for example, Indium and Tellurium availability is also expected to become an issue in thin-film manufacturing [141].

Measurements of the solar resource and its intermittency are required to estimate the performance of any photovoltaic system in real-world conditions. For CPV, the accurate collection of DNI data across wide regions, either through ground measurements or derived from remote sensing (satellite) measurements [142], must be prioritised. Currently there are limited number of sites that measure the DNI resource with ground instruments where the data is publicly available [143], with even fewer measuring spectrally-resolved irradiance. Some of these resources will be discussed in later chapters. Estimation of the solar resource from remote sensing is also challenging, particularly with DNI [144], and contains large errors in regions with complex atmospheric conditions [145–147].

The accurate prediction CPV system performance under realistic conditions is a key issue that has important ramifications for the cost of electricity. The majority of the work on CPV energy yield prediction has taken place in the United States and the Iberian peninsula, with specific ranges of atmospheric conditions [148–151]. Tools that accurately predict the performance of CPV systems in a range of realistic atmospheric conditions are also crucial - predictions that match well with measured performance will allow investors to have confidence in the technology and encourage its uptake. There is a growing awareness of the need for such methods and tools [152, 153], but the ability to predict performance under a variety of atmospheric conditions is crucial.

3 Simulating the Solar Irradiance - Description of Models and Validation

Given the importance of the solar spectrum in determining the performance of CPV systems due to the use of MJSCs, a variety of tools have been developed to simulate the solar spectrum from measurement of the atmospheric parameters detailed in Section 2. The differ in complexity and ease of implementation, and differ particularly strongly on how aerosols are simulated. Main differences in the three models are described, along with their inputs and key variations in output under realistic conditions. These are referred to generally as radiative transfer tools.

3.1 SPCTRAL2

The *Simple Solar Spectral Model for Direct and Diffuse Irradiance on a Horizontal and Tilted planes at the Earth's Surface for Cloudless Atmospheres (SPCTRAL2)* was developed by Bird and Riordan in 1986 [154] in response to a need for tools that allowed for rapid calculation of the direct and diffuse parts of a solar spectrum on a tilted plane, given the necessary atmospheric parameters. In the publicly available version [155], the aerosol extinction is parameterised with a single Angström Exponent value, which may not accurately represent realistic conditions. In addition, the DNI is calculated with an acceptance angle of 5^0 solid angle, which includes circumsolar radiation and not necessarily captured by high concentration CPV systems, which have acceptance angles of 1^0 or less.

At the highest resolution, DNI values are output every 5nm - this decreases significantly for longer wavelengths, as a result of the input data's

Table 3.1: Atmospheric parameter values used to generate the ASTM G-173 AM1.5D reference spectrum

Atmospheric Parameter	Value
Air mass	1.5
Aerosol Optical Depth, 500nm	0.084
Precipitable Water	1.42 cm
Angström Exponent $<$ 500nm	0.964
Angström Exponent $>$ 500nm	1.431

granularity.

Because the code is parametric and very quick to run (3milliseconds on a 2010 Apple Macintosh Pro), SPCTRAL2 is often implemented (in various forms) in both solar resource and PV performance estimation tools [156–158].

3.2 SMARTS

Additional complexity was introduced in the *Simple Model of the Atmospheric Radiative Transfer of Sunshine (SMARTS)* by Christian Gueymard [46], with more up-to-date spectroscopic data as inputs. Aerosol extinction can be specified in 2-tier Angström approach, where the AOD at 500nm is defined by the user, and two separate Angström Exponents (α_1, α_2 can be input to more accurately estimate the AOD at wavelengths below and above 500nm, respectively. In addition, the inclusion of numerous aerosol models can be invoked in situations when the AOD and/or Angström Exponent cannot be measured. The ability to consider different acceptance angles have also been included. It is important to note that clouds cannot be explicitly modelled within SMARTS.

The current reference solar spectra for photovoltaic systems (ASTM G-173), commonly referred to as AM1.5 Global and AM1.5 Direct for flat-plate and CPV systems respectively, are generated by SMARTS, using the parameters given in Table 3.1.

Similar to SPCTRAL2, SMARTS is a parameterised model and is quick to run - an average simulation for one DNI spectrum will take 0.2 seconds on a 2010 Apple Macintosh Pro desktop system.

3.3 SBDART

The *Santa Barbara DISORT Atmospheric Radiative Transfer (SBDART)* is the most advanced of the radiative transfer tools examined in this section. Written by Paul Ricchiazzi, Shiren Yang, Catherine Gautier and David Sowle, it was developed to analyse problems related to plane-parallel (i.e. not accounting for curvature of the Earth) satellite remote sensing and atmospheric energy budgets. One of its outputs is the direct normal irradiance at the Earth's surface.

In dealing with aerosols, SBDART has key differences with SMARTS and SPCTRAL, with the option of defining AOD at up to 47 wavelengths. Logarithmic interpolation(or extrapolation where the wavelength desired is not within the range of supplied values) is used to supply the model with aerosol optical depths covering the entire wavelength range of the calculation. Such an approach offers greater flexibility than the 2-tier Angström model, as it allows for greater accuracy in estimating the AOD values between the wavelengths measured.

For this added complexity, there is a considerable associated penalty in computing resources and time required - a simulation of a DNI spectrum with SBDART takes approximately 4 minutes on a 2010 Apple Macintosh Pro desktop system, with 14 CPUs working in parallel.

3.4 Comparison of modelled and measured broadband irradiance data

The accurate prediction of the solar spectrum is important for calculating the performance of any PV system, in particular the spectrally-sensitive CPV systems with multijunction solar cells. In order to have confidence in the predictions, validation of the atmospheric model against good quality measurements must be carried out under a range of atmospheric conditions.

SPCTRAL2, SMARTS and SBDART are used to estimate the solar spectrum in predicting DNI. Trapezoidal integration is then applied to calculate the broadband DNI associated with the spectrum, and this is compared to measured broadband irradiance data from a desert site at Sede Boqer, Israel. This location was chosen for its variability in aerosol loading, as well as reasonable variation in precipitable water values over the course of a year.

A publication by the author of SMARTS investigated the accuracy of various radiative transfer tools in a select number of locations [159], finding SMARTS to have reasonable accuracy in DNI prediction, provided appropriate inputs are used. Achieving good accuracy at high air mass was highlighted as a potential issue. A number of comparisons against theoretical and measured spectrally-resolved irradiance measurements were made between SMARTS, SBDART and MODTRAN [160] (a complex line-by-line radiative transfer tool used in the atmospheric physics community, which calculates the contribution of each spectral line for all molecules in the atmosphere) in [161], where aerosol optical depth was identified as key to determining the accuracy of DNI predictions. The usefulness of the default aerosol profiles contained in SMARTS were also evaluated against pyrheliometer measurements in three bands for urban conditions [162].

The accuracy of 18 different radiative transfer models were benchmarked against each other [163], including the SPCTRAL2 model - but in that publication, modifications were made to the original code in its aerosol calculation to use more than one Angström exponent. In the simulations here, the original implementation has been maintained - a single Angström exponent is used to extrapolate AODs away from 500nm. Reference [163] showed that for DNI, the improved version of SPCTRAL2 had mean bias error of -3 to +3% across a range of locations, with the root mean square deviation at 2-5%. The model does not provide breakdowns of these two metrics for different atmospheric conditions - there is some analysis of the modelled versus measured DNI values using the REST2 model [164] at air mass 1.50 ± 0.05, but performance under other atmospheric parameters is not explored. Gueymard also notes that the total uncertainty for typical field measurements, as at Sede Boqer, would be 3% for DNI values, and that an overall root mean square deviation of 3% is indistinguishable from measurement noise.

3.4.1 Key Simulation Methods and Comparison with Experimental Data

A Baseline Surface Radiation Network (BSRN) measurement site at Sede Boqer, Israel (30.90500^{0}N, 34.78200^{0}E, altitude: 500 meters) provides DNI measurements with 1-minute time resolution [143, 165], by an Eppley Normal Incidence Pyrehliometer (NIP).

Located near the BSRN station is an AERONET [166] measurement site 4.5km away (30.85500^{0}N, 34.78222^{0}E, altitude: 480meters), a federation of ground-based remote sensing aerosol networks with standardised instruments, calibration and processing. Precipitable water and aerosol optical depths at a number of wavelengths are measured approximately every 15 minutes for air mass values below 5, calculated using the measured solar zenith angle and equations that are broadly comparable to Equation 2.4. The air mass was not pressure corrected, as this measurement was not available on-site, although the site altitude is accounted for. AOD measurements at 440, 675, 870 and 1020nm are used, and the time period examined here ranges from *2003-01-01 00:00:00* to *2004-01-01 00:00:00*, containing usable 9054 datapoints.

At each of these measurements by AERONET, the BSRN database is searched for the nearest DNI measurement, and simulate the DNI using the atmospheric information and each of the radiative transfer models. In certain instances, there is a large time difference between the nearest BSRN and AERONET measurements. Only measurement pairs (AERONET and BSRN) made within 60 seconds of each other are considered. The values for integrated irradiance from 280 - 4000nm for the models and measurement are then compared.

The AERONET Level 2.0 data used here does not output measurements

Table 3.2: Model validation with measured DNI data at Sede Boqer, 2003-01-01 to 2009-01-01

Parameter	**Measurement Site**
Direct Normal Irradiance and Standard Deviation	BSRN
Aerosol Optical Depths (440,675,870,1020nm)	AERONET
Precipitable Water	AERONET
Air mass (Calculated)	AERONET

when cloudy conditions are detected [167], though there remains a chance that cloud cover is present at the BSRN site, but not the AERONET station. To minimise this, only points where the standard deviation in DNI is <1% of the measured value are examined. This in practice should filter out transient conditions where cloud cover is intermittent.

The accuracy of broadband DNI estimates, relevant to CPV systems, is investigated under different atmospheric conditions. To achieve this, the fractional difference between modelled values from measured DNI values is calculated, defined as:

$$\Delta DNI = \frac{DNI_{Model} - DNI_{Measured}}{DNI_{Measured}} \tag{3.1}$$

All values in fractional deviations - e.g. +0.05 = +5% deviation, where the modelled DNI overestimates by 5%. With this figure, the mean bias error (MBE) of each model's predicted DNI and the root mean square deviation (RMSD) of its predictions can be calculated, as defined below:

$$MBE = \mu = 100 \times \frac{1}{N}\sum_{i}^{N} \Delta DNI_i \tag{3.2}$$

$$RMSD = \sigma = \sqrt{\frac{1}{N}\sum_{i}^{N} (\Delta DNI_i - \mu)^2} \tag{3.3}$$

First, the metrics identified for all datapoints simulated are examined, where the irradiance is above $0\mathrm{Wm}^{-2}$ (occasionally DNI in the BSRN data is recorded as negative).

3.4.2 All Datapoints

Over all 9317 datapoints available at Sede Boqer for the period in question, SPCTRAL2, SMARTS and SBDART achieved MBE values of +0.1%, -2.3% and -2.0% respectively, with comparable RMSD of between 5.6-5.8% for all three models. The distribution in μ is given in Figure 3.1. Although SPCTRAL2 is an older, less complicated code, it appears to show less bias than other models. One must bear in mind that the acceptance solid angle for SPCTRAL2 is set at 5^0 and cannot be changed - whilst this may offer good agreement in this particular case, the acceptance angle for high concentration PV systems using MJSCs tend to be much narrower, at around 1^0 [168, 169], potentially leading to problems if SPCTRAL2 is used in CPV energy yield estimations.

3.4.3 Binning By Irradiance

The accuracy of the radiative transfer codes are first examined as a function of the DNI. The measured spectrum from ground-truth measurements at Sede Boqer are used as the baseline and assumed to be correct, given the uncertainty given previously.

At low DNI, all radiative transfer codes show significant underestimation of the solar resource when compared to measured values. Low measured DNI indicates a long pathlength or substantial extinction due to aerosols or precipitable water, as the AERONET level 2.0 data used here does not output measurements when cloudy conditions are detected.

All codes recover to MBE values around range of uncertainty for field instruments by 300-400Wm^{-2}, allowing us to quantify the DNI threshold beyond which cloudless spectral irradiance prediction may contain substantial errors.

3.4.4 Binning By Air Mass

All models have reasonable performance at all air mass values - in SMARTS, there is a slight trend to more negative bias at high air mass, as noted by the model's author [159].

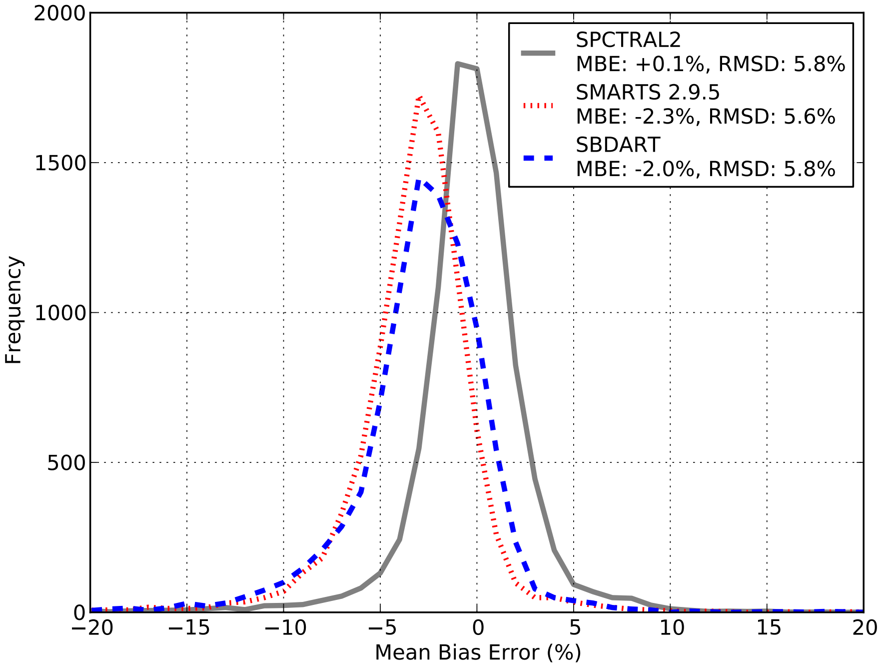

Figure 3.1: Mean Bias Error distribution of radiative transfer code DNI estimates, using all acceptable datapoints. All models are shown to have comparable root-mean-squared deviation (RMSD), but SPCTRAL2 is shown to have the least bias in this situation.

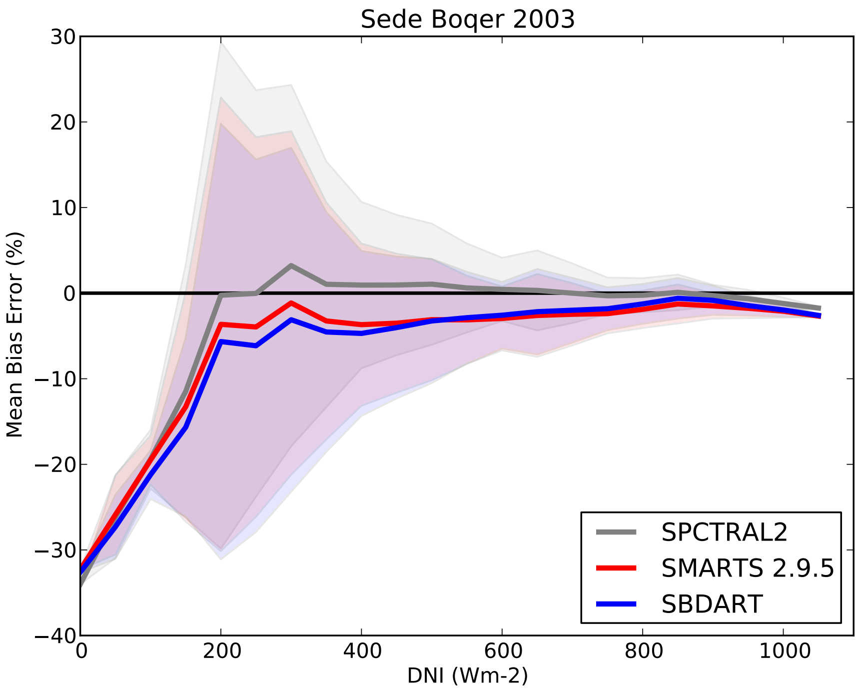

Figure 3.2: MBE as a function of DNI, in $50\mathrm{Wm}^{-2}$ bins. The filled areas correspond to RMSD for each irradiance bin.

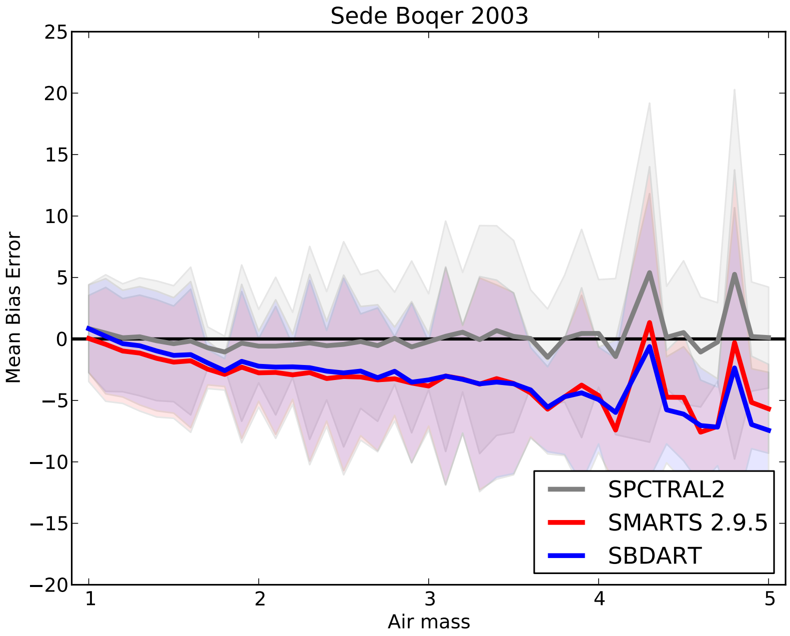

Figure 3.3: Mean bias error (MBE) as a function of air mass.

3.4.5 Binning By Aerosol Optical Depth

The accuracy of predictions under varying aerosol loading is examined in Figure 3.4. Effort has been made to capture as much Angström Exponent information as possible in the model simulations. For SPCTRAL2, this meant using the Angström exponent between 440nm and 870nm ($\alpha_{440-870}$) to extrapolate AOD values away from 500nm. For SMARTS, the AOD at 500nm (AOD_{500}) was calculated using the following relationship:

$$\tau_{500} = \tau_{440}\left(\frac{\lambda_{500}}{\lambda_{440}}\right)^{\frac{ln\frac{\tau_{440}}{\tau_{675}}}{ln\frac{\lambda_{675}}{\lambda_{440}}}} \tag{3.4}$$

and the Angström relation is invoked to calculate the AOD away from 500nm using a two Angström exponents, above and below 500nm. For wavelengths below 500nm, this is:

$$\alpha_{<500nm} = \frac{ln\left(\frac{\tau_{440}}{\tau_{500}}\right)}{ln\left(\frac{\lambda_{500}}{\lambda_{440}}\right)} \tag{3.5}$$

For wavelengths greater than 500nm, this takes the form of:

$$\alpha_{>500nm} = \frac{ln\left(\frac{\tau_{500}}{\tau_{870}}\right)}{ln\left(\frac{\lambda_{870}}{\lambda_{500}}\right)} \tag{3.6}$$

SBDART uses logarithmic fitting of the aerosol optical depth measurements to extrapolate the extinction due to aerosol, which would be most advantageous if AOD measurements were available at a large number of wavelengths.

All the radiative transfer codes examined have acceptable accuracy at low aerosol loadings, but significantly underestimate the solar resource at high AOD_{500} values, where any errors in the Angström exponent would be most clearly seen due to the greater aerosol optical depth.

3.4.6 Binning By Precipitable Water

Generally performance is reasonable across all precipitable water values, close to the uncertainty of field pyrheliometers, as seen in Figure 3.5. A spike in RMSD is noted between PW values of 1.5 to 2.0cm, and is likely due to covariance with one of the other atmospheric parameters. Looking at integrated irradiances, SPCTRAL2 performs surprisingly well given the coarseness of the water absorption spectrum contained in the model - the resolution in SPCTRAL2 is 5nm. This may have an impact on the accuracy if used in CPV performance estimation models - the quantum efficiency of a MJSC can vary greatly with small changes in wavelength.

3.4.7 Validation in low aerosol, low PW conditions

Both the SPCTRAL2 and SMARTS were designed with simulating atmospheric conditions prevalent on the mainland United States in mind. By

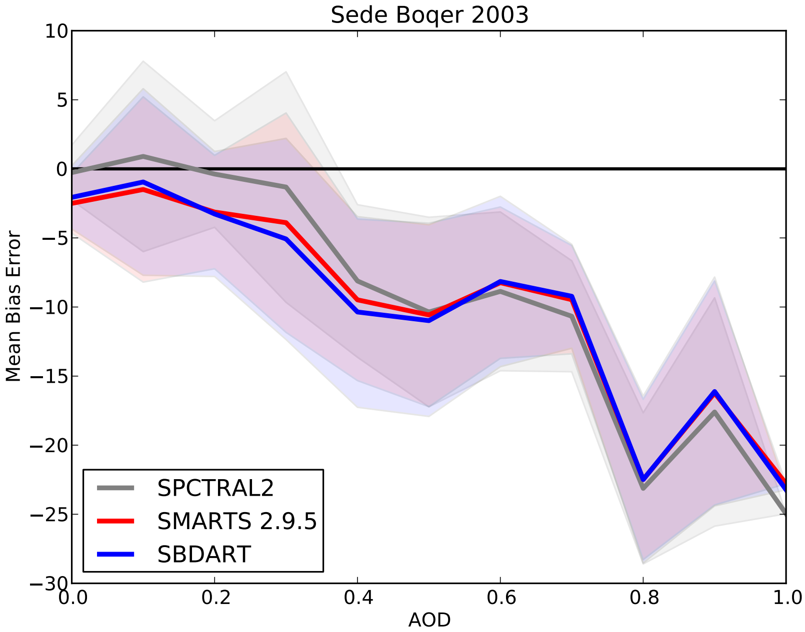

Figure 3.4: Mean bias error (MBE) as a function of AOD_{500}, in bins of 0.1.

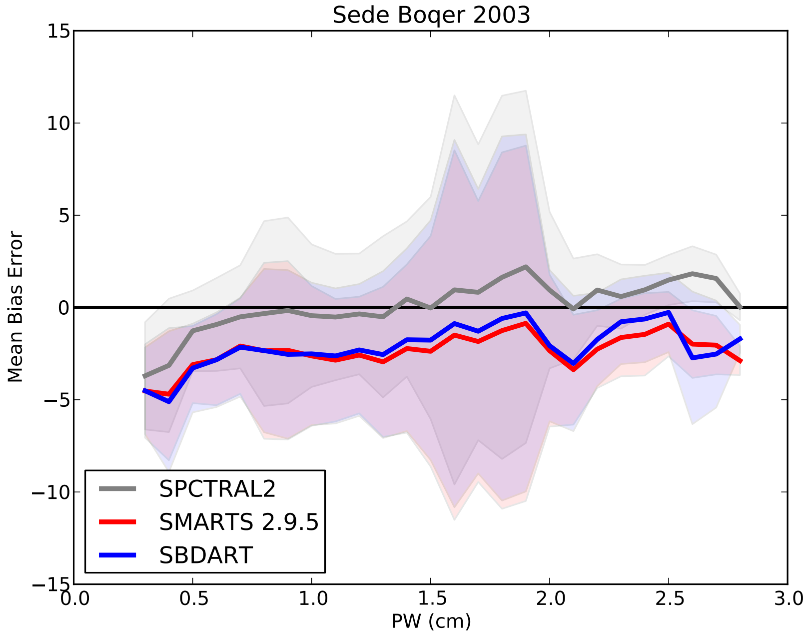

Figure 3.5: Mean bias error (MBE) as a function of PW, in 0.1cm bins.

only examining the range of atmospheric conditions that are generally encountered the southwestern United States (low aerosol optical depth, low precipitable water). AERONET measurements from the Rogers Dry Lake site are used as an example, with the data from Sede Boqer filtered such that they fall within the range of atmospheric conditions expected to be encountered at that location, summarised in Table 3.3.

Table 3.3: Atmospheric values encountered in southwestern US, taken from Rogers Dry Lake AERONET site

Atmospheric Parameter	Parameter Range
Air mass	1 - 5
Aerosol Optical Depth, 500nm	0.00 - 0.20
Precipitable Water	0 - 2.00 cm

The results, presented in Figure 3.6, show SPCTRAL2 as having the best agreement in terms of MBE, with SMARTS and SBDART offering small and comparable underestimates on between -1.4 and -1.8%. The similar RMSD values indicate the consistency is achieved across all radiative transfer codes.

From these results, the popularity of SMARTS within the solar energy community can be understood - it is a fast, relatively accurate radiative transfer tool that offers accuracy to within 1.8% in predicting integrated irradiance under atmospheric conditions encountered by most cell manufacturers, developers and installers, within the measurement error of field instruments. Outside of this parameter space, however, the accuracy of the simulations may vary.

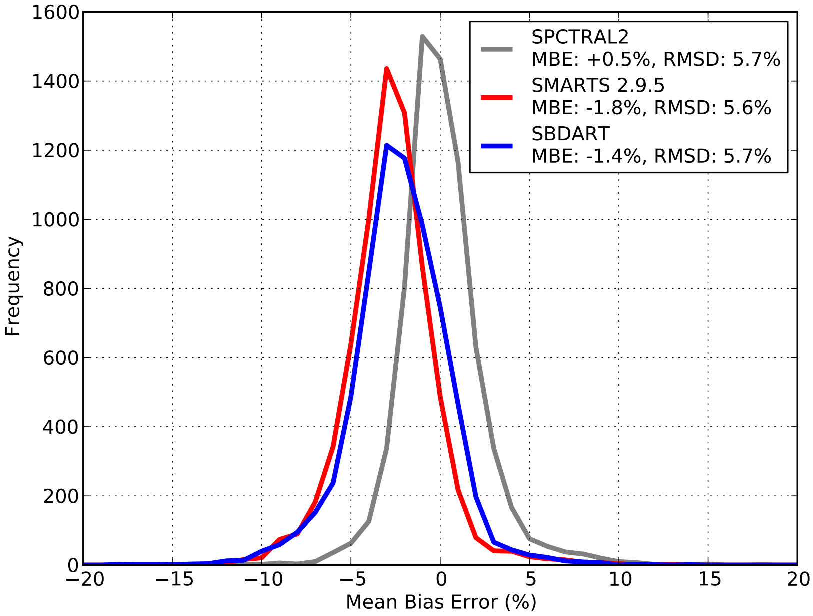

Figure 3.6: Validation of Radiative Transfer Models - Analysis for low AOD, low PW conditions. Number of datapoints: 6933.

3.4.8 Low irradiance performance

Here, the parameter has the largest influence on low irradiance predictions (DNI<400Wm−2, ≈4.4% of the number of datapoints) is determined, as well as the substantial under-estimates from radiative transfer models in this DNI range. SMARTS is used an example, although similar behaviour is noted for all three radiative transfer codes.

From Figure 3.3 and 3.5, there appears to be no significant change in MBE when precipitable water is varied. The calculation of air mass may contribute slightly towards any bias - the input file for SMARTS requires a local standard time and the timezone to calculate the solar zenith angle, and hence air mass. This is not optimal, as it requires a translation from the Coordinated Universal Time (UTC) linked to the AERONET records, and errors can occur during the calculation process, as there is a different between the Local Standard Time (LST, linked to the timezone) and Local

Apparent Time (LAT, very sensitive to the solar position). From Figure 3.4, however, model accuracy appears to be strongly dependent on aerosol loading.

From Figure 3.8, it can be seen that good agreement (within instrument uncertainty) is achieved by 400Wm^{-2}. Four distinct quadrants have been identified to examine the accuracy under different conditions. These include low AOD, low air mass (AOD<0.2, AM<2.5); low AOD, high airmass (AOD<0.2, AM>2.5); high AOD, low air mass (AOD>0.2, AM<2.5) and high AOD, high air mass (AOD>0.2, AM>2.5). The number of datapoints under 400Wm^{-2} in each quadrants is given.

The majority of the datapoints below 400Wm^{-2} occur under high aerosol loading and low air mass conditions. With relatively few datapoints at low irradiance with low aerosol loading, it is difficult to draw a conclusion regarding model performance for those conditions - but the limited data available indicates that SMARTS may overestimate the DNI resource given those parameters.

In Figure 3.8, the MBE trend for high AOD conditions, at both high and low air mass, show negative values at low irradiance conditions, indicates an underestimation of DNI. This is confirmed by calculating the Spearman's rank coefficient, examining the correlation between ΔDNI and AOD$_{500}$. A strong negative correlation was noted for all atmospheric models, signalling underestimation gets more severe as the aerosol loading increases. The distribution in MBE and RMSD and the associated statistics for points with measured DNI below 400Wm^{-2} is given in Figure 3.7, whilst Spearman's rank coefficients are given in Table 3.4.8.

Further differentiation between the models can be achieved by examining the effectiveness of the 2-tier Angström exponent approximation used. In SPCTRAL2, the aerosol optical depths at all wavelengths other than 500nm are extrapolated using a single Angström exponent. In SMARTS, the aerosol optical depths at all wavelengths greater than 500nm are extrapolated using two Angström exponent (a separate exponent is used for <500nm)- in real aerosols, this approximation is often overly simplified,

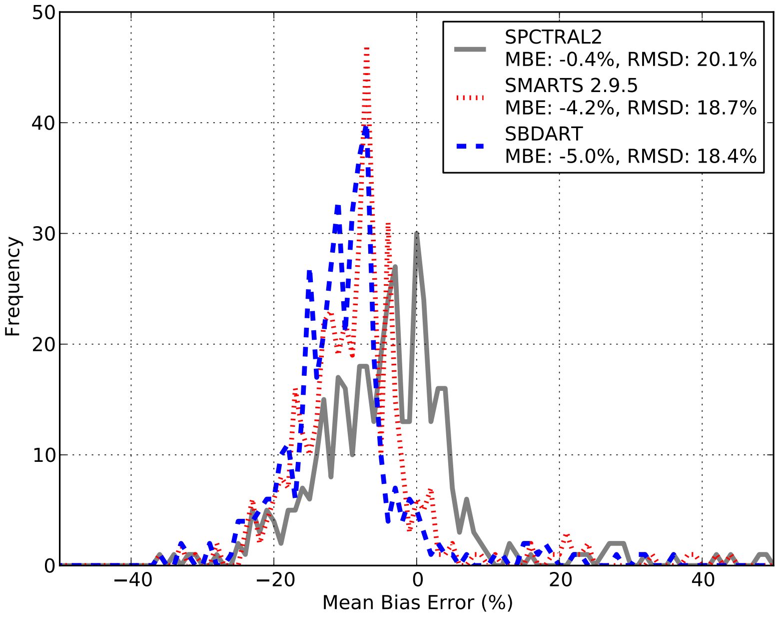

Figure 3.7: Validation of Radiative Transfer Models - MBE and RMSD for low irradiance conditions. A greater negative MBE bias is seen, along with elevated RMSD values, indicating less consistency than under high DNI conditions.

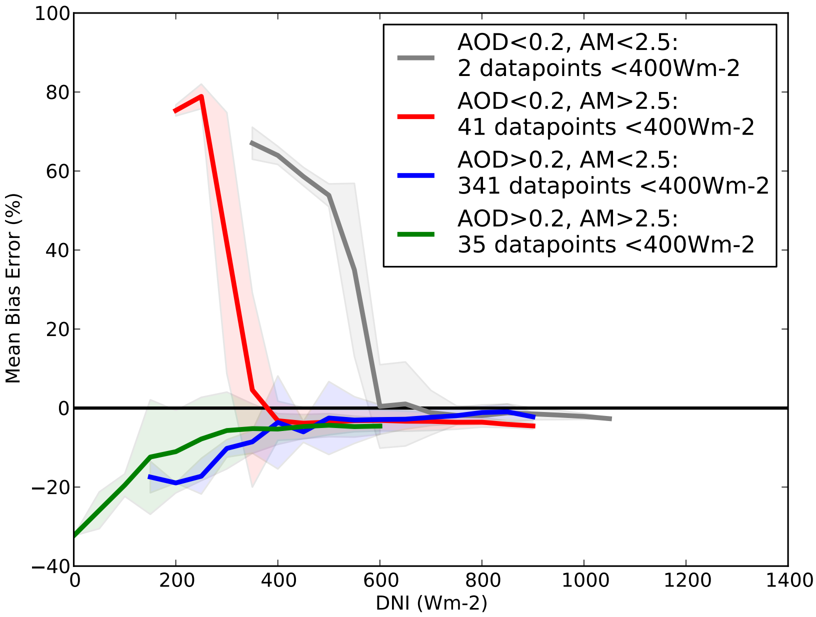

Figure 3.8: Validation of Radiative Transfer Models - Analysis for low irradiance conditions. High AOD values appear to be primarily responsible for the negative MBE values at low irradiance conditions, indicating an underestimation of DNI.

Parameter	**SPCTRAL2**	**SMARTS**	**SBDART**
AOD_{500}	-0.6693	-0.5624	-0.5427
α’	-0.1651	-0.0152	+0.086

Table 3.4: Spearman’s Rank Correlation Coefficients for ΔDNI and AOD_{500}, AOD curvature. SPCTRAL2 exhibits greater negative correlation with curvature, an indicator of the effectiveness of using a single Angström exponent to extrapolate AOD.

with the Angström exponent changing with wavelength. In this way, the extrapolation from SMARTS may lead to significant errors in the predicted DNI, particularly in conditions where the aerosol loading is high and this discrepancy is amplified, as illustrated in Figure 3.9.

The curvature in the aerosol optical depth measurements are calculated as detailed in [170] and examined its correlation with DNI prediction accuracy at high AOD values ($AOD_{500} > 0.2$). This is given by the curvature in $ln\tau_a$ versus $ln\lambda$ and expressed in mathematical form in Equation 3.7. Reasonable correlation exists between the first derivative of the Angström exponent (α') and ΔDNI for SPCTRAL2, but is almost negligible for SMARTS. The results indicate that with greater curvature, the MBE value for SPCTRAL2 decreases, indicating a stronger negative bias, whilst SMARTS is relatively unaffected, and greater curvature actually leads to an increase in MBE for SBDART, a possible effect of its method for calculating AOD. The correlation coefficients are given in Table 3.4.8.

$$\begin{aligned}\alpha' = \frac{d\alpha}{dln\lambda} = -\left(\frac{2}{ln\lambda_{1020nm} - ln\lambda_{500nm}}\right) \times \\ \left(\frac{ln\tau_{a,1020nm} - ln\tau_{a,870nm}}{ln\lambda_{1020nm} - ln\lambda_{870nm}} - \frac{ln\tau_{a,870nm} - ln\tau_{a,500nm}}{ln\lambda_{870nm} - ln\lambda_{500nm}}\right)\end{aligned} \tag{3.7}$$

3.5 Summary

The SPCTRAL2, SMARTS 2.9.5 and SBDART radiative transfer tools have been evaluated against measurements of *integrated* direct normal irradiance. The statistics of their performance were analysed at a variety of irradiance

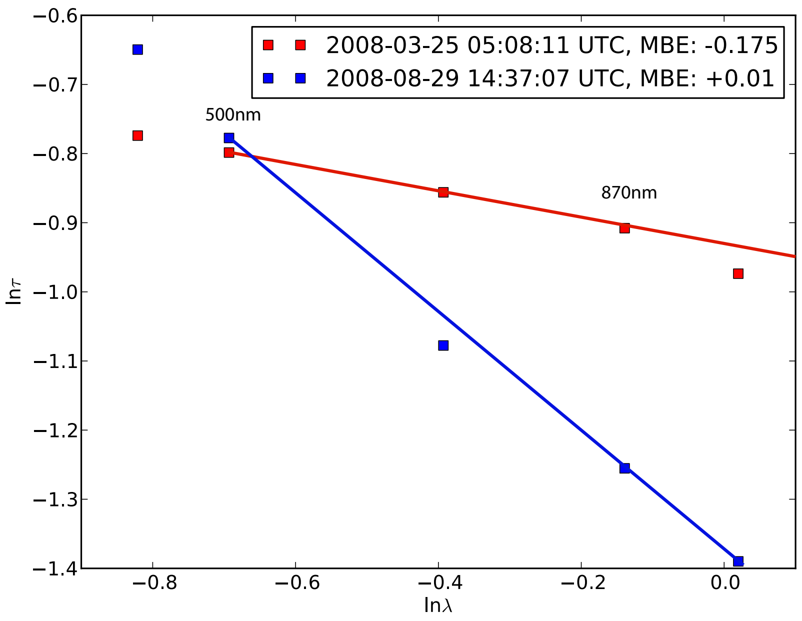

Figure 3.9: Validation of Radiative Transfer Models - Angström exponent issues. A change in α with wavelength can affect the accuracy of radiative transfer models. Here, two datapoints with similar air mass and AOD_{500} values are plotted, one with significant AOD curvature (red), and the with negligible curvature (blue). This is particularly important for high aerosol loading and relatively low Angström exponents.

levels and under a range of atmospheric conditions, using the metrics of mean bias error and root mean squared deviation.

All radiative transfer tools show similar levels of uncertainty at DNI values greater than 400Wm^{-2}, but the mean bias error can vary from model to model. SPCTRAL2 shows the least bias in this particular situation, but its coarse absorption spectra resolution, inability to modify the acceptance angle and its use of a single Angström exponent to extrapolate AOD may have an impact on the spectral accuracy of any simulated solar spectra.

SBDART performs well at reasonable irradiance values, offering a slight improvement over SMARTS 2.9.5 in terms of mean bias. Its computational overhead currently limits its use in spectral irradiance simulations for CPV systems, where thousands of spectra may need to be simulated quickly. It does, however, offer additional functionality, such as attenuation due to clouds and creation of multiple aerosol layers, which may become important considerations in the future.

SMARTS 2.9.5 is shown to be acceptable in terms of integrated DNI, provided the DNI is above 400Wm^{-2}. Below this level, the Mean Bias Error and RMSD are large, and investigations indicate the discrepancy at low irradiances (under cloudless conditions) is likely due to the treatment of aerosols used in the model. This radiative transfer tool strikes a balance between speed, accuracy and flexibility in terms of aerosol representation, and will be used for the simulations outlined in the following chapters.

It is crucial to note that the *spectral irradiance*, the distribution of solar irradiance as a function of wavelength, has not been examined here - there are few available sources of good-quality, spectrally resolved DNI measurements in locations with sufficiently varied atmospheric conditions, summarised in Table 3.5. Further examination of the spectral accuracy of these models is needed for more challenging spectral conditions when sufficient data becomes available.

Resource	**Measurements**	**Locations**
BSRN [143]	GHI, DNI, Diffuse, integrated	Worldwide
NREL - Solar Radiation Research Laboratory [171]	GHI, DNI, spectrally-resolved	United States
National Solar Radiation Database [156]	Hourly GHI, DNI, Diffuse, integrated	United States
SKYNET [172]	GHI, DNI, Diffuse, integrated	Asia

Table 3.5: Publicly available solar resource ground measurements for CPV systems, all with sub-hourly temporal resolution unless otherwise stated.

4 Radiative Efficiency and Optimal Band Gaps

In any solar cell, the balance of photogeneration and recombination determines the performance and gives rise to a set of optimum band gaps. The radiative limit represents the lowest permissible level of recombination in a solar cell and therefore places an upper limit on the voltage that can be attained. Realistic, practical solar cells operate below this limit, where non-radiative recombination takes on greater importance. Non-radiative recombination is often caused by trap states created by imperfections in the material, due to impurities, point or line defects [173]. Increased recombination will reduce the performance of a solar cell, and is particularly relevant for multijunction devices, operated under high concentration (hence high bias) with a high device voltage. Taking increased recombination into consideration can result in substantially different power outputs.

Currently, there are no methods that provide a reasonable way of comparing material quality across different material systems, and examining their impact on the band gaps of optimal designs. This section will summarise the existing methods and propose a novel way of evaluating material quality and its influence on the band gaps of optimal solar cell designs under different solar spectra.

In the past, the etaOpt computer model was developed at the Fraunhofer Institute for Solar Energy [174], investigating the optimal band gaps for single junction and tandem solar cells that operate at the detailed balance limit identified by Shockley and Queisser in 1961 [29], and where only radiative recombination is examined.

A way of accounting for realistic recombination in MJSCs is provided by

Spectrolab [175], where the concept of a *band gap-voltage offset* is introduced in an attempt to move away from the detailed balance limit. This figure of merit describes the difference between the band gap of a junction and its achieved V$_{OC}$, and is calculated for a range of experimentally achieved materials. The results described in [175] concerns the realistic performance projections of 4-, 5- and 6-junction devices.

In this thesis, an equivalent measure of semiconductor quality, termed *radiative efficiency*, is introduced, allowing cell performance predictions to be generated with a simple yet effective approach. Tools used to model the performance of solar cells often require substantial sets of parameters describing the carrier transport properties within each junction or device data measured from newly manufactured solar cells. The more generalised approach detailed in this thesis allows for an estimate of non-radiative recombination current to be obtained, given a fairly small number of spectroscopic parameters. The recombination attributed to each type is quantified, and a standardised measure of material quality applicable across a range of material systems is detailed. Further, optimal band gaps for solar cells are calculated with realistic radiative efficiencies under a range of concentrations, and a comparison is offered with results from an existing method.

4.1 Definition of material quality

Past efforts to calculate the optimal band gap combinations for multi-junction devices have taken a single-diode approach, either using empirical data [176] or consider solely radiative recombination [58,174,177,178]. The majority of photovoltaic devices do not approach this theoretical limit, as non-radiative recombination is present in real devices. With greater non-radiative recombination, the current-voltage characteristics of the solar cell change, resulting in decreased open circuit voltage (V_{OC}) and lower cell efficiency. A recent publication [175] examining the V_{OC} offset in single junction devices has provided insight into material quality of a particular cell. It does not, however, break down the analysis into the radiative and non-radiative components.

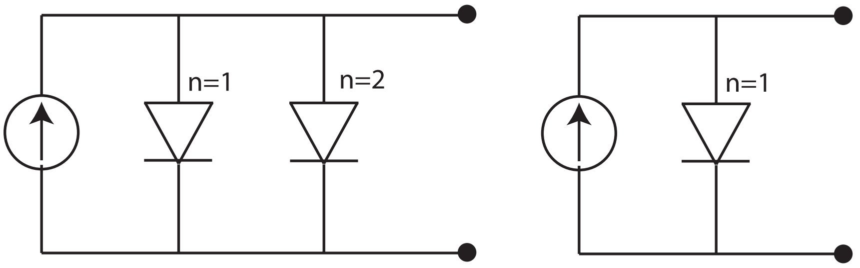

Figure 4.1: One- and two-diode equivalent circuits for considering recombination mechanisms in each junction of a multi junction device. Parasitic resistances not included.

Multijunction devices can be modelled as series-connected diodes [179] with each junction described by the well-studied two-diode model [57], summarised by Equation 4.1 and illustrated in Figure 4.1, where n=1 represents bi-molecular recombination, assumed to be solely radiative, and n=2 describes non-radiative Shockley-Read-Hall (SRH) recombination in the depletion region of the device, assuming all SRH recombination occurs in the depletion region and that there are the population of holes and electrons is approximately equal.

To simulate the projected performance of the structures in this work, the MJSC device is modelled as multiple diodes connected in series. The recombination current in each diode can be approximated using the standard two-diode model. One component, J_{01}, describes bi-molecular recombination, which is assumed to be radiative, while the other mono-molecular component, J_{02}, describes non-radiative Shockley-Read-Hall (SRH) recombination in the depletion region [57, 175]:

$$J_{dark}(V) = J_{01}(e^{\frac{qV}{k_B T}} - 1) + J_{02}(e^{\frac{qV}{2k_B T}} - 1) \tag{4.1}$$

The photon flux from radiative recombination is a fundamental property of a given semiconductor, fixed by the joint-density of states and oscillator strength. It can be estimated by assuming that the onset of absorption (and emission) occurs at the band gap energy, and that the probability of absorption (and emission) is unity. This enables the internal, isotropic, emission from a semiconductor of refractive index n to be described by a generalised form of the Planck equation [180]:

$$N = \frac{2\pi n^2}{4\pi^3\hbar^3c^2}\int_{E_g}^{\infty}\frac{E^2}{e^{\frac{E-\mu}{k_BT}}-1}dE \tag{4.2}$$

where N is the emitted photon flux density, E is the photon energy, k is the Boltzmann constant, h is Plancks constant and μ is the difference in electrochemical potential between the electron and hole populations. Using Equation 4.2, applying the Boltzmann approximation, and integrating, an analytical expression is obtained:

$$N = \frac{2\pi n^2}{4\pi^3\hbar^3c^2}e^{\frac{-E_g}{k_BT}}(E_g^2 + 2E_gk_BT + 2k^2T^2)e^{\frac{q\mu}{k_BT}} \tag{4.3}$$

where E_g is the material band gap, T is the temperature of the device and q is the electron charge. Thus, J_{01} can be estimated by converting the photon flux into current and assuming the application of a bias V=μ

$$J_{01} = \frac{2q\pi n^2}{4\pi^3\hbar^3c^2}e^{\frac{-E_g}{k_BT}}(E_g^2 + 2E_gk_BT + 2k^2T^2) \tag{4.4}$$

In Equation 4.4, non-radiative recombination in the neutral regions, which requires the non-radiative lifetime there to be long when compared to the radiative lifetime, is neglected.

Since the total current through a solar cell can be expressed as:

$$J_{Total}(V) = J_{SC} - J_{01}(e^{\frac{qV}{k_BT}} - 1) - J_{02}(e^{\frac{qV}{2k_BT}} - 1) \tag{4.5}$$

where the sign of the current is chosen so that positive currents correspond to carrier generation. Within the assumption of a fully radiative J_{01} term, the radiative efficiency of the device near the operating bias can be written as:

$$\eta_{rad}(V) = \frac{J_{01}(e^{\frac{qV}{k_BT}} - 1)}{J_{01}(e^{\frac{qV}{k_BT}} - 1) + J_{02}(e^{\frac{qV}{2k_BT}} - 1)} \tag{4.6}$$

where η_{rad} gives an estimate of the fraction of recombination processes due to the intrinsic, radiative mechanism in a particular device. It can be regarded as a measure of the device quality, related to the presence of defects and other recombination centres. It is evident from Equation 4.6 that the radiative efficiency is a strong function of device voltage V - for large values of V, the contribution from terms associated with J_{01} will outweigh that from J_{02}, due to its n=2 dependence.

To compare materials with different band gap energies, choose an arbitrary reference level of injection is chosen, corresponding to a J_{SC} of 30 mA/cm^2, close to the 1-Sun short-circuit current density of a single-junction GaAs solar cell. Under open-circuit conditions, i.e. $J_{total}(V)=0$, radiative efficiency for a given cell can be defined as:

$$\eta_{rad}(V_{OC,REF}) = \frac{J_{01}(e^{\frac{qV_{OC,REF}}{k_B T}} - 1)}{J_{SC,REF}} \tag{4.7}$$

where $J_{SC,REF}$= 30 mA/cm^2, and $V_{OC,REF}$ corresponds to the V_{OC} associated with $J_{SC,REF}$, given by:

$$V_{OC,REF} = \frac{2k_B T}{q} \ln \left\{ \frac{J_{02} + \sqrt{J_{02}^2 + 4J_{01}(J_{SC,REF} + J_{01} + J_{02})}}{2J_{01}} \right\} \tag{4.8}$$

Furthermore, J_{02} can be expressed in terms of J_{01}, J_{sc}, and V_{OC} through:

$$J_{02} = \frac{J_{SC} - J_{01}\left(e^{\frac{qV_{OC}}{k_B T}} - 1\right)}{e^{\frac{qV_{OC}}{2k_B T}} - 1} \tag{4.9}$$

With this theoretical background, and drawing on the experience of a previous publication [181], radiative efficiency is now used as a figure of merit to parameterize the performance of experimentally demonstrated single-junction III-V devices, with J_{SC}, V_{OC}, E_g and T as input parameters. To establish a baseline, the radiative recombination component of the current, J_{01}, is first calculated from Equation 4.4. The non-radiative recombination component of the current, J_{02}, is given by fitting the V_{OC} using Equation 4.9. With the two components of the recombination current, a radiative efficiency is then determined at the reference current density of 30 mA/cm^2 using Equations 4.7 and 4.8.

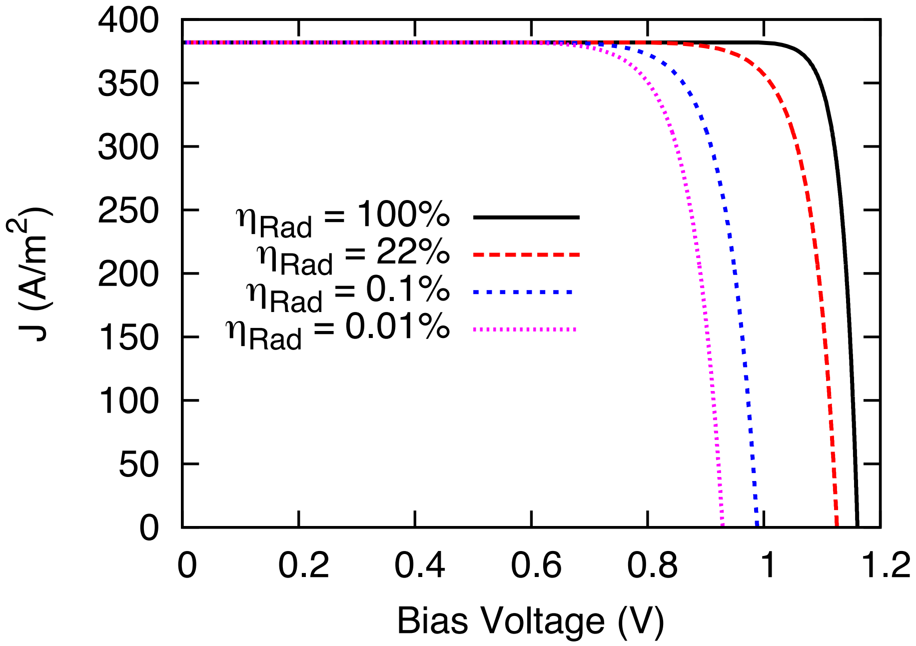

Figure 4.2: Current density vs. voltage for a single- junction GaAs solar cell under 1-Sun AM0 illumination, at a range of radiative efficiencies. Lower radiative efficiencies indicate lower diode quality, and greater non-radiative recombination. Moving away from the radiative limit incurs penalties in V_{OC} and maximum power point voltage (V_{MPP}).

4.2 Validation of radiative efficiency methodology

Through applying series-connected constraints, multi- junction devices can be simulated through combining J-V curves for all junctions. Example J-V curves are shown in Figure 4.2 for a single-junction device with a band gap of 1.42 eV at a range of radiative efficiencies.

A single-junction GaAs device detailed in [182] has been simulated with η_{rad}=22% and the modelled I-V curve compared against experimental results in Figure 4.3. Other essential cell characteristics are also shown in Table 4.2. In general, good agreement between simulation and experiment can be noted. The discrepancy in fill factor between measurement and simulation is likely attributable to photon management within the device, which is not modelled.

Parameter	**Experiment**	**Simulation**
J_{SC} (mA/cm^2)	27.89	27.89
V_{OC} (V)	1.029	1.031
Fill Factor (%)	86.4	81.9
Efficiency (%)	24.8	23.5

Table 4.1: Electrical characteristics for an experimentally measured and simulated single junction GaAs solar cell under AM1.5G illumination. A radiative efficiency of 22% was used for the simulation. Close agreement is noted with most parameters.

4.3 Changes in radiative efficiency

Situations exist where one could expect radiative efficiency to deviate from the previously stated values when junctions are grown on substrates with mismatched lattice constants, or when the solar cell is irradiated by energetic particles as in a space radiation environment, increasing the defect density and hence the rate of non-radiative recombination.

By performing these calculations for various materials using published data sources of I-V curves for single-junction and isotype MJSCs [61, 65, 118, 119, 175, 179, 182–195], η_{rad} values ranging from up to 20% for InGaP, 40% for GaAs, and 35% for InGaAs devices are obtained. Since the quoted η_{rad} values are always calculated at the same reference current density, they do not necessarily correspond to the performance characteristics of a particular solar cell, but rather enable comparisons to be made across different types of single- and multijunction devices.

4.3.1 Radiative efficiency as a function of lattice-mismatch

Figure 4.4 shows the radiative efficiency as a function of lattice mismatch for GaAs, InGaP and InGaAs solar cells grown on various substrates, including

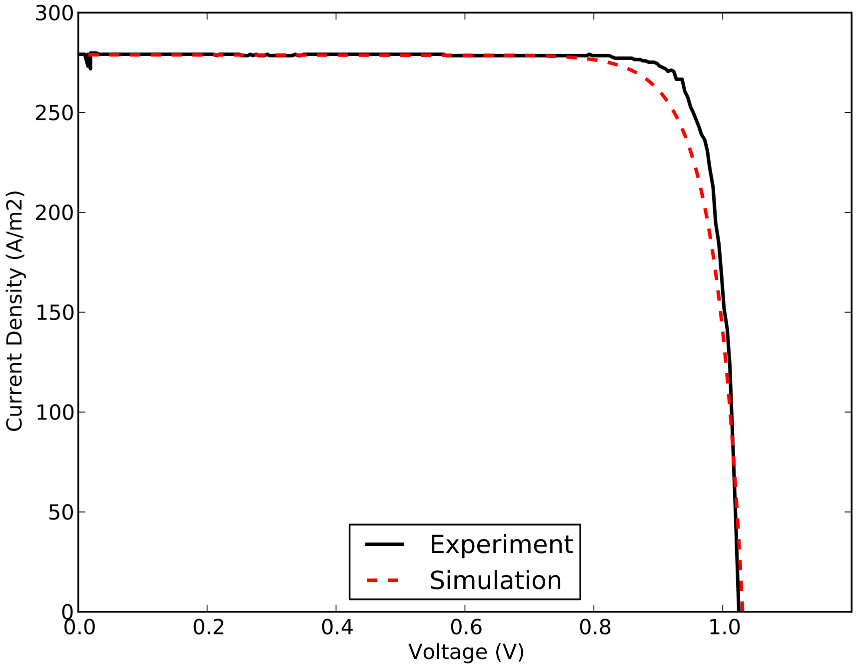

Figure 4.3: Experimentally measured and simulated illuminated I-V curves for a single-junction GaAs device under AM1.5 Global illumination. A radiative efficiency of 22% was used for the simulation, and the curves demonstrate reasonable agreement for lattice-matched junctions. Experimental data extracted from [182]

GaAs and Ge, the current substrates of choice for multijunction technologies. As seen from Figure 4.4, radiative efficiency values of approximately 40% can be found for the best lattice-matched materials, and display a monotonic decrease with the amount of mismatch. A fit to the data showed that the radiative efficiency for the devices considered in this work decreases exponentially as the mismatch increases with a decay constant of $\approx$ -1.5%. Lattice-mismatch is defined as:

$$Lattice\ Mismatch = \frac{\mathring{A}_{substrate} - \mathring{A}_{junction}}{\mathring{A}_{junction}} \tag{4.10}$$

where $\mathring{A}$ represents the lattice constant of the material in question, in units of Ångströms (1x10^{-10}m).

For an inverted metamorphic device, the lattice mismatch becomes important, particularly for the InGaAs bottom junction. From the fitting of radiative efficiency as a function of mismatch, the two lattice-matched junctions are assumed to have radiative efficiencies of 22%, whilst the mismatched bottom 1 eV junction has a much lower radiative efficiency of 0.23%. Figure 4.5 shows that the model closely reproduces the experimental illuminated I-V curve for the IMM cell under the AM0 spectrum. In the future, IMM MJSCs with two relaxed sub-cells may be demonstrated.

At this point, it is useful to note that the radiative efficiency is dependent on material quality and may vary for different growth and/or processing conditions. With improvements in growth and processing techniques, material quality is expected to rise with time, and the change in radiative efficiency over the past few decades is examined.

4.3.2 Evolution of radiative efficiency with time

As with any technology, one would expect the material quality to rise with time. Due to improved manufacturing processes, this is observed in InGaP, InGaAs and GaAs devices. A plot showing this improvement is given in Figure 4.6

A large spread in radiative efficiency is present in the 2008-2011 time-

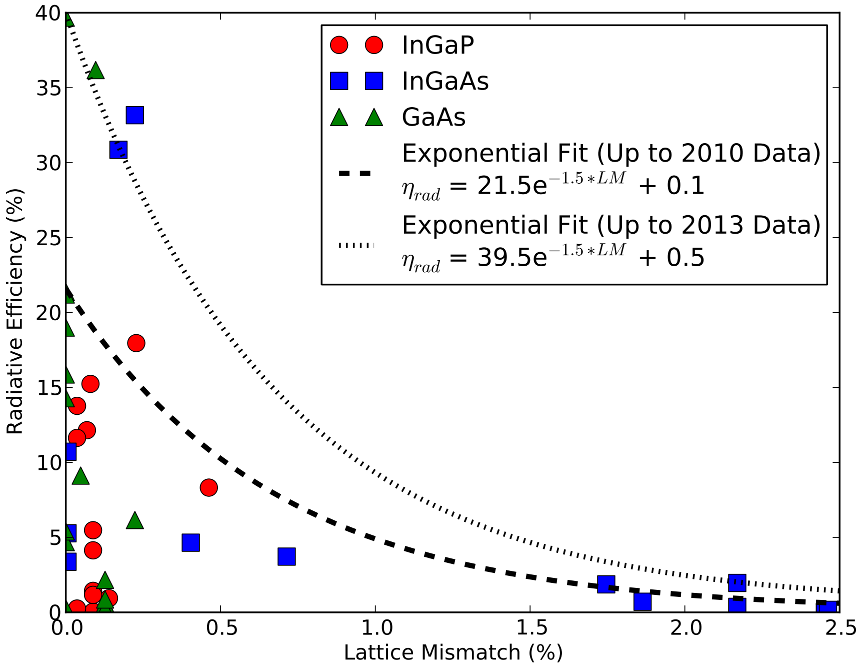

Figure 4.4: Change in radiative efficiency with lattice mismatch. A fit to the data shows the radiative efficiency for the devices considered here decreases exponentially with an increase in lattice mismatch, with the fits presented on the graph.

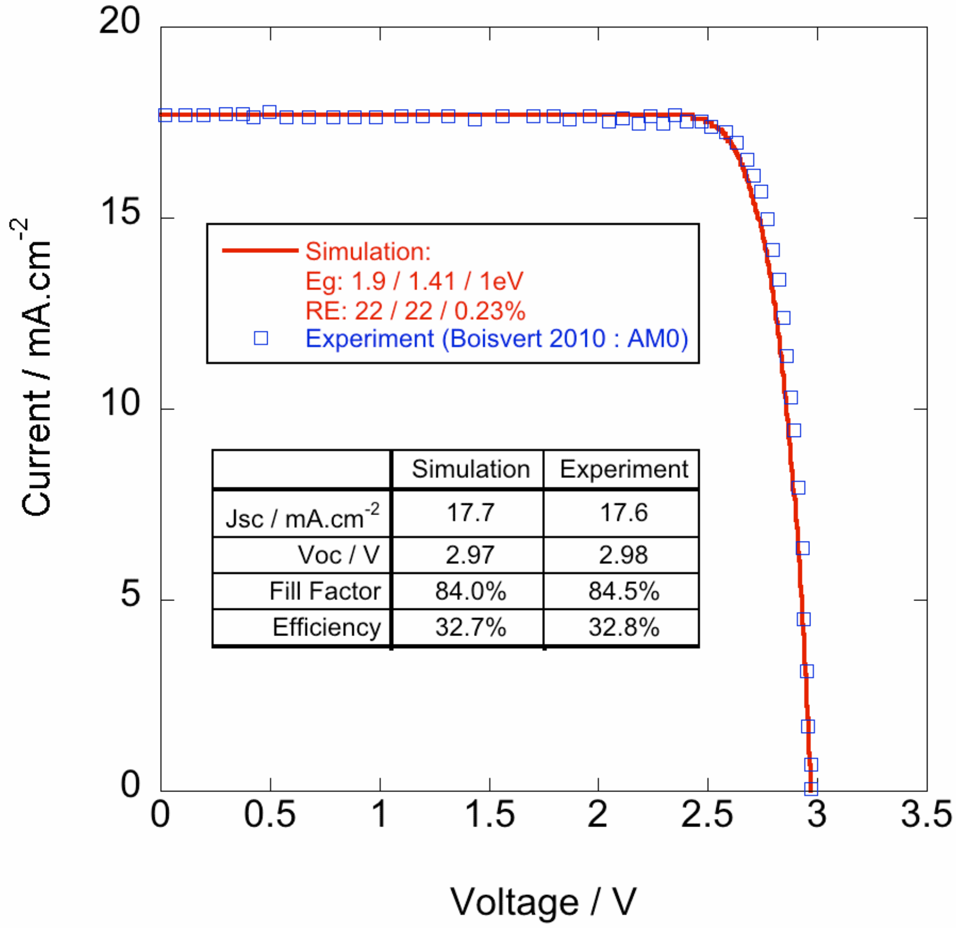

	Simulation	Experiment
Jsc / mA.cm^{-2}	17.7	17.6
Voc / V	2.97	2.98
Fill Factor	84.0%	84.5%
Efficiency	32.7%	32.8%

Figure 4.5: Validation of the radiative efficiency model through simulation of the illuminated I-V curve for an IMM InGaP/GaAs/InGaAs solar cell. The experimental data was extracted from [196].

frame, as the concept of lattice-mismatched growth gains popularity, due to its ability to reach band gaps that were not possible with traditional lattice-matched growth.

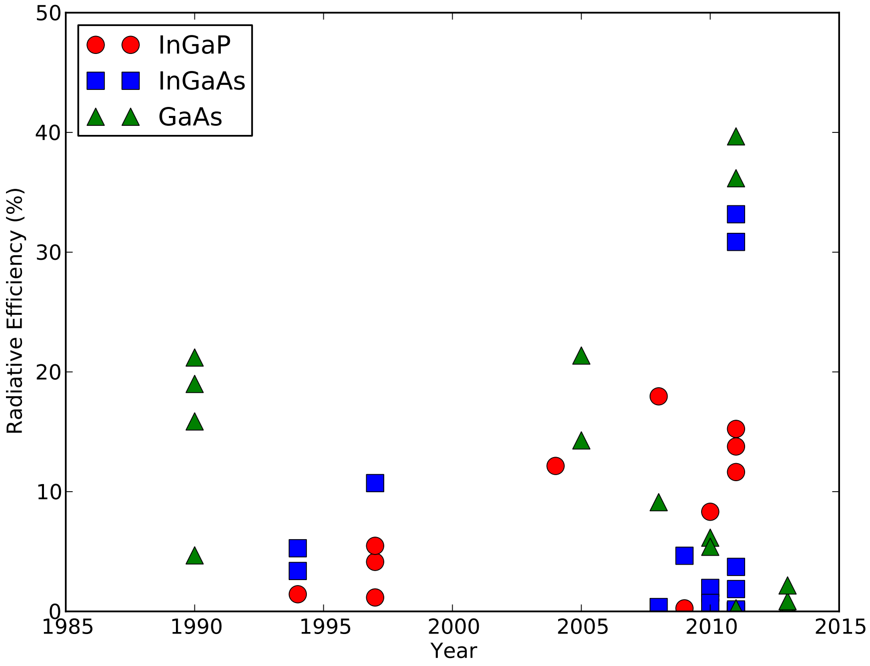

Figure 4.6: Improvement in Radiative Efficiency with Time for GaAs, InGaP and InGaAs devices surveyed.

4.4 Optimal Band Gaps - Unconcentrated Sunlight

Optimal band gap calculations have been discussed by numerous authors [58, 177, 197], using a numerical approach that examines all possible band gaps and calculates their output power, given appropriate semiconductor electronic behaviour. In all these approaches, the authors have only included radiative losses, i.e. the calculations were performed at the radiative limit. The work in this chapter moves beyond this assumption, to account for non-radiative losses in devices with material quality that are representative of practical solar cells. A numerical approach is applied where all possible band gap combinations are simulated, from which the optimal band gap is determined.

Single-, dual- and triple-junction structures, with quantum efficiency values of 0.98 at wavelengths above band gap of the junction and below the band gap of the preceding junction, have been modelled at a range of radiative efficiencies. Photon recycling has not been considered. Each device is two-terminal and series-constrained, with parasitic resistance losses not considered due to strong dependence on processing techniques. The optimal band gap combination, defined by the highest power output, is calculated for each radiative efficiency value.

Under the ASTM E-490 Air Mass Zero (AM0) spectrum at 1-sun concentration, a clear trend of higher band gaps with lower radiative efficiency is demonstrated, illustrated by Figures 4.7 and 4.8, for single- and dual-junction devices respectively. Triple junction devices follow a similar trend, with a selection of values listed in Table 4.4. This matches the pattern noted by Shockley and Queisser in their publication dealing with the detailed balance limit [29].

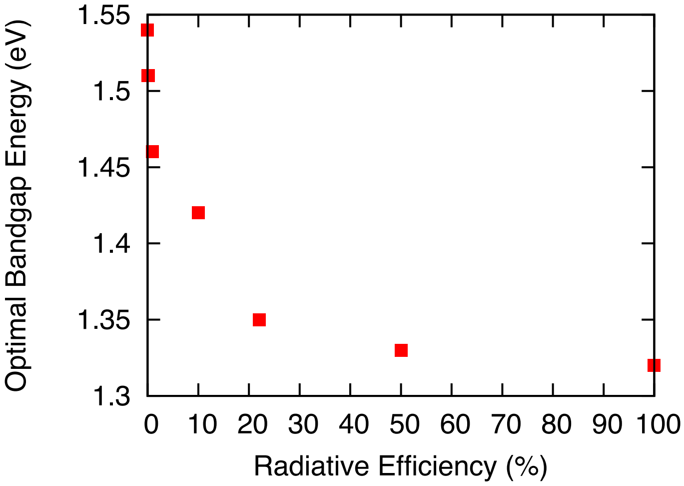

Figure 4.7: Optimal band gap as a function of radiative efficiency for a single-junction device under 1X AM0 illumination.

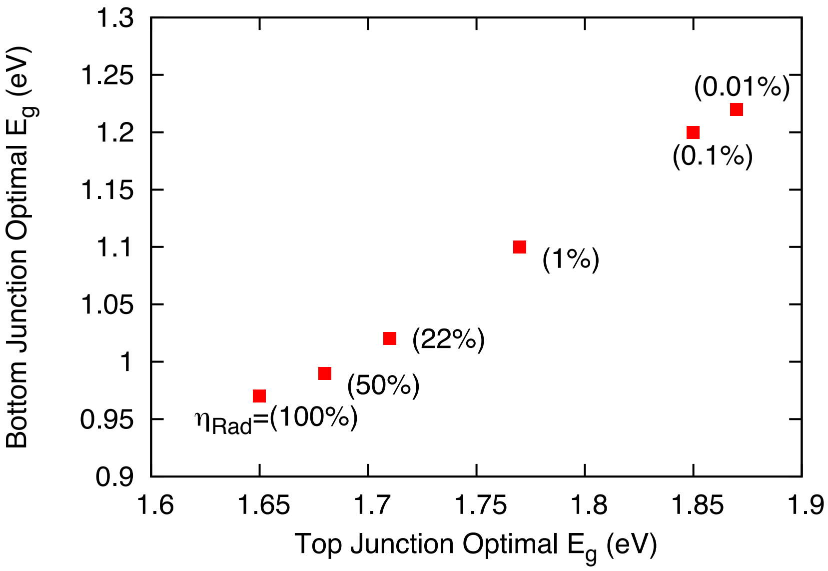

Figure 4.8: Optimal top and bottom junction band gap energies for a dual-junction device, under 1X AM0 illumination. The radiative efficiency for each band gap combination is shown in brackets. Optimal band gap values increase with lower radiative efficiencies to compensate for voltage loss.

η_{rad} (%)	**Eg$_1$(eV)**	**Eg$_2$(eV)**	**Eg$_3$(eV)**	**Efficiency (%)**
100	1.89	1.27	0.83	43.45
22	1.94	1.32	0.87	38.27
1	1.99	1.39	0.95	34.34
0.1	2.00	1.41	0.97	31.86

Table 4.2: Optimal junction band gaps for a triple- junction device as a function of radiative efficiency, under 1X AM0 illumination

At the radiative limit, a junction possesses the highest achievable voltage. When non-radiative recombination is considered, the J_{02} term in Equation 4.1 becomes non-zero and reduces the current produced. Figure 4.2 demonstrates this effect graphically for a single junction, showing a drop in operating voltage, where maximum power is produced. Such behaviour is often signalled by a reduction in the fill factor (FF) of a device.

By raising the band gap, the reduction in operating voltage can be counteracted, but a penalty is incurred in terms of current produced. It also follows logically that with greater non-radiative recombination and hence lower diode quality, the efficiency of a device will drop.

For a multijunction device, current-matching conditions add complexity, but the effect of poor diode quality on individual junctions remains similar - band gaps must rise to compensate for greater non-radiative recombination.

4.5 Optimal Band Gaps - Concentrated Sunlight

A similar approach has been undertaken using a 500-Sun AM1.5D spectrum to investigate the effects of changing radiative efficiency on terrestrial concentrator systems. In this case, there is no significant change in the optimal band gaps with change in radiative efficiency, as illustrated in Table 4.3.

η_{rad} (%)	**Eg_1(eV)**	**Eg_2(eV)**	**Eg_3(eV)**	**Efficiency (%)**
100	1.75	1.18	0.70	54.40
22	1.75	1.18	0.70	53.61
1	1.75	1.18	0.70	50.96
0.1	1.76	1.19	0.70	47.94

Table 4.3: Optimal junction band gaps for a triple- junction device as a function of radiative efficiency, under 500X AM1.5D illumination

Such behaviour can be understood as a consequence of increased short circuit current, J_{SC}. It follows that the voltage associated with the maximum power point at high concentrations has increased. A shift to higher bias leads to dominance of J_{01} in the dark current, shifting the device operation towards the radiative limit, where recombination is solely attributable to radiative processes. Figure 4.9 illustrates this with a plot of the components of dark current as a function of bias.

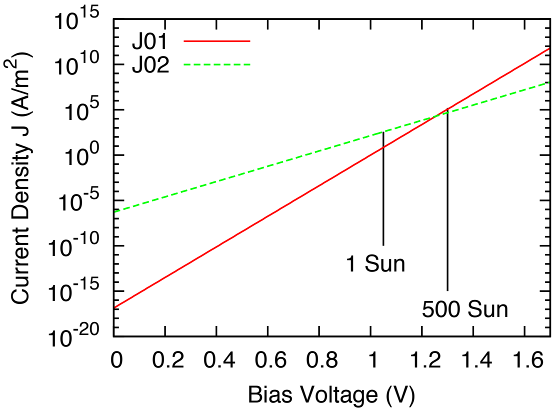

Figure 4.9: Components of dark current in an example single-junction device with E_g=1.42eV and η_{rad}=22%. Here, J_{01} and J_{02} represent radiative and non-radiative recombination respectively. The contribution of each component is highlighted for V_{OC} conditions at 1-Sun and 500-Suns by the vertical lines.

At high concentrations, regardless of the junctions radiative efficiency at open circuit voltage, J_{01} is several orders of magnitude larger than J_{02}. Radiative recombination processes therefore dominate, resulting in similar optimal band gaps for all radiative efficiencies. Single-junction device optimal band gap energies converge, regardless of diode quality, shown in Figure 4.10.

In addition, the optimal band gaps for various values of concentration of the AM0 and AM1.5D spectra have been calculated and similar behaviour is noted in both cases. With the AM1.5D terrestrial spectra, the presence of atmospheric absorption bands leads to pinning of the optimal band gaps at certain energies before a sudden change. This behaviour is illustrated in the single-junction case in Figure 4.11. With the smooth AM0 extraterrestrial spectrum, this effect is absent. However, in both cases the optimal band gap energies converge at high irradiance concentrations.

Under high concentration, radiative recombination processes dominate, regardless of radiative efficiency. For dual- and triple-junction devices, the situation is similar the optimal band gap energies of poor diode quality

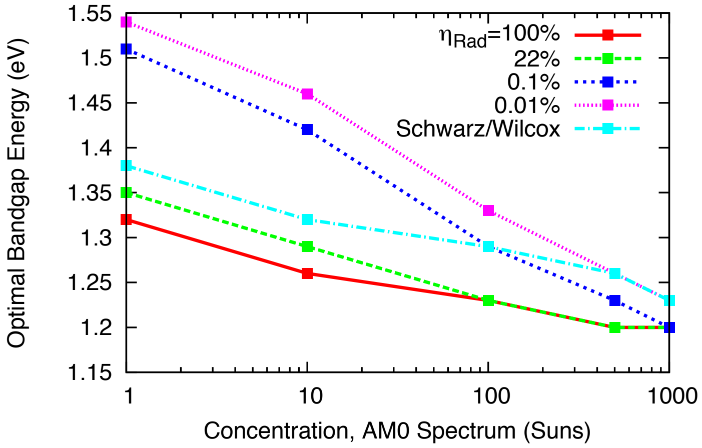

Figure 4.10: Optimal band gaps for a single-junction device as a function of irradiance concentration under the AM0 spectrum. Values converge at high concentration due to high device bias and the dominance of the n=1 recombination term, assumed to comprise radiative recombination.

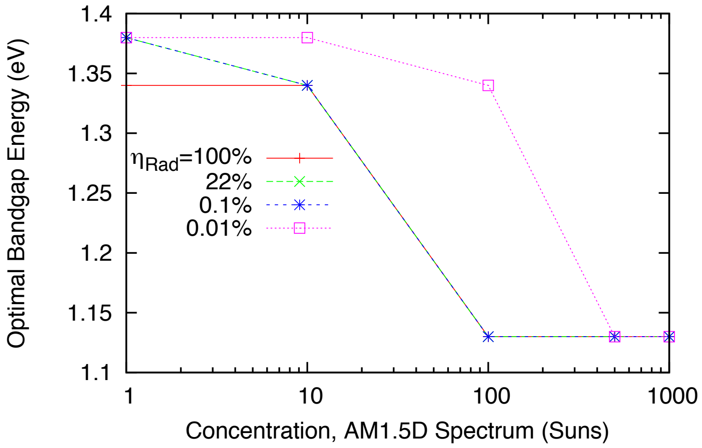

Figure 4.11: Optimal band gaps for a single-junction device as a function of irradiance concentration under the AM1.5D spectrum. The sudden change in optimal band gaps is a result of absorption bands in the terrestrial spectrum.

devices are 100s of meVs greater than those of good diode quality at low concentrations, with convergence in the values at high concentrations. In Figure 4.12 an example is shown for the triple-junction case under AM1.5D illumination at various concentration values, for each individual junction.

An alternative solution has been considered, and the optimal band gaps as a result of their application are also shown. A method for estimating J_0 is given in recent publications by Wilcox et al. [198], where a 1-diode model with a proprietary empirical expression (given in Equation 4.11) is used. In that publication, all recombination is assumed to be associated with the n=1 ideality factor. Agreement is noted with the radiative efficiency method at high concentrations, consistent with the logic that high current densities lead to dominance by the n=1 component in the recombination current.

$$J_0 = e^{-40.5E_g+20.8538} \tag{4.11}$$

All findings show a similar trend to calculations performed at the detailed balance limit by Marti and Araujo [177], in that optimal band gaps decrease with greater concentration. It has been additionally shown that for low concentration ratios, lower material quality will increase optimal band gap energies to compensate for the loss in voltage.

Constraints on the radiative efficiency are applied depending on the lattice mismatch caused by growth on materials with different lattice constants. Up to ∼500-Sun illumination, optimal band gaps for the triple-junction solar cell are found to be higher than the case where radiative efficiency is the same throughout all junctions. Beyond this point, the radiative component of recombination becomes dominant and no significant differences are present. This is reassuring from both a cell-design and module viewpoint - assuming a sufficiently high concentration, the optimal band gaps will not change significantly under a reference spectrum.

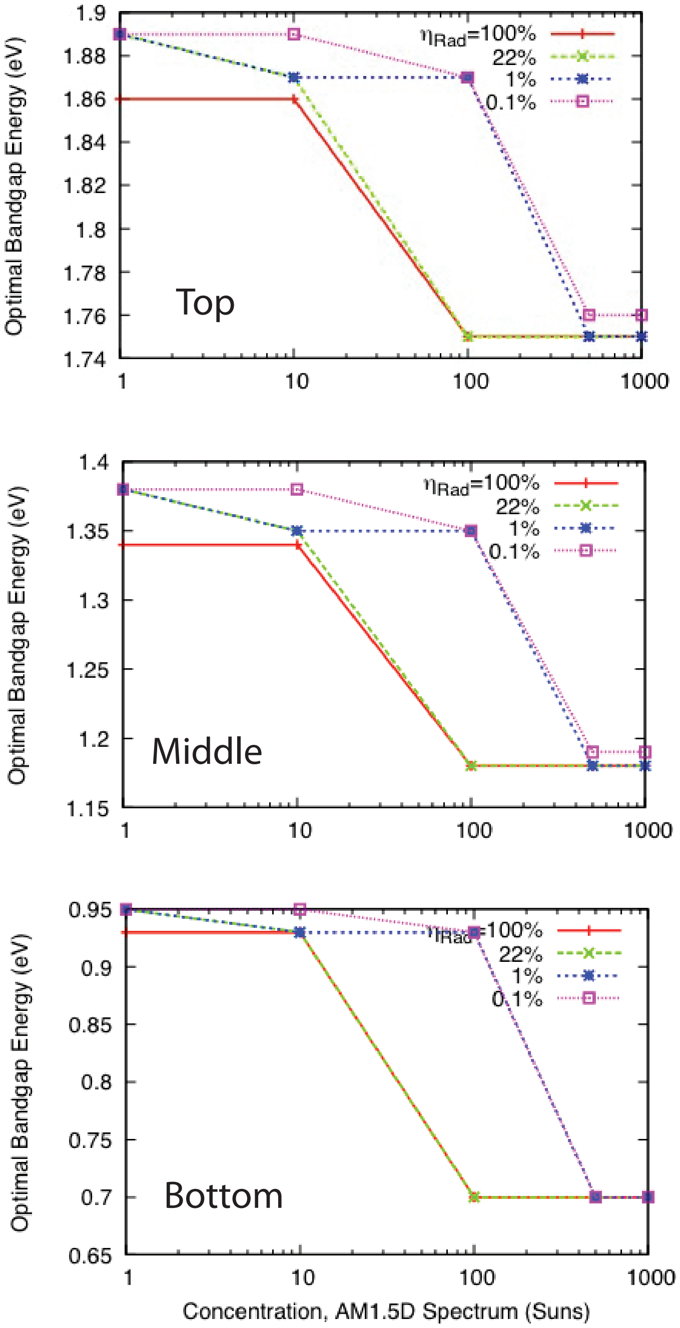

Figure 4.12: Optimal band gaps for a 3-junction device as a function of AM1.5D irradiance concentration under, showing (a) top, (b) middle, and (c) bottom junctions. Large jumps in energies are due to absorption bands in the terrestrial spectra. Optimal band gaps converge at high concentration.

Concentration	**Eg$_1$(eV)**	**Eg$_2$(eV)**	**Eg$_3$(eV)**	**Efficiency (%)**
1	1.85	1.34	0.67	36.51
500	1.75	1.18	0.67	51.79
1000	1.75	1.18	0.67	53.24

Table 4.4: Optimal junction band gaps for a **upright growth, Ge-substrate triple-junction device with InGaP/InGaAs/Ge junctions** as a function of radiative efficiency, under 1X, 500X and 1000X AM1.5D illumination.

Concentration	**Eg$_1$(eV)**	**Eg$_2$(eV)**	**Eg$_3$(eV)**	**Efficiency (%)**
1	1.90	1.42	0.99	36.99
500	1.90	1.42	0.99	49.79
1000	1.90	1.42	0.99	50.94

Table 4.5: Optimal junction band gaps for an **inverted growth, GaAs-substrate triple-junction device with InGaP/InGaAs/InGaAs junctions** as a function of radiative efficiency, under 1X, 500X and 1000X AM1.5D illumination.

4.6 Optimal Band Gaps - Constrained Material System Designs

It is understood that achieving good material quality, with as few defects as possible, is essential to creating a high performance multi junction solar cell. There are numerous growth methods that have been demonstrated with this in mind [76, 78, 194, 199].

Two of these are investigated - upright and inverted growth - and optimal band gaps for upright InGaP/InGaAs/Ge and inverted metamorphic InGaP/InGaAs/InGaAs solar cells are calculated. The 2013 exponential fit detailed in Figure 4.4 is used to calculate the radiative efficiency of junctions as a function of lattice mismatch.

For the upright growth on Ge, optimum band gaps of 1.75/1.18/0.67eV at 1000-Suns have been identified, given the assumption of 98% absorption above band gap and the estimated radiative efficiency values, with no parasitic resistance. This estimate bears resemblance to values highlighted

Concentration	**Eg$_1$(eV)**	**Eg$_2$(eV)**	**Eg$_3$(eV)**	**Efficiency (%)**
1	1.88	1.38	0.95	37.12
500	1.86	1.34	0.93	51.26
1000	1.86	1.34	0.93	52.59

Table 4.6: Optimal junction band gaps for a **upright growth, GaAs-substrate triple-junction device with InGaP/InGaAs/InGaAs junctions** as a function of radiative efficiency, under 1-, 500- and 1000-sun AM1.5D illumination.

Concentration	**Eg$_1$(eV)**	**Eg$_2$(eV)**	**Eg$_3$(eV)**	**Efficiency (%)**
1	1.87	1.36	0.94	40.63
500	1.74	1.17	0.69	53.46
1000	1.74	1.17	0.69	54.64

Table 4.7: Optimal junction band gaps for a **upright growth, Ge-substrate triple-junction device with lattice-matched junctions** at η_{Rad}=40%, under 1-, 500- and 1000-sun AM1.5D illumination. This can be considered the practical limit for triple-junction solar cells, given current achievable radiative efficiencies.

in other publications by King et al. [77] (1.80/1.30/0.67eV) and Guter et al. [76] (1.80/1.29/0.66eV), with the primary differences expected to be the near-unity absorption modelled.

Modelling the inverted growth on GaAs, the calculated estimate of optimal band gap is found to be identical to that proposed and experimentally demonstrated by Takamoto et al. [78], confirming the accuracy of this approach. For additional information, a calculation is performed to determine the optimal band gaps and efficiencies of an upright metamorphic InGaP/InGaAs/InGaAs device grown on a GaAs substrate, to highlight the effect of growth direction on optimal band gap. The projected efficiencies of these growth methods are shown in Figure 4.13.

It is worth noting that it is difficult for triple-junction solar cells based on inverted growth to achieve efficiencies above 50%, even under high concentration and negligible series resistance. Upright metamorphic devices can theoretically achieve slightly greater efficiency than inverted metamorphic

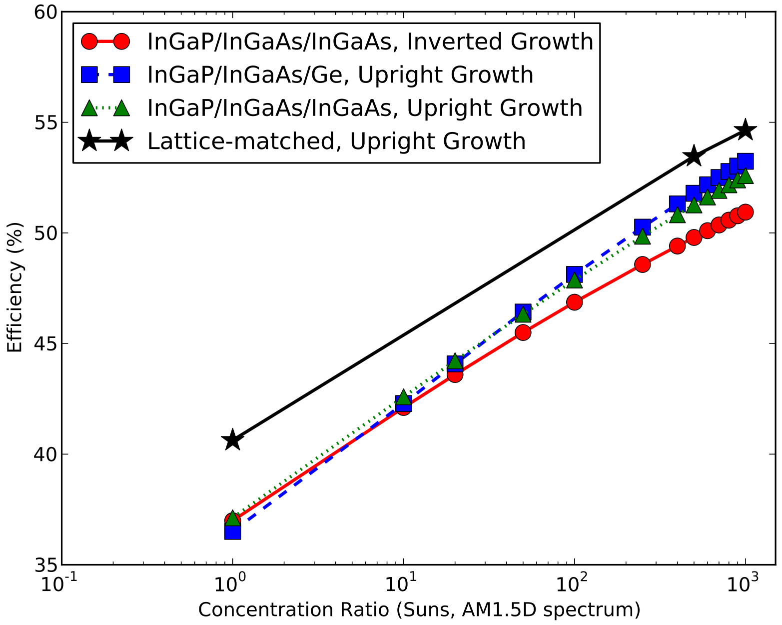

Figure 4.13: Efficiency of material-system constrained triple-junction devices as a function of concentration. Upright metamorphic devices can theoretically achieve slightly greater efficiency than inverted metamorphic MJSCs, but a fully lattice-matched triple-junction MJSC would offer an advantage of 3.5% and 1.4% absolute efficiency percentage points at 1X and 1000X AM1.5D compared with the next best performer, respectively.

MJSCs, but a fully lattice-matched triple-junction MJSC would offer an advantage of 3.5% and 1.4% absolute efficiency percentage points under 1X and 1000X AM1.5D illumination compared with the next best performer, respectively. This type of cell can be considered the practical limit for triple-junction devices, given current achievable radiative efficiencies.

4.7 Optimal Band Gaps - Further Considerations

Having considered the impact of material quality on diode performance, via the radiative efficiency figure of merit, it is necessary to consider factors that may have an effect on the optimal band gaps given in this paper. Idealized quantum efficiencies of 98% above band gap have been used this is achievable for a few anti-reflection coated materials, but serves as an upper limit in the analysis. Short-circuit current densities for devices have been known to change with increasing electron and proton fluence, alongside a reduction in radiative efficiency, but the effect will be complex and requires further investigation.

Calculations have been performed at a temperature of 300 K, but it is likely that both terrestrial and extraterrestrial devices will operate at a range of temperatures that deviate from this value. Optical efficiency has been maintained at unity over all wavelengths. This is known to be dependent on the material used in the optical system, with unique spectral dependence.

In addition, in this study, only two spectra have been studied the AM0 and AM1.5D Low-AOD reference spectra. For terrestrial concentrator systems in particular, realistic atmospheric conditions will affect the spectral distribution and thus the optimal band gap energies, themes that are explored in Chapters 5 and 6.

4.8 Summary

Optimal band gaps for modelled single-, dual- and triple- junction solar cells have been calculated whilst incorporating the effects of both radiative and non- radiative recombination, and have been found to be affected by material quality, characterised by the radiative efficiency.

At low solar irradiance concentrations, optimal band gap energies rise with increasing non-radiative recombination, by 100s of meVs. At high concentration ratios, the dominance of the radiative recombination mechanism regardless of the material quality results in no significant differences between optimal band gap energies. The observed behaviour is similar for both terrestrial and extraterrestrial spectra at concentrations ranging from 1X to 1000X.

When optimising solar cell band gaps under low concentration illumination, it is imperative that the material quality is accounted for. Complexity may arise where this factor is constrained by the availability of band gaps associated with each material system.

Good agreement is shown between predicted optimal band gaps for three material-system constrained triple-junction solar cells (inverted growth InGaP/InGaAs/InGaAs on GaAs substrate, upright growth InGaP/InGaAs/Ge on Ge substrate, upright growth InGaP/InGaAs/InGaAs on GaAs substrate) and experimentally demonstrated devices. The realistic efficiency limit of triple-junction solar cells with material quality currently achieveable have been established, and it is noted that new cell designs will likely be needed to realistically achieve conversion efficiencies >50%.

The results presented here provide a method by which solar cell designers can quantify material quality and incorporate it into their designs, and also provide a more accurate way of generating realistic, achievable roadmaps for future multijunction solar cells.

5 Energy Yield Estimation Methods - Validation at Toyohashi, Japan

In addition to performance under controlled standardised test conditions, it is important that photovoltaic systems can perform well under realistic operating conditions, where the irradiance and other atmospheric parameters are highly variable, and their energy output can be predicted with sufficient accuracy for users and/or investors. This allows developers to install appropriate capacity to satisfy a given load, and allows for greater confidence in the financial returns of any photovoltaics project.

Current tools do not simulate cell behaviour from fundamental physical parameters, instead relying on fits to measured system power output data. In this section, an alternative method is presented, where a previously developed semiconductor physics model that calculates system response from basic parameters is combined with a radiative transfer code that provides accurate estimates of the direct normal irradiance, providing a flexible, translatable tool for the CPV industry.

The accurate prediction of energy yields for photovoltaic systems has been the subject of many publications, primarily examining single-junction, flat-plate technologies such as silicon and cadmium telluride. King [200] and De Soto [201] have presented 1-diode, 5-parameter (J_{SC}, V_{OC}, R_{series}, R_{Shunt}, J_0) models and comparison with measurements for various types of silicon solar cells. These concepts are implemented in a number of PV energy yield estimation tools [202–204].

III-V concentrator photovoltaic systems attain high efficiency through the use of series connected multijunction solar cells. As these solar cells absorb over distinct bands over the solar spectrum, they have a more complex response to real illumination conditions than silicon solar cells. Multijunction solar cells have become standard components in high efficiency concentrator solar systems and offer the potential for low-cost solar electricity generation [205]. These highly efficient CPV systems have a much stronger dependency on the spectral irradiance than conventional single-junction photovoltaic panels [206, 207].

Past efforts to understand system behaviour under realistic spectral irradiance conditions have taken approaches with varying emphasis on modelling and experimental measurements. Calculation of the potential energy yields for a number of ideal, theoretical multi-junction cell designs and selection of the optimal designs is achieved through modelling in [206, 208]. Atmospheric parameters such as air mass, turbidity and precipitable water (PW) are considered, and the efficiency and power response to changing parameter values are evaluated. Spectral fluctuations have been noted cause changes in energy yield of up to 20% for single-junction solar cells [206] and around 5-10% variation in efficiency when predicting outdoor performance of multijunction devices [209].

A detailed balance method for simulating solar cell performance [174, 210] has been combined with atmospheric modelling [211] and the merits of various bandgap combinations in terms of energy harvesting efficiency. Cloudless-sky atmospheric data was sourced from reputable measurements sites, albeit only monthly average values are used - this has been shown to have a non-trivial impact on energy yield predictions [212]. It is understood that the detailed balance approach represents the theoretical limit to performance, with practical cells and systems operating well below this limit.

Araki et al. have calculated that for a spectrally optimised Ge-based triple-junction III-V solar cell, the power loss caused by spectrum mismatch over an annual period compared with AM1.5D reference power is 3.5% for Nagoya, Japan [213], reinforcing the idea that spectral effects can have a substantial impact on system performance. A direct comparison of modelled and measured energy yields are offered in [148, 149], where the energy output of a CPV system sited in Nevada, USA is predicted using atmospheric parameters taken from a typical meteorological year (TMY) database. Agreement in energy production to within 2% is noted over 14 months of operation, although this is in a location with an atmosphere bearing close resemblance to the conditions of the AM1.5D reference spectrum.

In a separate publication, the spectral response of triple-junction solar cells from Boeing Spectrolab has been examined as a function of temperature [214], and a preliminary analysis of the annual energy output for cells sited in several representative locations. The results indicated a potential for increased performance if cells are optimised for higher air mass and temperature, although several key atmospheric parameters and the transmission function of CPV optical elements are not accounted for in that particular paper.

Verlinden and Lasich [215] quantified the responsivity of a triple-junction solar cell to air mass, aerosols, PW and temperature for a concentrator dish system sited at Hermannsburg, Australia. In their analysis, air mass had the largest impact on efficiency, followed by precipitable water and then aerosols. A method for predicting output for any given CPV system at any location is proposed, involving translational corrections for various parameters. Although this has not been verified in publication to the authors knowledge, it is expected to estimate module efficiency to within a relative accuracy of 10%.

An overview of additional models that aim to predict the power output of CPV systems is given by Müller et al. [216]. These are for the most part empirical formulae taking in that rely on fitting parameters generated through collection of measured system performance data, and are very much system and location specific. A discussion of relevant energy yield prediction models is given in Section 5.1

In contrast to the approaches reviewed, the methodology discussed in this thesis predicts the energy yield of CPV systems from fundamental semiconductor device parameters and physical relationships. Time-resolved measurements of atmospheric parameters - including aerosols, relative humidity, temperature and solar irradiance - have been combined with simulations of the solar spectrum with a high temporal resolution. A detailed electrical modelling of a real CPV module, incorporating quantum efficiencies, optical transmission functions and parasitic resistances, allows the electrical output of different modules to be simulated for different atmospheric conditions. Coupled with on-site measurements of solar irradiance, temperature and relative humidity, this formed a detailed dataset estimating the annual energy yield and quantifying the impact of each parameter on module efficiency.

5.1 Review of published energy yield prediction models

Multijunction solar cells have become standard components in high efficiency concentrator photovoltaic (CPV) systems, and the performance of such systems is rated under a reference solar spectrum [217] and standardized ambient environmental conditions, allowing for ease of comparison between modules of different sizes and system designs.

Under realistic operating conditions, however, system performance deviates from reference values in a complex manner. Here, attempts by other authors to estimate energy yields in various systems are reviewed and key differences are summarised.

5.1.1 Sandia System Advisor Model

The Sandia System Advisor Model [218, 219] is a PV performance model with the ability to simulate CPV systems, using the relationship given in Equation 5.1:

$$P = DNI \times Area_{Collector} \times \eta_{Module}(DNI) \times F_{Temperature} \tag{5.1}$$

Where $\eta_{Module}(DNI)$ is the module efficiency as a function of DNI, $F_{Temperature}$ is a temperature correction factor, either provided in the manufacturers specifications or using suggested values from the built-in database. The calculation for $F_{Temperature}$ is given in Equations 5.2 and 5.3:

$$T_{Cell} = T_{Back} + dT\left(\frac{DNI}{DNI_{Ref}}\right) \tag{5.2}$$

$$F_{Temperature} = 1 + \gamma(T_{Cell} - T_{Ref}) \tag{5.3}$$

where DNI_{Ref} denotes the DNI under reference conditions, T_{Back} the temperature measured at the back of the module, γ the maximum power temperature coefficient, and dT is given as 17^0C.

This method requires the module efficiencies to be known under a range of irradiances, requiring a number of measurements to made on a manufactured system. In addition, there is no explicit accounting for spectral variations.

5.1.2 Translational methods

Translational methods begin with the system characteristics measured under reference conditions. The current-voltage curve, direct normal irradiance and module temperature are all measured with appropriate instrumentation. Each point of the curve can then be translated to a different irradiance level.

Because only a single reference I-V curve is required, this particular translational method can be used in a predictive manner, where a module does not need to be deployed on-site at a new site before the energy yield can be estimated.

For example, in [220, 221], the measured values are fed into a set of equations that translate realistic performance into defined standard test conditions, using an adapted form of the Shockley equations, as detailed in Equation 5.4 and 5.5.

$$I_{Measured} = I_{STC}\frac{DNI_{Measured}}{DNI_{STC}} \tag{5.4}$$

$$\begin{aligned} V_{Measured} &= V_{STC} - \Big[\Big(N \times \tfrac{0.0257\times(T_{STC}-T_{Cell,Measured})}{297}\Big) \\ &\quad \times \ln\Big(\tfrac{(I_{SC1,STC}-I_{Measured})\times(I_{SC2,STC}-I_{Measured})\times(I_{SC3,STC}-I_{Measured})}{I_{SC1,STC}\times I_{SC2,STC}\times I_{SC3,STC}}\Big)\Big] \\ &\quad - (N(E_{g1}+E_{g2}+E_{g3}) - V_{OC,Measured})\Big(1-\tfrac{T_{STC}}{T_{Cell,Measured}}\Big) \end{aligned} \tag{5.5}$$

where N is the number of cells in series, I represents the current, $\mathrm{V}_{Measured}$ the voltage of the measurement, $\mathrm{I}_{SCx,STC}$ represents the short circuit current for junction x under STC conditions, and all other symbols have their usual meanings. The power output at all biases is then simply the product of $I_{Measured}$ and $\mathrm{V}_{Measured}$.

Agreement to within 1.91% in instantaneous power output was noted for this method when tested on two concentrator modules at Puertollano, Spain. The DNI values of these test points were consistently high (>770 Wm^{-2}), indicating a careful selection process. In the field, CPV systems are expected to experience a wide range of atmospheric conditions, and the energy yield over a long time period must be evaluated to prove the success of any estimation method.

The methodology described here does not consider changes in the spectral distribution - it assumes that performance can be well characterised by variations in the DNI and temperature alone. Although this approach may well be applicable at the Puertollano site, where such assumptions may be acceptable due to the atmospheric conditions present, it may not be suitable to extrapolate this behaviour out to other deployment locations.

5.1.3 Multivariate regression methods

The multivariate regression methodology uses measured values for irradiance, air mass, precipitable water and temperature to generate an empirical relationship between these parameters and the instantaneous power. A key requirement is that the system needs to be deployed at the site of interest and the power output recorded over a sufficiently long time period, covering a range of atmospheric conditions. It also assumes the system undergoes no changes in its characteristics - for example, degradation will not be accounted for.

With a sufficiently large number of measurements, a multivariate linear regression analysis can be performed for each parameters and individual coefficients determined.

Two examples are given for empirical relationships in Equation 5.6, taken from the ASTM E 2527-06 standards:

$$P = DNI \left(a_1 + a2DNI + a_3 T_{ambient} + a_4 V \right) \tag{5.6}$$

where direct normal irradiance (DNI) represents the amount of sunlight incident on the system, $T_{ambient}$ represents the ambient temperature, V represents wind speed. It is important to note that coefficients for these relationships (a_1, a_2) are found by performing regression analysis on measured system data, requiring the establishment of test sites and a sufficiently long observation period. Such an approach does not consider aerosol explicitly, and the coefficients for one location may not be applicable to others. Hence by its nature, multivariate regression is a retrodictive (as opposed to predictive) method. For such numerically intensive technique, if a sufficient number of measurements are present and there are a large enough number of parameters in the empirical relationship, good agreement with measured power and energy yields can be expected for a specific location.

5.1.4 Typical Meteorological Year

A continuous effort from the National Renewable Energy Laboratory has resulted in Typical Meteorological Year (TMY) irradiance tables suitable for use in CPV performance prediction [222]. The latest update, TMY3, contains integrated DNI values at hourly resolution for over 1000 sites across the United States. The tables were created to represent the irradiance behaviour during a *typical* year at a certain location, accounting for humidity, aerosol optical depth and other meteorological parameters where measurements are available.

TMY data has been used in a number of CPV performance estimation calculations, with agreement to within 2% of measured energy yield in 9 months of operation [149]. Available data, however, is currently restricted to sites in the United States. In publications to date, the parts of the model that simulate the electrical performance of the module are proprietary and details are not released.

5.1.5 Utilization Factor methods

The concept of a utilization factor is a de-rating method that contains elements of the multivariate regression method [150, 223]. The standard one-diode model is used to calculate the performance under reference conditions, with the Utilization Factor (UF) invoked to extrapolate its performance under different air mass, temperature and DNI values. An example of this approach is give in Equation 5.7, along with the subfunction UF_{AM} in Equation 5.8.

$$UF = UF_{AM} + UF_T + UF_{DNI} \tag{5.7}$$

$$\begin{aligned} UF_{AM} & \qquad \mathbf{ForAM < AM_{Threshold}} \\ &= w_{AM}(1 + (AM - AM_{Threshold})) \times S_1 \\ & \qquad \mathbf{ForAM > AM_{Threshold}} \\ &= w_{AM}(1 + (AM - AM_{Threshold})) \times S_2 \end{aligned} \tag{5.8}$$

where UF_{AM}, UF_T, UF_{DNI} represent the utilization factor subfunctions for air mass, temperature and direct normal irradiance respectively. The coefficients w and S and the threshold value $AM_{Threshold}$ are determined empirically from collection of many measurements.

Published results show this has good agreement in terms of energy production to within 1.9% in some locations, but the show large inaccuracies performance in more challenging atmospheric conditions [223].

5.2 System Description and Atmospheric Data - Toyohashi, Japan

A concentrator photovoltaic module was sited at Toyohashi, Japan to investigate its performance under realistic operating conditions, with the current-voltage characteristics, maximum power and energy output recorded every

5 minutes from 2004-06-01 to 2005-05-31.

5.2.1 System Technical Parameters

The concentrator solar collector in this study is shown in schematic form in Figure 5.1. It is composed of 20 triple junction InGaP/$In_{0.01}$GaAs/Ge solar cells connected in series, illuminated by 550X solar concentration via a shaped Fresnel lens. A glass homogenizer is used to ensure a uni- form solar flux, with an optical efficiency of 85.8% [224]. The cells achieved efficiencies of 38.9% under 489 suns and Standard Test Conditions (STC). Quantum efficiencies for the cell are presented in Figure 5.2. The current-voltage characteristics can be calculated by analytically solving drift-diffusion equations defined in [57], given experimentally measured material parameters for each junction. Under reference conditions, the cell overproduces current in the Ge bottom junction. Further details regarding the precise construction process, reliability and cost of the module can be found in [90]. The module was mounted on a tracker, tracking the position of the sun throughout the day.

Peak system efficiencies of over 26% were measured for the concentrator system at a test-site located at Toyohashi University in Japan [225], where the system and atmospheric conditions are monitored continuously. The module power output and direct normal irradiance for the concentrator system in Toyohashi are shown for September 2004 and March 2005 in Figure 5.3. DNI was measured using an Eko Instruments MS-54 pyrheliometer mounted on the module to measure the direct normal irradiance incident on the module. In addition, a separate ground mounted tracking pyrheliometer of the same model was deployed adjacent to the module. The characteristics of that device are given in Table 5.1.

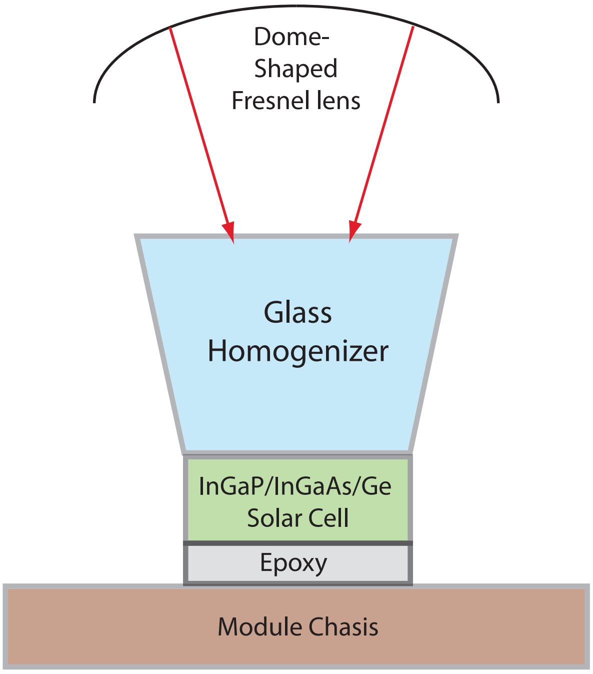

Figure 5.1: Schematic diagram of a single receiver in deployed InGaP/InGaAs/Ge CPV module in Toyohashi, Japan.

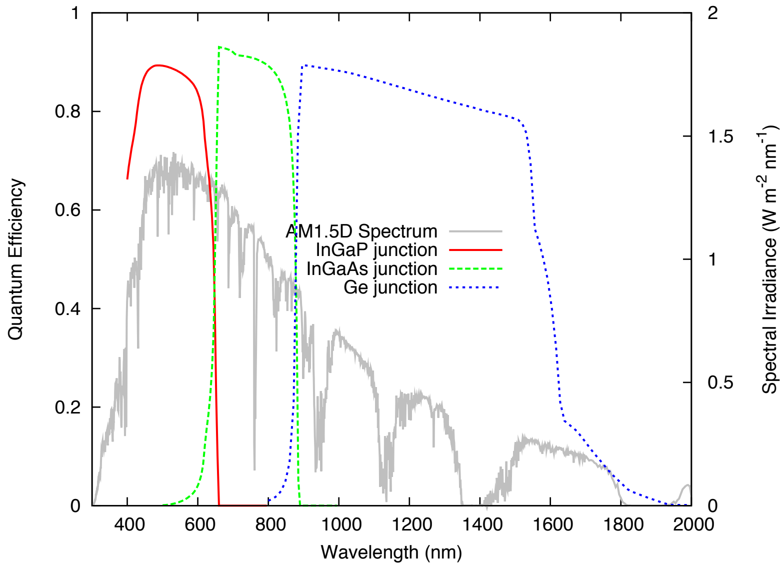

Figure 5.2: Modelled quantum efficiencies for the lattice-matched InGaP/InGaAs/Ge cells used in the modules at Toyohashi, Japan. AM1.5D reference spectrum also shown.

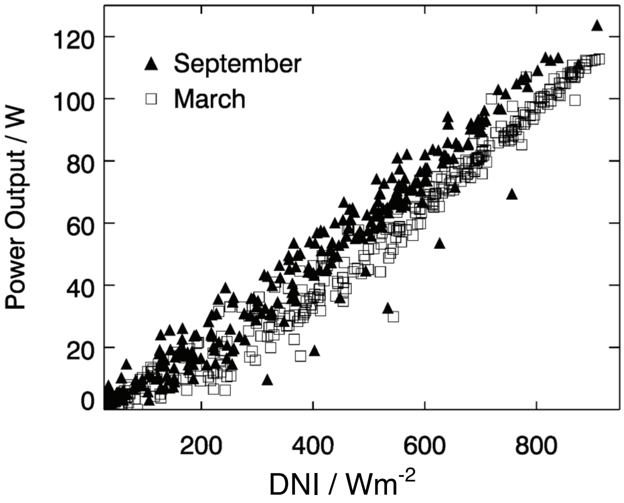

Figure 5.3: Electrical power output of concentrator photovoltaic module versus measured direct normal irradiance for the months of September 2004 and March 2005.

Parameter	**Value and Applicable Range**
Spectral range	200 - 4000nm
Spectral selectivity	Less than ±0.5% (350 - 1500 nm)
Non-linearity	Less than ±0.2% (<1000 nm)
Irradiance range	0 - 2000W m^{-2}

Table 5.1: Technical specifications for the Eko Instruments MS-54 pyrheliometer used to make measurements of direct normal irradiance incident on the Toyohashi module.

5.2.2 Atmospheric Data

Air mass values were calculated internally by SMARTS 2.9.5 , using the fomulae detailed in Section 2.1 and the date and time information recorded.

On-site aerosol measurements were not available at Toyohashi, and it was necessary to use data from AERONET [166] sites at Shirahama and Osaka, situated 140 and 105miles from Toyohashi, respectively. To assess the spatial and temporal variability in aerosol loading, the correlation of aerosol optical depth between the two locations have been examined. Figure 5.4 shows a scatter plot of daily mean AOD_{500} from the two sites, requiring at least three measurements to be made in the same day. The clear positive relationship, with a least-squares fit gradient of 0.95 and a Spearmans rank correlation coefficient of 0.74, would suggest that both sites show similar temporal variability in aerosol loading, with slightly higher values tending to be prevalent at Osaka.

Data is examined over a long time period (1st January 2000 to 1st January 2011) and a histogram of the differences in daily mean AOD between Osaka and Shirahama is computed. On average, Osaka's AOD values are 34% higher, providing an upper estimate for AOD.

The average of daily AOD_{500} at the two sites is used in the simulations as a rough approximation for the true aerosol conditions at Toyohashi. Although there is substantial geographical separation between the AERONET sites and Toyohashi, for a first attempt at quantifying the impact of differ-

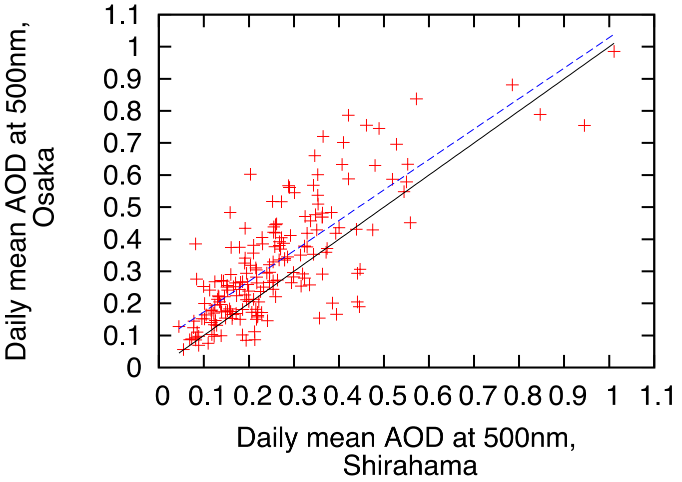

Figure 5.4: Correlation between measured daily mean aerosol optical depth at Osaka and Shirahama AERONET sites, June 2004May 2005. Dashed line represents a 1:1 relationship; dotted line is a least-squares fit to data points with a gradient of 0.95.

ent parameters, the method provides a reasonable estimate of AOD_{500} with the available data.

In this location, examination of the Angström Exponent suggests increased aerosol loading leads to considerable attenuation of short wavelength light. Figure 5.5 shows the daily mean AOD at Shirahama for the test period, from 1st June 2004 to 1st June 2005. On a day when AERONET measurements are unavailable, either due to equipment downtime or cloudy conditions over the AERONET sites, the AOD at Toyohashi is taken as the mean AOD of the 10 days either side. This ensures the seasonal behaviour is captured, without the noise of day-to-day variations.

On-site measurements of relative humidity and ambient temperature were made using an Eko Instruments MT-062 device, incorporating both a thermometer and a hygrometer into a single unit, with the specifications given in Table 5.2.2 . These values have been used to calculate values of PW internally within SMARTS, using standard equations given in previous publications [226, 227].

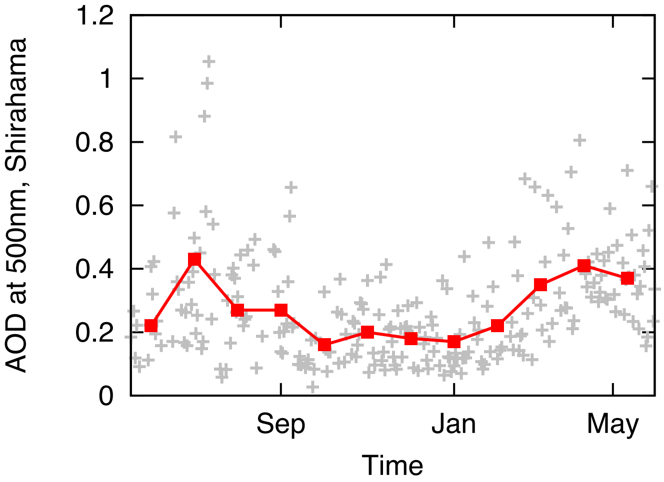

Figure 5.5: Daily mean (grey crosses) and monthly mean (red squares) aerosol optical depth for the Shirahama AERONET site, June 2004May 2005.

Parameter	**Value and Applicable Range**
Relative Humidity	
Humidity Range	0.8 - 100% RH
Measurement error	less than ±2% (0.8 - 90% RH)
	less than ±3% (90 - 100% RH)
Ambient Temperature	
Temperature Range	-40 to +60^{0}C
Measurement error	±0.3% (at 20^{0}C

Table 5.2: Technical specifications for the Eko Instruments MT-062 thermometer and hygrometer, measuring temperature and humidity respectively.

Precipitable water values derived from this method are broadly in agreement with AERONET measurements at Shirahama, and the correlation is shown graphically in Figure 5.6. A good linear fit is achieved between daily mean values at the two locations, with a least squares fit gradient of 1.01, and a Spearmans rank correlation coefficient of 0.89, indicating a strong positive relationship. By examining PW derived from humidity as a function of time, illustrated in Figure 5.7, one can note a clear seasonal dependence, with high PW in the summer months and low values during winter.

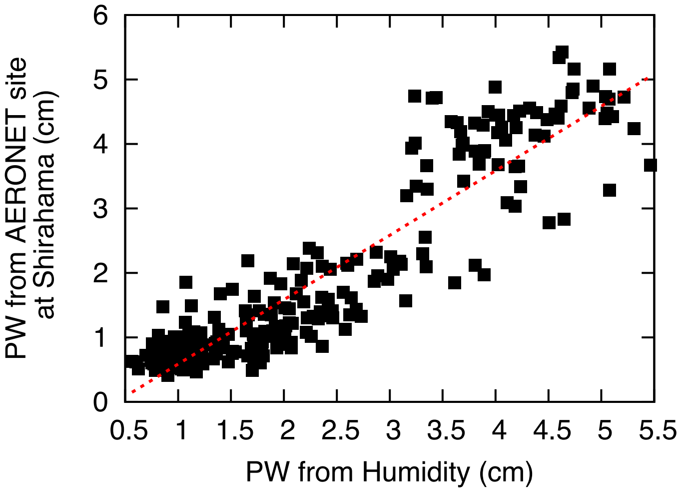

Figure 5.6: Correlation between measured precipitable water at the Shirahama AERONET site, and precipitable water derived from relative humidity measurements at Toyohashi. Dotted line is least-squares linear fit with a gradient of 1.01. A clear positive correlation is present.

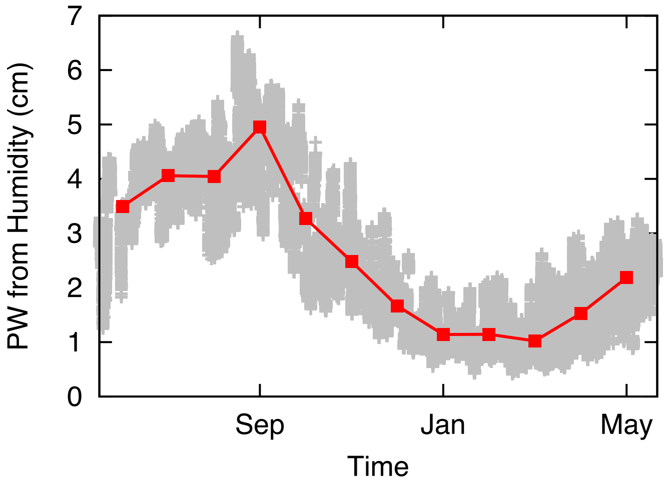

Figure 5.7: Daily mean (grey crosses) and monthly mean (red squares) precipitable water values derived from measurements of relative humidity for Toyohashi, June 2004 - May 2005.

5.3 The Syracuse Model

To accurately simulate the behaviour of both the atmosphere and concentrator module, a computer model called Syracuse [228,229] has been developed and consists of several components illustrated in Figure 5.8. The SMARTS 2.9.5 radiative transfer code [46] is used to give a realistic estimate of the spectral photon flux incident on the concentrator module drawing from a database of local meteorological parameters. A photovoltaic device model then determines the response of the solar cell to this incident irradiance, accounting for transmission through the concentrator optics. The device model considers photogeneration and recombination in each of the component junctions in the multi-junction solar cell. An equivalent circuit is then composed representing each junction, shown in Figure 5.9, and linked together to assemble a cell and module. Finally, the circuit network is solved, and the results are collected into a form in which they can be readily compared with outdoor test data.

The calculation of the photocurrent starts from the fundamental absorp-

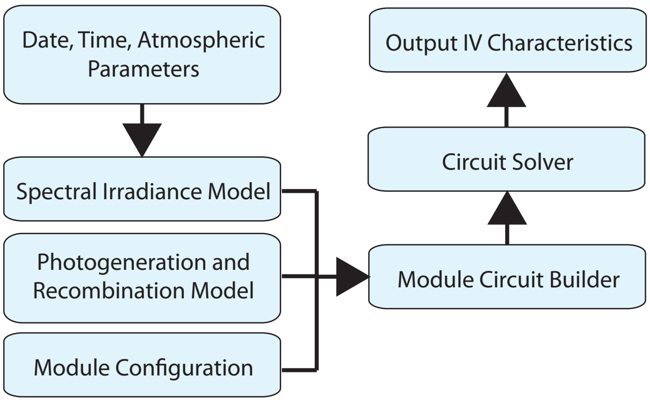

Figure 5.8: Components of the Syracuse computer program used to simulate module performance.

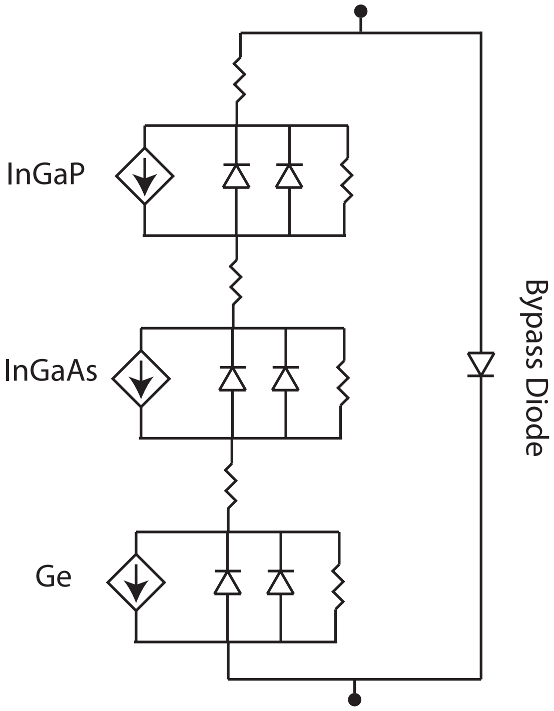

Figure 5.9: Equivalent circuit for a single multi-junction cell packaged with a bypass diode into a receiver.

tion coefficient for each semiconductor junction [230, 231] and offset according to the semi-empirical Varshni equation [232], $E_g(T) = E_0 - \frac{\alpha T^2}{T+\beta}$, to account for the temperature dependence of the band-gap and hence absorption profile. The quantum efficiency profile for each junction is then calculated from the absorption coefficient, junction thicknesses (x), minority carrier diffusion length (L) and surface recombination (S) using analytical solutions to the semiconductor diffusion equations in the neutral p and n regions of the device [57]. Photogeneration that takes place in the depletion region is assumed to be completely collected. Convolving the quantum efficiency curve with the appropriate spectral irradiance then yields a short circuit current for each junction, represented in Figure 5.9 by the current source.

Recombination in each junction is approximated using a double diode model, accounting for carrier injection in the neutral regions of the device (J01) and Shockley-Read-Hall recombination in the depletion region (J02) [57, 233, 234]. The tunnel junction is treated as a linear resistive element with a characteristic resistance. The values for J_{01} and J_{02} and parasitic resistances were determined from extensive experimental fitting to the I-V characteristics of the solar cells used in the module under controlled illumination and temperature conditions [235]. In all cases, the J_{02} component of the recombination current was found to scale with $e^{\frac{qV}{2kT}}$ whereas the J01 component was found to vary as $e^{\frac{qV}{n_1 kT}}$, where the ideality factor n_1 was close to unity. The values used in the simulation are given in Table 5.3, and the resultant quantum efficiencies are given in Figure 5.2. The radiative efficiency figure of merit has not been used here, due to the presence of good quality experimental data, but the calculated values of η_{rad} from J_{01} and J_{02} are on the order of $\approx$0.04%, far from the theoretical radiative limit for solar cells.

In a real module containing many series-connected solar cells, it is inevitable that small differences in optical alignment or cell manufacturing will exist. This mismatch loss manifests itself in a series-connected string of cells as a reduced fill factor and needs to be simulated if good agreement with module I-V curves is desired. To account for this, the short-circuit currents are distributed on a Gaussian curve of standard deviation s, with

Material Parameter	**Parameter Value**		
	InGaP	**InGaAs**	**Ge**
L_n	1×10^{-6}m	5×10^{-6}m	5×10^{-5}m
L_p	200×10^{-9}m	500×10^{-9}m	800×10^{-9}m
x_n	100×10^{-9}m	100×10^{-9}m	400×10^{-9}m
x_p	600×10^{-9}m	350×10^{-6}m	100×10^{-6}m
E_0	1.976eV	1.519eV	0.7437eV
α	7.5×10^{-4}	5.405×10^{-4}	4.774×10^{-4}
β	500	204	235
J_{01}	4.93×10^{-24} Acm^{-2}	1.0×10^{-21} Acm^{-2}	4.93×10^{-6} Acm^{-2}
n_1	1.07	1.05	1.00
J_{02}	3.28×10^{-15} Acm^{-2}	2.70×10^{-10} Acm^{-2}	1.00×10^{-5} Acm^{-2}
n_2	2.00	2.00	2.00
R_s	0.0236 Ω	0.0012 Ω	8.00×10^{-4} Ω
R_{sh}	3×10^{6} Ω	1.5×10^{6} Ω	115 Ω
S_n	1cm^{-1}	1cm^{-1}	1cm^{-1}
S_p	3.0×10^{3}cm^{-1}	1cm^{-1}	1cm^{-1}
N_A	1×10^{17}cm^{-3}	1×10^{17}cm^{-3}	1×10^{17}cm^{-3}
N_D	2×10^{18}cm^{-3}	3×10^{18}cm^{-3}	3×10^{18}cm^{-3}

Table 5.3: Parameters for simulating quantum efficiencies and module behaviour.

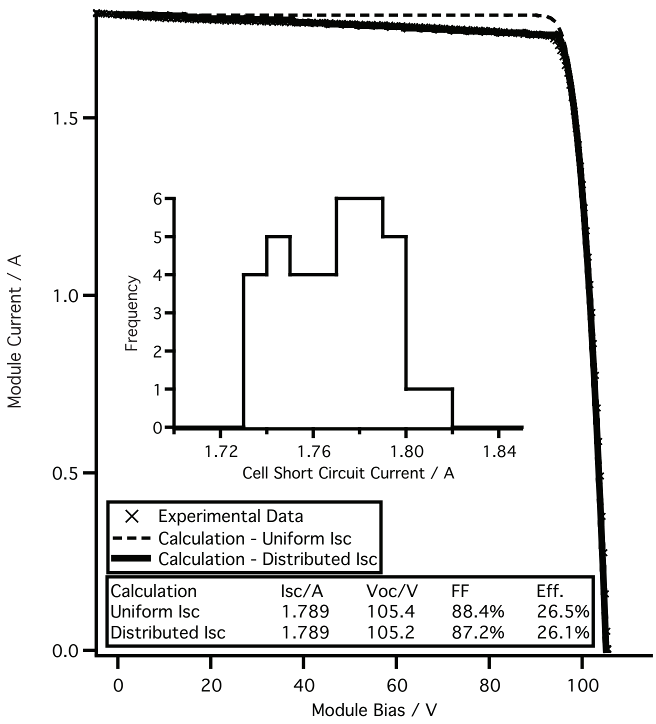

Figure 5.10: Simulated and experimentally measured I-V curve for a 400X module with 36 identical cells giving uniform Isc over the module and non-uniform cells with a distribution of I_{SC} across the module.

the highest current in this discrete set matching the detailed calculation of the short-circuit current described earlier. Figure 5.10 shows an I-V curve for a similar module taken on a clear, dry day with low aerosol loading. The assumption of identical, uniform cell response results in too high a fill factor, but distributing the cell current with $\sigma = 0.014$ gives a remarkably good fit as shown in the inset in Figure 5.10. Over the measurement period, the standard deviation of the distribution in cell current is observed to rise slightly, as might be expected owing to weathering of components over time.

A key advantage of the Syracuse modelling methodology is its translatability across different locations - as we're simulating from the most basic device and atmospheric parameters, there is no reliance on any empirical relationships as in regression-analysis based methods. All parameters used in Syracuse are linked to physical processes, whilst most empirical relationships use coefficients that do not have any physical meaning - they simply provide a weighting for the parameter in question. This is much more intuitive and offers us flexibility in two key ways:

- **Predictive power in new climates** - the performance of new system designs at locations with different atmospheric conditions can be estimated before manufacturing or deployment. Provided a good model of the cell and module is available and there are measurements of the atmospheric conditions, it is possible to predict the energy yield prior to deployment.
- **Enhanced cell design** - understanding atmospheric interactions and their effect on the spectrum will allow us to influence system design - to deal with current-limiting issues in more spectrally selective MJSCs.

5.4 Estimating Annual Energy Yield at Toyohashi

Using an entire year of meteorological data, including DNI, temperature, relative humidity and averaged daily AOD from the two AERONET sites, the concentrator system was simulated using the method detailed, every 5 min from 1 June 2004 and finishing on 1 June 2005, and the results were compared with the actual measured system data. In the best-effort simulations, the date and time information, ambient and module temperature, relative humidity and daily average aerosol optical depth were input as atmospheric parameters.

SMARTS is then triggered to generate a solar spectrum, based on these atmospheric parameters. The spectrum is then scaled to match the measured DNI from the database. The prediction of time-resolved DNI is difficult, particularly when cloudy conditions are considered, and it is understood that the real spectral distributions can deviate significantly from the simulated spectrum. This CPV system generates relatively little of its annual electrical power output during cloudy conditions.

This approach ensures the modelled solar irradiance incident on the module matches measured values, but accounts for the spectral distribution of the solar spectrum using SMARTS2. The aerosol profile SRA Urban has been chosen for this work.

The Syracuse computer programme, using appropriate quantum efficiencies, parasitic resistances and recombination parameters, would then simulate the electrical characteristics. Simulated instantaneous current-voltage characteristics of the module are then output, from which electrical power, efficiency and annual energy yield can be derived.

Accounting for all measurable atmospheric parameters leads to an agreement between the simulated and measured annual energy yield of 2.1%, as shown in Table 5.4. From 1 June 2004 to 31 May 2005, a total DNI of 1265.41 kWh m^{-2} is recorded as having been incident on the module.

To investigate the effect of spectral distribution on energy yield, a simulation was performed where the spectral distribution of the fixed AM1.5D low-AOD spectrum [217] of each simulation point remains fixed, but scaled to match the DNI measured value. This leads to an overestimate of 16% in the annual energy yield. If instead, the old AM1.5D reference spectrum [236] is used, but also scaled to match measured DNI, an over-estimate of the annual energy production by 5% is obtained.

This is clearly seen in Figure 5.11, which compares the measured efficiency with that simulated using the best approach and with the standard AM1.5D low-AOD spectrum. The seasonality noted in the measured efficiency is clearly not present when the fixed reference spectrum is used; strong evidence that the spectral distribution of the solar spectrum plays a large role in determining system performance.

Although the seasonality of the module efficiency is captured in the Syracuse simulation, it is necessary to consider the deviations throughout the year. The calculation of air mass is dependent on solar geometry and is well understood [46, 237], but the aerosol loading and size distribution is likely to vary between Toyohashi and Osaka or Shirahama. To demonstrate this, the difference in AOD between Shirahama and Osaka is plotted in Figure 5.12. This atmospheric parameter is believed to be primarily responsible for

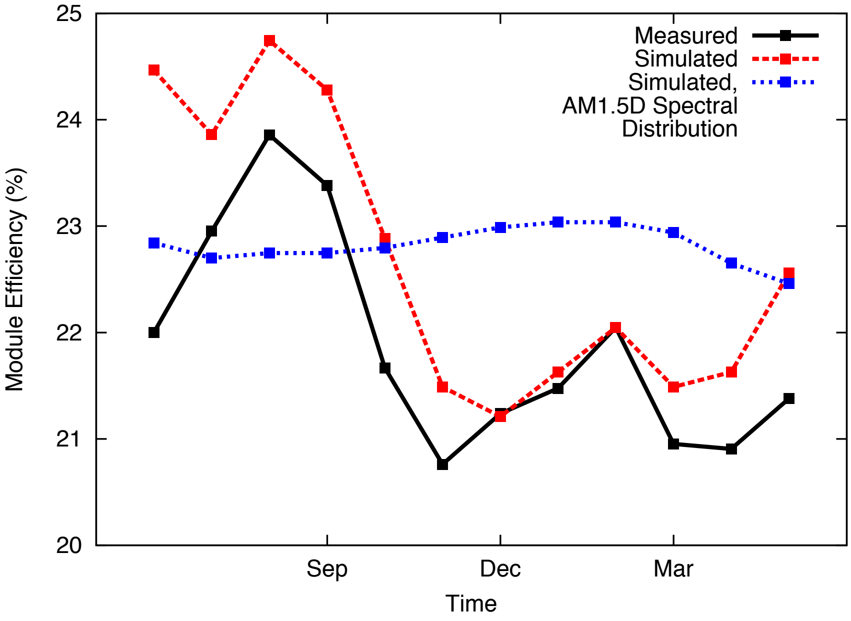

Figure 5.11: Measured and simulated module efficiencies. Best effort simulation (dashed line) shows good general agreement and captures seasonal variation. Simulated efficiency if the spectral distribution associated with the AM1.5D low-AOD spectrum is scaled to match direct normal irradiance is shown - the dependence of module efficiency on seasonal effects is no longer present.

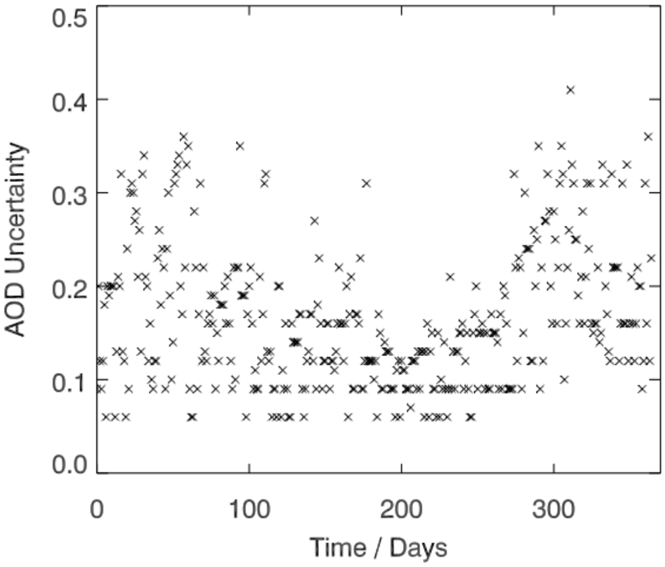

Figure 5.12: Difference in aerosol optical depth extracted from AERONET data between Shirahama and Osaka, June 2004 - May 2005.

differences between measured and modelled module efficiencies throughout the investigated time span.

In addition, the methodology contained in SMARTS for estimating PW from relative humidity [226, 227] has been validated in North America only, although the experience is expected to be translatable to Japan. It is also possible that the variation in PW causes a smaller change in module efficiency.

The deviation in module efficiency of 2.5% in June 2004 likely results from a combination of these two effectsthe variability in AOD between Osaka and Shirahama is high during that period, and Figure 5.16 indicates such variability in AOD would result in module efficiency deviations of approximately 2%. The remaining deviations are likely attributable to PW and inhomogeneous cell temperature across the module.

A summary of the agreement between measured and simulated energy yields is presented in Table IV. These results highlight the need to understand the local atmospheric conditions and their variation over long time scales, rather than relying on standard reference spectra, if accurate estimates of energy yield are to be made in diverse locations.

Particularly good agreement between the simulated and measured power output was achieved during periods of high DNI. When DNI drops below $\approx 400\ Wm^{-2}$, the simulation has a tendency to overestimate the power delivered, highlighted in the frequency contour of measured and modelled electrical power output as a function of DNI given in Figure 5.14. This stems from an inability to fit the fill factor correctly at low irradiance. Because the fill factor is affected by illumination and temperature uniformity across the module as well as spectral irradiance, a combination of these effects is likely to be responsible.

The parasitic resistances in the cell and module do not appear play a significant role in the deviation between measured and simulated fill factor. Such an effect would lead to significant drop in fill factor under high DNI conditions caused by enhanced currents. A contour histogram of measured fill factor against DNI is shown in Figure 5.13, demonstrating a greater variation in fill factor at low irradiances, in line with our hypothesis. A Spearmans rank coefficient of +0.379 confirms a positive statistical correlation.

Although the complex behaviour in this regime remains a topic of investigation, it is important to emphasise that a reduced accuracy during periods of low DNI does not adversely affect the overall energy yield calculation because the majority of the power is delivered during periods of high DNI where the simulation is accurate. It must be noted that investigations from Chapter 3 show that SMARTS performs with reasonable accuracy above $400\mathrm{Wm}^{-2}$, within pyrheliometer instrument error.

Owing to Japans location in the Northern hemisphere, one would expect lower air mass values during the summer months, and enhanced DNI as a result. The recorded measurements do not follow this pattern, and instead show greater DNI during winter months, when air mass is higher, even when cloud cover is discounted as much as possible. This is likely due to higher

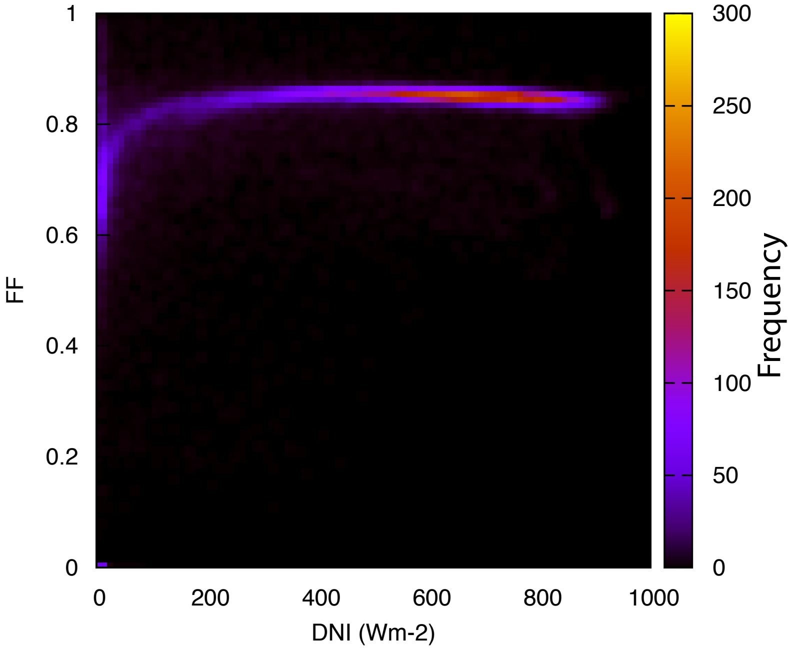

Figure 5.13: Frequency colour contour of measured fill factor versus direct normal irradiance. Greater variation in can be noted at low irradiances.

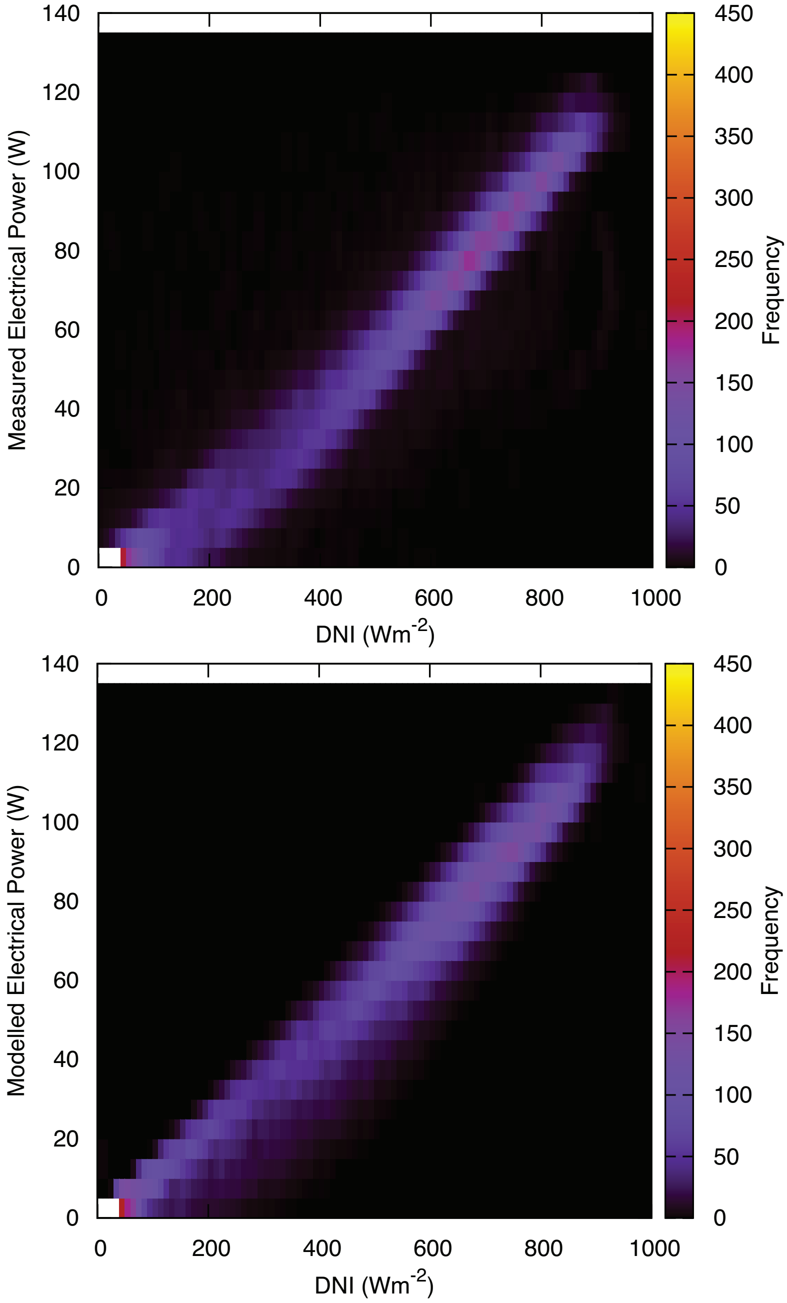

Figure 5.14: Frequency colour contour of measured and modelled module electrical power versus direct normal irradiance. The model overestimates power at low irradiances compared to measured values.

aerosol loading and greater PW during the summer months, increasing absorption and scattering, and hence reducing DNI.

In addition, module efficiency reaches a peak during the summer months, despite the lower DNI. Module efficiency is expected to rise as air mass decreases, but this should be coupled with an increase in DNI. In the data available, aerosol is enhanced over the summer months, but the detrimental effect of that parameter on efficiency is outweighed by the positive effect of higher PW. Such complexity in atmospheric parameters should be accounted for in accurate simulation programmes.

Simulation Description	**Electrical Yield (kWh)**	**Deviation from Measured Data**
Measured Module Output	121.3	-
Syracuse Simulation, Full atmospheric data, 5-min interval using SMARTS	123.8	+2.1%
Spectral distribution of High-AOD AM1.5D reference spectrum, ASTM E-891 (Old Standard)	127.3	+4.9%
Spectral distribution of Low-AOD AM1.5D reference spectrum, ASTM G173-03 (New Standard)	141.0	+16.2%

Table 5.4: Annual electrical energy yield for measured and modelled outputs, and the percentage deviation in annual energy yield from measured data. Neglect of atmospheric parameters that shows an over-estimate of up to 16% can be introduced. Good agreement within 2% of measured annual yield is noted for simulations incorporating best-effort atmospheric parameters.

Parameter	**Data Source**	**Observed** Range	**Impact on Efficiency (Absolute % points)**
Air mass	Date, Time, Location	1.02 - 70.65	20
Aerosol Optical Depth, 500nm	AERONET data, interpolated	0.027 - 1.054	10
Precipitable water	Local air temperature, relative humidity	0.41 - 6.61	3
Cell temperature	Estimated from measured module temperature, DNI	273 - 350K	1.5
Current mismatch between receivers	Estimated from fill factor	1.0 - 2.5%	0.7
Others	-	-	<2

Table 5.5: Impact of atmospheric parameters on module efficiency at Toyohashi, Japan.

5.5 Influence of Atmospheric Parameters on Module Efficiency at Toyohashi

The impact of various atmospheric parameters on module efficiency has been investigated, by examining the difference in module efficiencies associated with the extreme values of each parameter. A single parameter is varied, whereas all others are held constant at values regarded as typical, allowing for the effect of individual variables to be examined. A summary detailing the parameters examined, their impact on module efficiency and observed ranges used in this paper is presented in Table 5.5, and the authors are well aware that the range of values for each parameter will vary according to location. It must be stresed, however, that the stated values are suitable ranges for the Toyohashi location.

The three most significant factors that influence the efficiency of this triple junction concentrator system were found to be air mass, AOD and PW. As air mass depends on the solar position, it can be calculated with high accuracy, but meteorological data for the other parameters is essential, particularly for the summer months, when both PW and AOD are higher.

5.5.1 Influence of Air Mass

For Toyohashi, Japan with this module, air mass has the largest impact on system efficiency of 20%, as expected. At high air mass, short wavelength light is strongly attenuated, and the cell becomes badly current mismatched resulting in a dramatic drop in module efficiency. Such behaviour is illustrated in Figure 5.15.

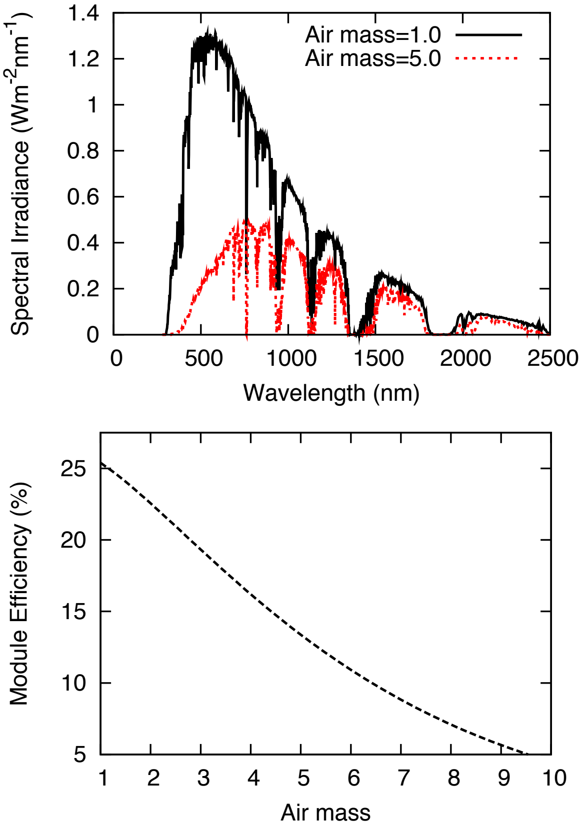

Figure 5.15: Effect of air mass on (a) spectral irradiance and (b) module efficiency. Other parameters remain fixed, AOD = 0.28, cell temperature at 310 K, PW = 1.42 cm.

5.5.2 Influence of Aerosols

Aerosol optical depth is found to be the atmospheric parameter with the second largest impact on the efficiency of this module at 10%. The high

Angström exponent values in both the measurements and the selected aerosol model ensure that aerosols absorb and scatter preferentially at short wavelengths at this location.

As the InGaP/In$_{0.01}$GaAs/Ge solar cells are top junction current-limited under CSTC, increased AOD results in detrimental impact on module performance, illustrated in Figure 5.16, as the top junction is deprived of light.

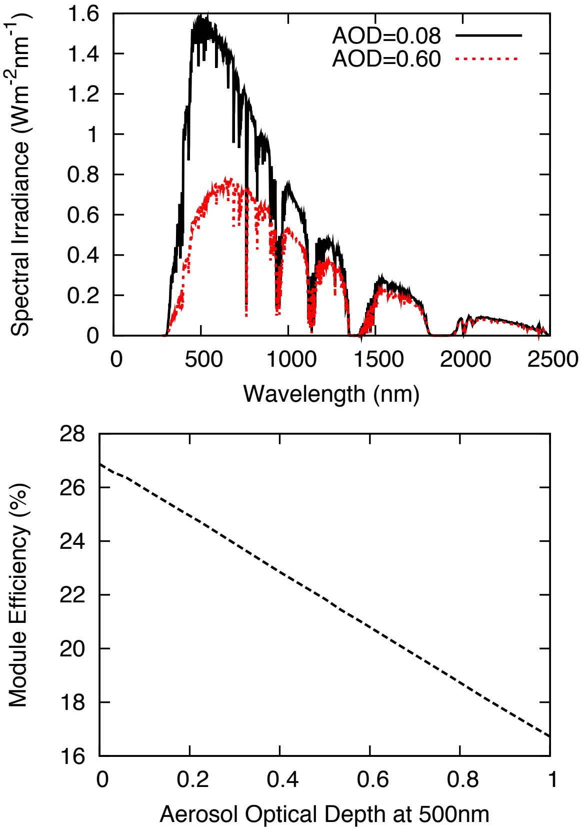

Figure 5.16: Effect of aerosol optical depth on (a) spectral irradiance and (b) module efficiency. Other parameters remain fixed, air mass = 1.5, cell temperature at 310 K, PW = 1.42 cm.

5.5.3 Influence of Precipitable Water

In Figure 5.17, sample PW values for summer (June September, 5.00) and winter (DecemberFebruary, 0.50) months were computed and the SMARTS2 radiative transfer model was used to simulate the impact on spectral irradiance. All other atmospheric variables were kept constant at representative values.

With increasing PW, the efficiency rises as the cell power output remains roughly constant, whereas the DNI is reduced. This is confirmed in Figure 5.17, showing the efficiency of the triple junction solar cell as a function of PW. As the multi-junction solar cell was always found to be current limited by the top InGaP junction and the variation in spectral irradiance with different values of PW is mainly seen in the infrared, it has relatively little effect on the solar cell power output. This behaviour is illustrated in Figure 5.18, showing first DNI and electrical power output as a function of PW, and the remaining fraction of DNI and electrical power from the values associated with PW=0.0cm. DNI is seen to drop off quicker than electrical power as a fraction of its initial value, leading to a rise in efficiency.

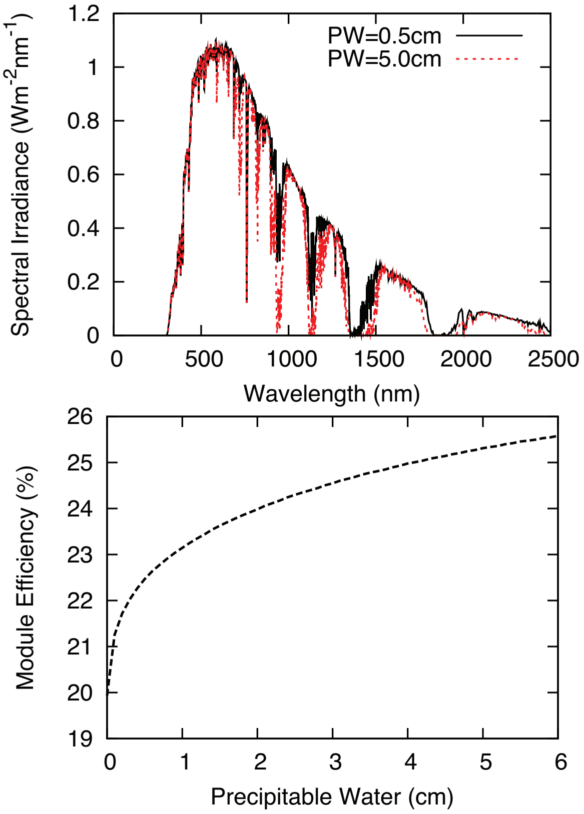

Figure 5.17: Effect of precipitable water on (a) spectral irradiance and (b) module efficiency. Other parameters remain fixed, air mass = 1.5, AOD = 0.28, Cell temperature at 310K

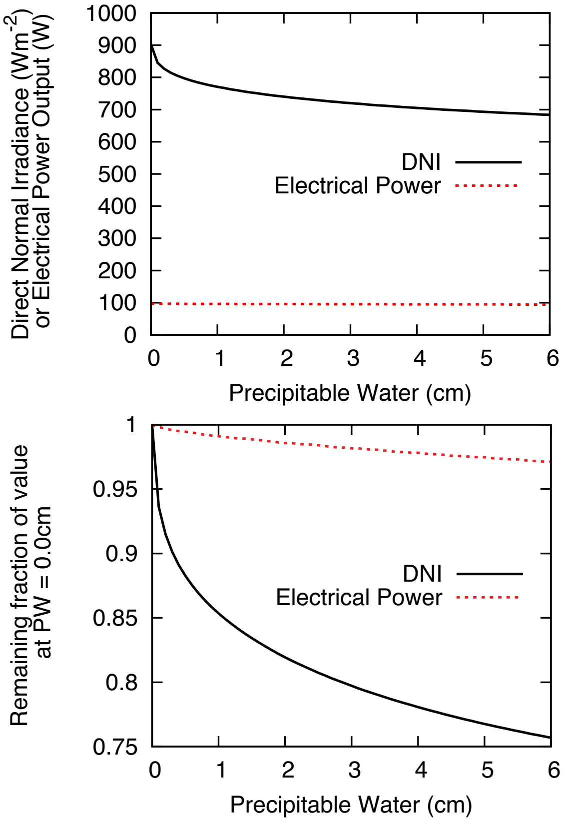

Figure 5.18: Effect of Precipitable water (PW) on (a) direct normal irradiance (DNI) and electrical power output and (b) remaining fraction of DNI and electrical power output values, compared with PW = 0.0 cm. Other parameters remained fixed, air mass = 1.5, AOD = 0.28, cell temperature at 310 K.

5.5.4 Influence of Other Parameters

The sensitivity of cell efficiency to other atmospheric parameters was also investigated, including ozone, the choice of aerosol models pertinent to the area, gas pollution models (both internal to SMARTS) and temperature. In this instance, AOD has been specified, with the aerosol model controlling the Angström exponent involved in the calculation. This parameter will impact on the calculated AOD at other wavelengths and change the spectral distribution of the solar spectrum. The impact on efficiency was small (0.7%

absolute) when other sensible choices of aerosol model were considered. No other parameters demonstrated a significant impact on system efficiency when appropriate bounds on the analysis were applied.

5.6 Summary and Recommendations

When sufficient meteorological data is available, it is possible to simulate multi-junction concentrator systems with high accuracy. Some long-term data, such as humidity and integrated DNI values may be readily available, but need to have knowledge of aerosol conditions is crucial if accurate predictions of energy yield are to be made. It has been demonstrated that energy yields can be predicted to within 2% accuracy using the Syracuse model, given sufficient atmospheric information, for a module located in Japan.

Air mass, aerosol optical depth and PW have been identified as atmospheric parameters with the largest impact on system efficiency at Toyohashi for this particular system. By developing an understanding of the fundamental physical principles, it is feasible that the modelling methodology is inherently transferable to other sites with different atmospheric conditions, providing sufficient atmospheric and material parameter information is available.

The work presented in this chapter provide a clear, open and translatable way for system developers, analysts and other interested parties to predict the energy yield for a given CPV system in new atmospheric conditions, without the need to establish test systems at the location of deployment, or rely on retrodictive models and past measurements. By providing a measurement of the impact of individual atmospheric parameters, the most useful monitoring apparatus can then be deployed, or the appropriate measurements can be sought from relevant parties.

6 Impact of individual atmospheric parameters on CPV system power, energy yield and cost of energy

Under realistic operating conditions, CPV system performance deviates from reference values in a complex manner. This chapter identifies and quantifies two critical issues when considering CPV performance - the impact of individual atmospheric parameters on the rated power, and the influence of atmospheric data knowledge on energy yields. Currently, there are methods that deal with spectral mismatch between subcells, but none that deal specifically with the impact of each atmospheric parameter, and none that deal with the impact on power from not having sufficient knowledge of these conditions. In the chapter, each atmospheric parameter is evaluated in detail and its impact is calculated, and the impact on device power and energy yield is quantified for various levels of atmospheric parameter knowledge.

6.1 Review of published atmospheric parameters impact methods

The concept of quantifying the effect of atmospheric parameters on system performance has focused on calculating the spectral mismatch via the use of a daily spectral enhancement factor (DSEF) [51]. Whilst a useful technique, this considers only the short-circuit current available, and does not calculate the expected output power.

A different approach examined the spectrometric characterization of a double-junction solar cell with measured quantum efficiencies, where the effective irradiance received by each junction is translated into a spectral parameter that is itself related to electrical characteristics of the cell or module in question [238, 239]. Such methods compress all the complexity of the atmosphere into a single dimensionless parameter, and it is not possible to deduce the contribution of each atmospheric parameter. In addition, a large number of measurements are required to achieve a reasonable degree of accuracy.

6.2 Simulation Approach

Previously in this thesis, the impact of various atmospheric parameters has been characterised as the difference in efficiency resulting from extreme values of individual parameters, which confirmed that of the atmospheric parameters investigated, air mass, aerosol optical depth and precipitable water have the greatest impact on system efficiency within realistic value ranges. Other atmospheric constituents such as ozone and other trace gases, such as nitrogen dioxide and sulphur dioxide, had negligible impact on CPV efficiency.

An alternative approach is used in this chapter. Through examining historically measured values of fundamental atmospheric parameters, their impact on CPV system performance is considered by taking the frequency distributions into account. The impact of each parameter on module power output is computed for three distinct locations.

Simulations have been performed to calculate the power output of a CPV system previously deployed at Toyohashi, Japan, using the previously validated model, with a temporal resolution of 15 minutes, over entire annual periods, resulting in electrical energy yields. Varying levels of knowledge about the atmospheric parameters has been modelled; the most basic level of knowledge is when only the date, time and location are known, hence allowing an estimate of the air mass; in the most detailed simulations all relevant available atmospheric parameters are used. The availability of atmospheric data is demonstrated to have a substantial impact on energy production and generation costs for many locations where CPV can expect

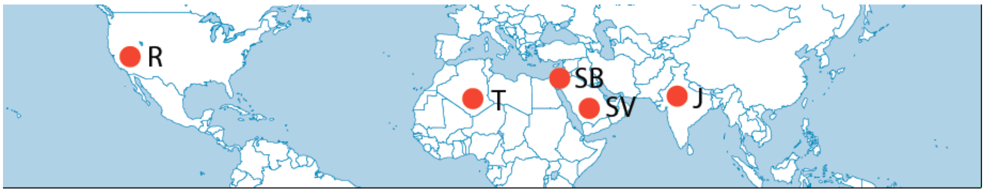

Figure 6.1: Sites investigated in this chapter - Rogers Dry Lake, USA **(R)**; Tamanrasset, Algeria **(T)**; Sede Boqer, Israel **(SB)**; Solar Village, Saudi Arabia **(SV)**; and Jaipur, India **(J)**

deployment.

6.3 Atmospheric Profiling

The air mass, aerosol and precipitable water data have been obtained from the Aerosol Robotic Network (AERONET) [166]. The data used has undergone a cloud screening process [167]. As CPV systems only accept the direct component of total solar irradiance, the use of cloud-screened data provides a reasonable basis for characterizing CPV performance in the deployment locations.

Data from AERONET sites in geographical areas of high CPV potential: Rogers Dry Lake, USA **(R)**; Tamanrasset, Algeria **(T)**; Sede Boqer, Israel **(SB)**; Solar Village, Saudi Arabia **(SV)**; and Jaipur, India **(J)** is used. Locations are indicated in Figure 6.1, whilst the years selected and estimated cloudless solar yields are given in Table 6.3. A full annual cycle for each site has been assessed and is broadly representative, as demonstrated later in this chapter.

Location	**Simulation Period**	**Modelled Cloudless Solar Yield (kWh/m^2/year)**
Rogers Dry Lake	2001-01-01 to 2002-01-01	1663.37
Tamanrasset	2007-01-01 to 2008-01-01	1424.50
Sede Boqer	2006-01-01 to 2007-01-01	1436.05
Solar Village	2001-01-01 to 2002-01-01	1677.17
Jaipur	2010-09-01 to 2011-09-01	772.57

Table 6.1: Locations of potential CPV sites Investigated and their modelled cloudless solar yield, using all available atmospheric parameters.

Our baseline spectrum is the ASTM G-173 Direct Reference, detailed in 2.19, and the parameter values used to generate it are shown in Table 3.1. The cell temperature has been maintained at 25^{0}C, or 298K, in line with concentrator standard test conditions in order to isolate the effects of the solar spectrum. It is known that this will vary in realistic deployment conditions, but temperature measurements are not always available for the AERONET sites investigated.

6.3.1 Profiling of Air mass

Values for the solar zenith angle are provided at each AERONET site , and Equation 2.3 is invoked to calculate air mass. This is primarily a function of time of day and the planetary tilt. For the locations examined, the air mass distributions show negligible differences, due to their similar latitudes. In Figure 6.2 a distribution is presented for all locations encompassing the years indicated. A plot of simulated module power against air mass is shown in Figure 6.3.

6.3.2 Profiling of Aerosols

AERONET measurements are used to supply the inputs required by the SMARTS code. AERONET sites provide AODs at a select number of wavelengths (generally including 440, 675, 870 and 1020nm). AOD$_{500}$ is derived from these measurements using the Angström relation, described in Equation 2.5, and Equation 6.1, making use of the measurements that bracket

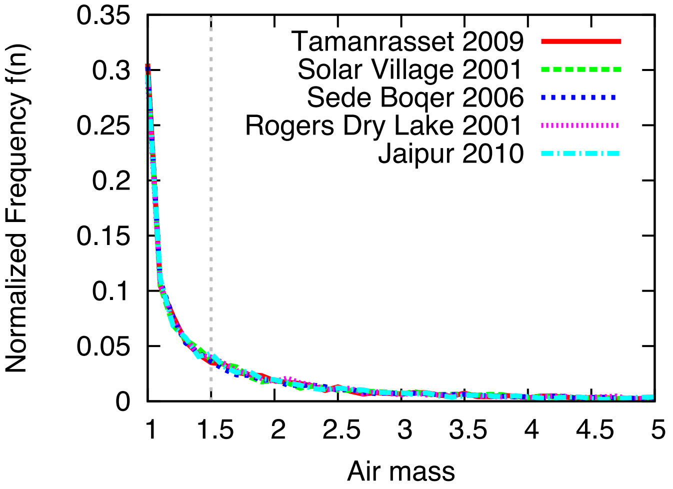

Figure 6.2: Normalised frequency distribution of air mass.

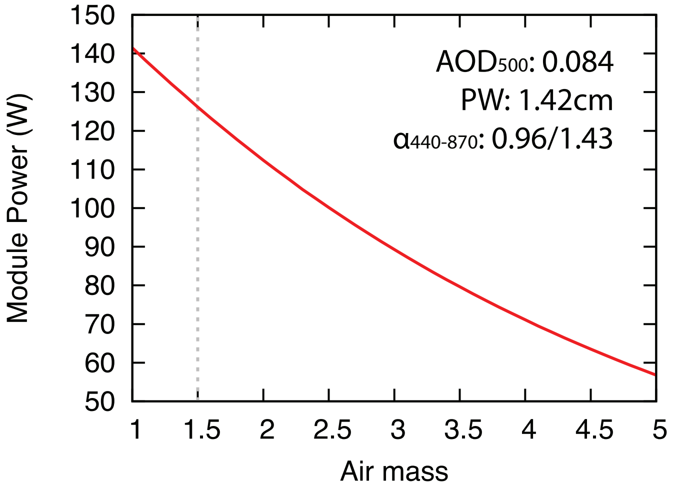

Figure 6.3: Power response of CPV module to changing air mass. For this particular system, power output generally decreases with greater air mass. All other conditions are maintained at reference values indicated. Grey dotted line indicates the value (1.5) used to generate the AM1.5D reference spectrum.

the required wavelength. In the discussion of the impact of Angström Exponent on cell performance results are framed in terms of the value calculated using AODs measured at 440 and 870 nm, $\alpha_{440-870}$ (Equation 6.2), in order to provide a degree of consistency with products that are routinely available from the AERONET website.

$$\tau_{500} = \tau_{440} \left(\frac{\lambda_{500}}{\lambda_{440}} \right)^{\left(\frac{ln \frac{\tau_{440}}{\tau_{675}}}{ln \frac{\lambda_{675}}{\lambda_{440}}} \right)} \tag{6.1}$$

$$\alpha_{440-870} = \frac{ln \left(\frac{\tau_{440}}{\tau_{870}} \right)}{ln \left(\frac{\lambda_{870}}{\lambda_{440}} \right)} \tag{6.2}$$

Another publication [240] has examined the yearly mean values of turbidity (expressed as aerosol optical depth at 1000nm) at a wide range of locations, which is related via the Angström Exponent to AOD_{500}. Though this is a useful first step, AOD_{500} can vary substantially from the average. Here, long-term data has been examined for the locations identified in Figure 6.1 - a frequency distribution of AOD_{500} values for each site is given in Figure 6.4 alongside the simulated power response of the module to changing AOD_{500} in Figure 6.5.

In the majority of locations, AOD_{500} values much larger than the reference value, indicated by the grey vertical line, are common. As expected, the shapes of the AOD distributions are essentially log-normal, with the distribution of values at Rogers Dry Lake showing significantly lower levels of aerosol loading compared to the other sites highlighted here.

Using a similar approach to examine the Angström Exponent for the same locations, the normalised frequency distributions of are presented in Figure 6.6. Clear differences again exist between locations, for example at Tamanrasset and Solar Village where one would expect the predominant aerosol type to be dust the Angström Exponent values are small, whereas at Rogers Dry Lake and Jaipur, high Angström Exponent values indicate the majority of particles are of a small size, typically associated with soot and agricultural byproducts [50, 241].

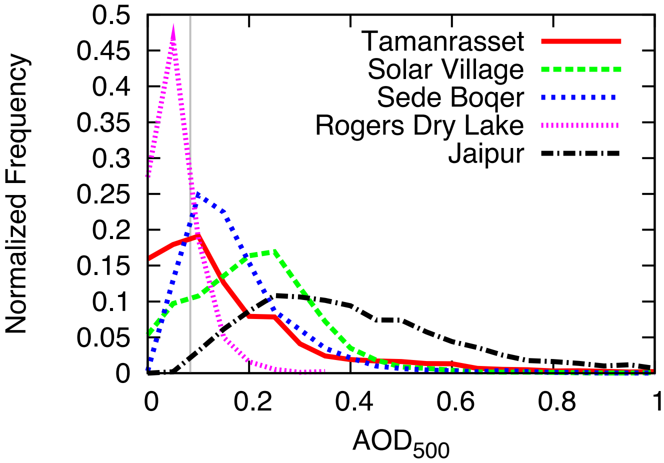

Figure 6.4: Normalised frequency distribution for Aerosol Optical Depth at 500nm (AOD_{500}) for various locations, extracted from AERONET database. Grey vertical line indicates the value (0.084) used to generate the AM1.5D reference spectrum.

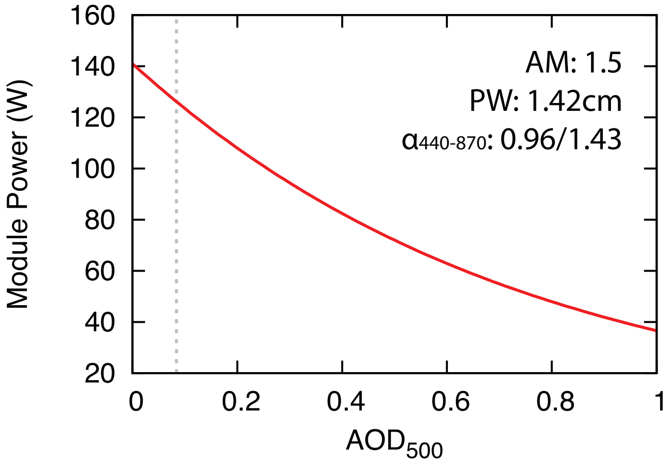

Figure 6.5: Power response of CPV module to varying AOD_{500}. Decreasing power is seen as with AOD_{500} increases. All other conditions are maintained at reference values indicated. Grey vertical line indicates the value (0.084) used to generate the AM1.5D reference spectrum.

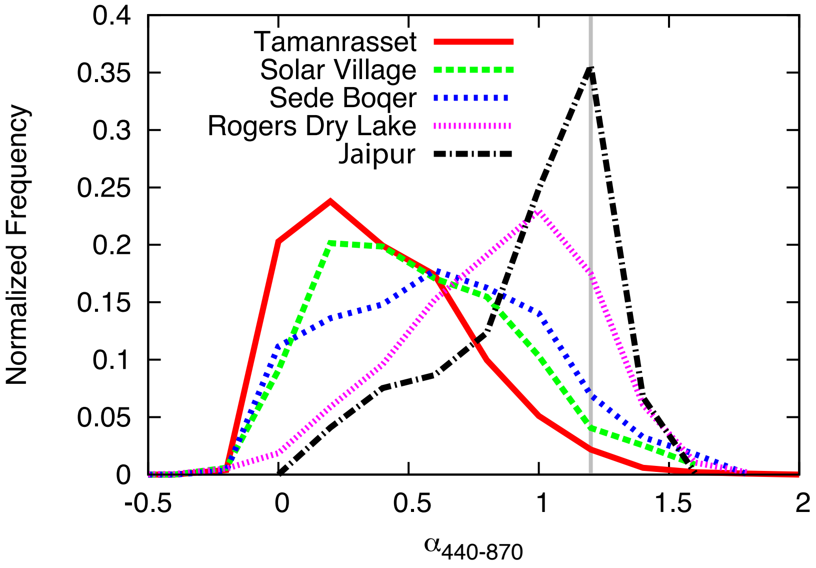

Figure 6.6: Normalised frequency distribution for Angström Exponent, evaluated between 440 and 870nm ($\alpha_{440-870}$), for various locations and extracted from AERONET database. Grey vertical line indicates the mean value (1.2) used to generate the AM1.5D reference spectrum.

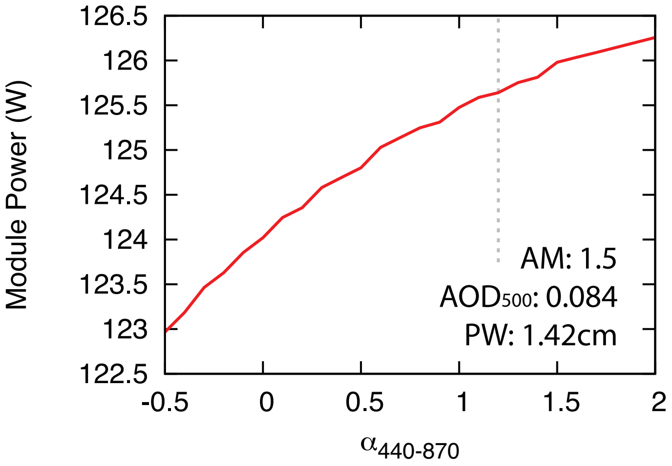

Figure 6.7: Power response of CPV module to changing Angström Exponent. All other conditions are maintained at reference values indicated. Grey vertical line indicates the mean value (1.2) used to generate the AM1.5D reference spectrum.

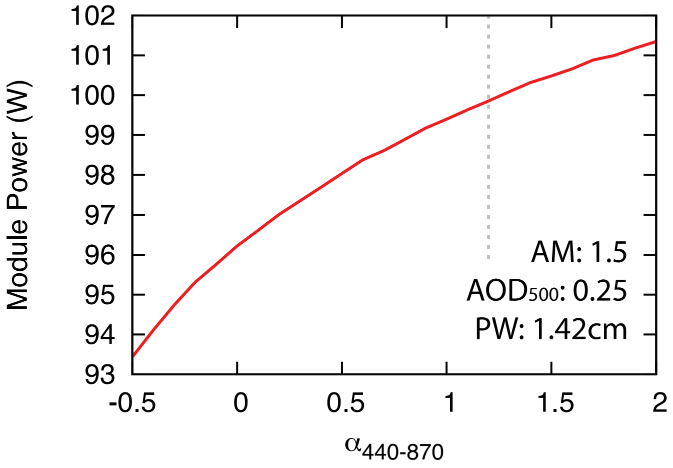

Figure 6.8: Power response of CPV module to changing Angström Exponent under higher aerosol loading.

In Figure 6.7, module power is simulated as a function of Angström Exponent, with AOD maintained at the reference value - in this case, module power does not change greatly as AOD is low. At higher aerosol loading (represented by higher AOD), the device power will be lower at the same Angström Exponent, when compared to Figure 6.7, due to greater attenuation of light, but the effect of changes in Angström Exponent will be amplified, as seen in Figure 6.8.

The distribution for AOD_{500} and Angström Exponent are noted to change slightly on an inter-annual basis as seen in Figure 6.9 and 6.10. Given the significant impact on cell performance of AOD_{500} in particular, this highlights the need for long-term observations of spectral aerosol optical depth, and/or the ability to accurately predict these data. However, for this initial study, one set of annual data at each location can give an insight into the impact of aerosols on CPV system response.

Also calculated are 2-dimensional normalized frequency histograms (Figure 6.9 - 6.10) examining the covariance of aerosol optical depth at 500nm and the Angström exponent, evaluated between 440 and 870nm, for Rogers Dry Lake, Sede Boqer and Jaipur for the simulation periods given in Table

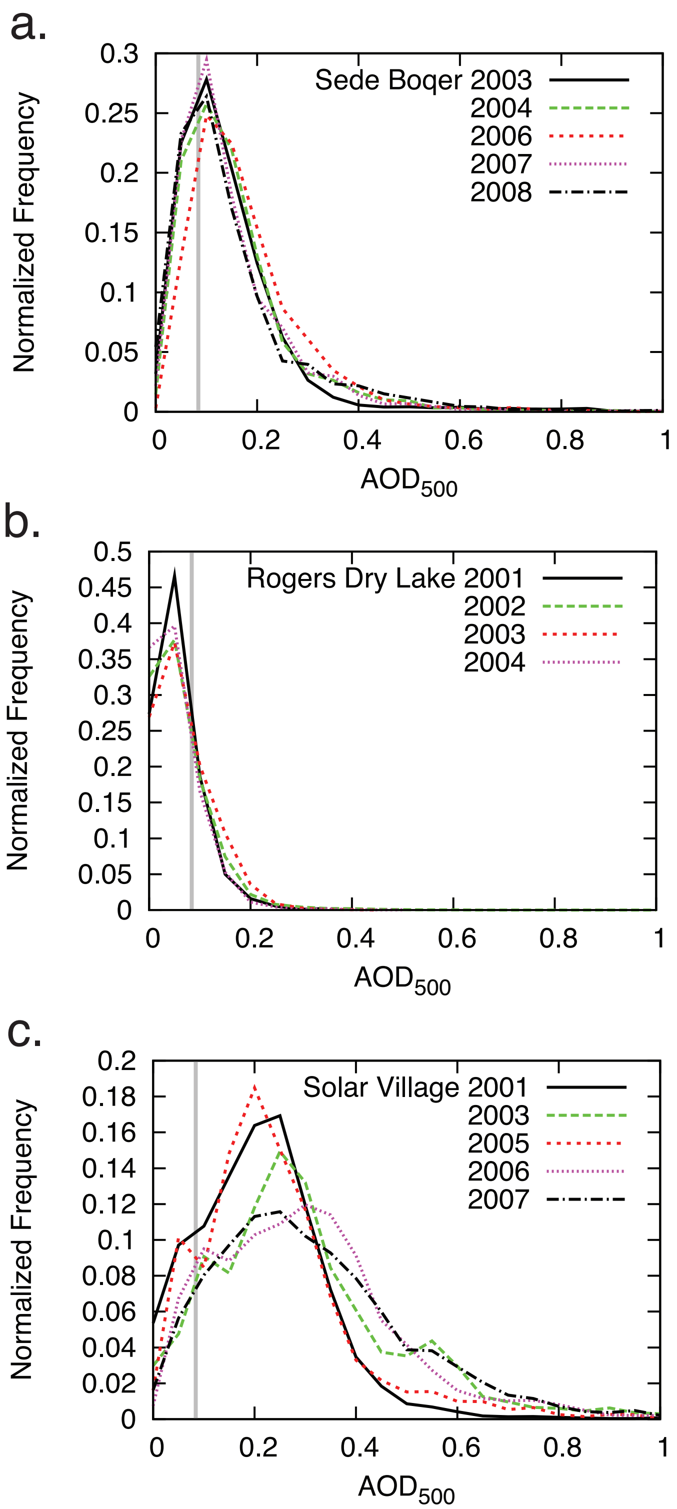

Figure 6.9: Normalised frequency distribution of AOD_{500} over multiple years, at (a)Sede Boqer; (b) Rogers Dry Lake and (c) Solar Village during the years indicated.

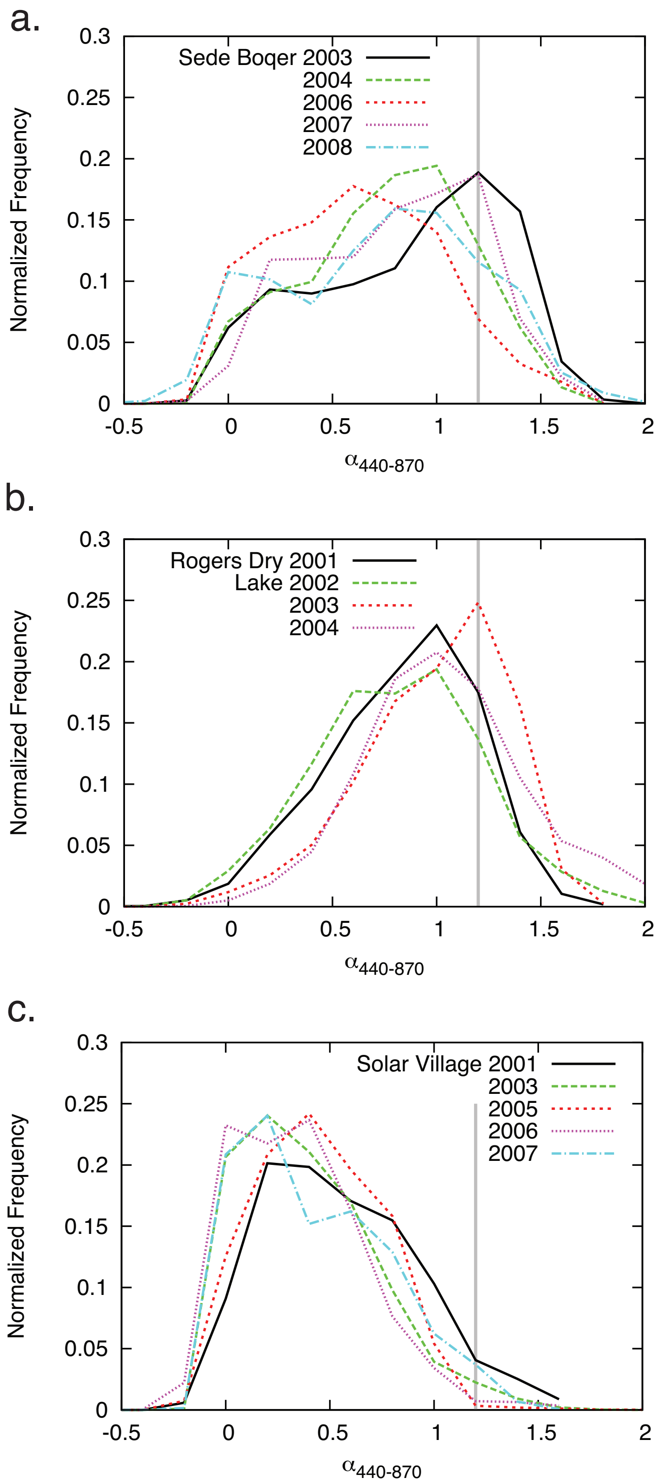

Figure 6.10: Normalised frequency distribution of Angström Exponent ($\alpha_{440-870}$) over multiple years, at (a)Sede Boqer; (b) Rogers Dry Lake and (c) Solar Village during the years indicated.

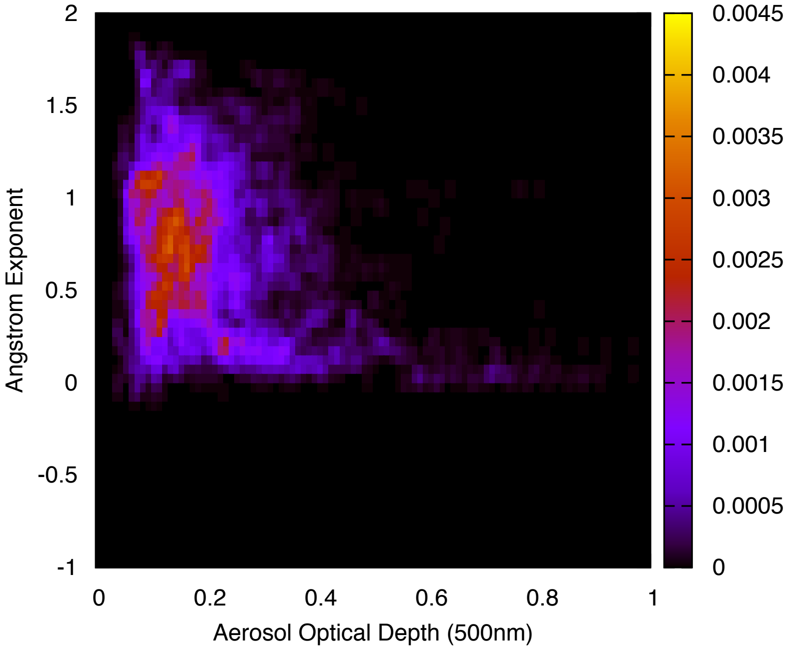

Figure 6.11: Normalised frequency contour map for AOD_{500} and $\alpha_{440-870}$, for Sede Boqer. Colour contour represents the normalised frequency.

6.3. Distinct differences can be noted for each site, particularly in Jaipur, where high Angström Exponents dominate, indicating smaller aerosol particles. Such variations serve to highlight the need to consider the covariance between aerosol optical depth and Angström Exponent carefully.

6.3.3 Profiling of Precipitable Water

In Figure 6.14, the distribution of measured precipitable water values are given for the same locations discussed in previous sections, alongside the module power response to changing precipitable water in Figure 6.15. Most of the locations considered here are desert-like and correspondingly exhibit a skewed distribution consistent with dry conditions. Tamanrasset is situated at an altitude of 1385m, so measurements made here are above the lowest kilometer or so of atmosphere where the highest concentrations of water vapour (and potentially dust aerosol) would be expected. Jaipur has

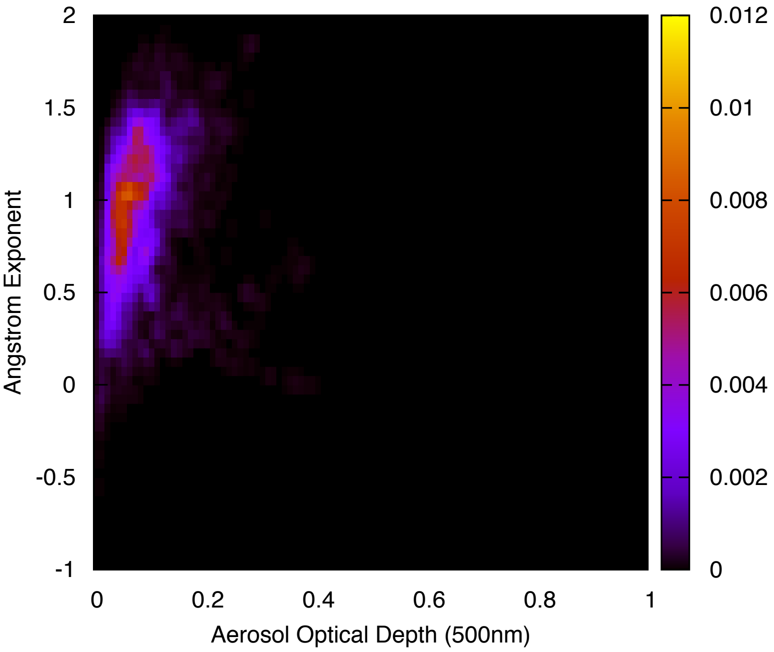

Figure 6.12: Normalised frequency contour map for AOD_{500} and $\alpha_{440-870}$, for Rogers Dry Lake. Colour contour represents the normalised frequency.

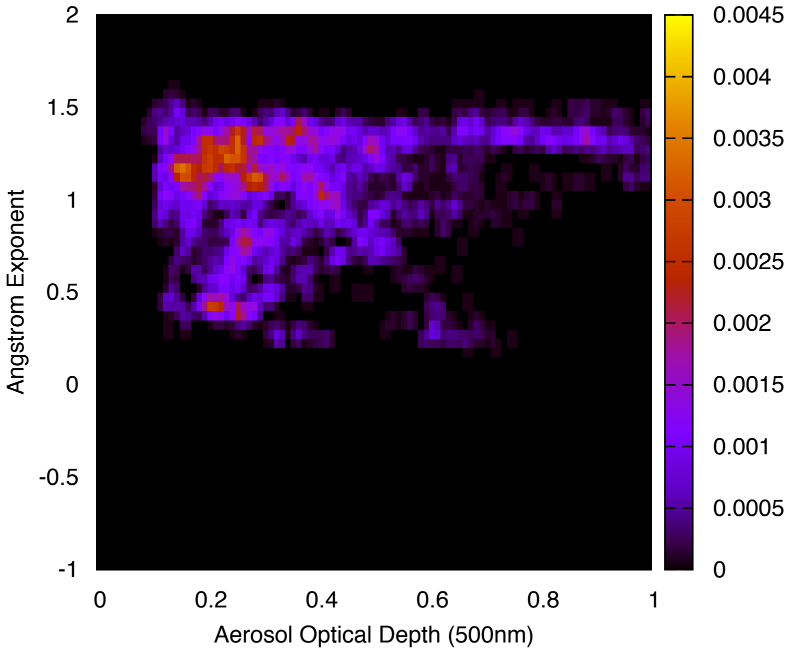

Figure 6.13: Normalised frequency contour map for AOD_{500} and $\alpha_{440-870}$, for Jaipur. Colour contour represents the normalised frequency.

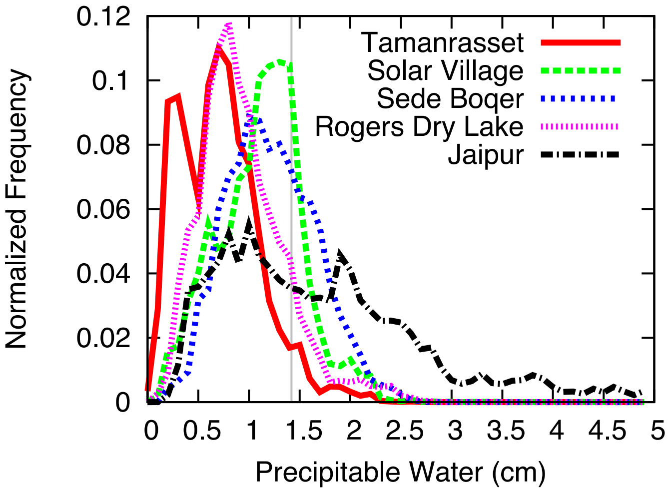

Figure 6.14: Normalised frequency distribution of precipitable water for various locations, extracted from AERONET database. Grey line indicates the value (1.42cm) used to generate the AM1.5D reference spectrum.

a large range of precipitable water values, with the highest values recorded in the period from July to September and coinciding with the Indian summer monsoon [242].

No significant inter-annual differences in the PW frequency distribution for Sede Boqer, Solar Village and Rogers Dry Lake are seen, as shown in Figure 6.16.

6.4 Quantifying the Impact of Atmospheric Parameters on CPV Power

The influence of atmospheric parameters has previously been defined as the difference in module efficiency between the most extreme parameter values recorded over the test period. Drawing on each parameters long-term normalised frequency distribution from Section 6.3 and taking into account the likelihood of each value occurring, it is possible to calculate the impact on power, ΔP, due to each parameter or set of parameters. The proposed methodology can be applied in any location to modules and cells of any size

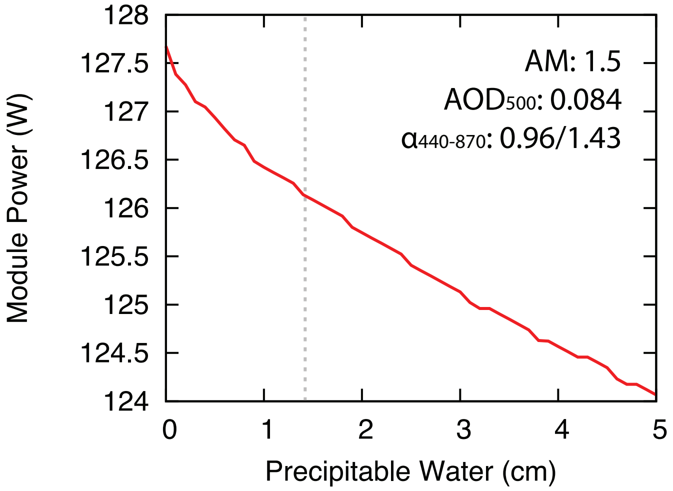

Figure 6.15: Power response of CPV module to varying PW. All other conditions are maintained at reference values as indicated. Grey line indicates the value (1.42cm) used to generate the AM1.5D reference spectrum.

and design, provided sufficient data is available.

Correlation exists between AOD and Angström Exponent, and thus they are considered together, forming a 2-dimensional frequency distribution. The combined impact of AOD and Angström Exponent will be referred to as aerosols. The expected impact on power for air mass (ΔP_{AM}), precipitable water (ΔP_{PW}) and aerosols ($\Delta P_{Aerosols}$) is given in mathematical form in Equations 6.3 - 6.5.

$$\Delta P_{AM} = \sum_{n} [P_{AM1.5D} - P_{AM}(n)] \times f_{AM}(n) \tag{6.3}$$

$$\Delta P_{PW} = \sum_{n} [P_{AM1.5D} - P_{PW}(n)] \times f_{PW}(n) \tag{6.4}$$

$$\Delta P_{Aerosols} = \sum_{m} \sum_{n} [P_{AM1.5D} - P_{AOD,\alpha_{440-870}}(m,n)] \times f_{AOD,\alpha_{440-870}}(m,n) \tag{6.5}$$

where $P_{AM1.5D}$ represents module power under the AM1.5D reference

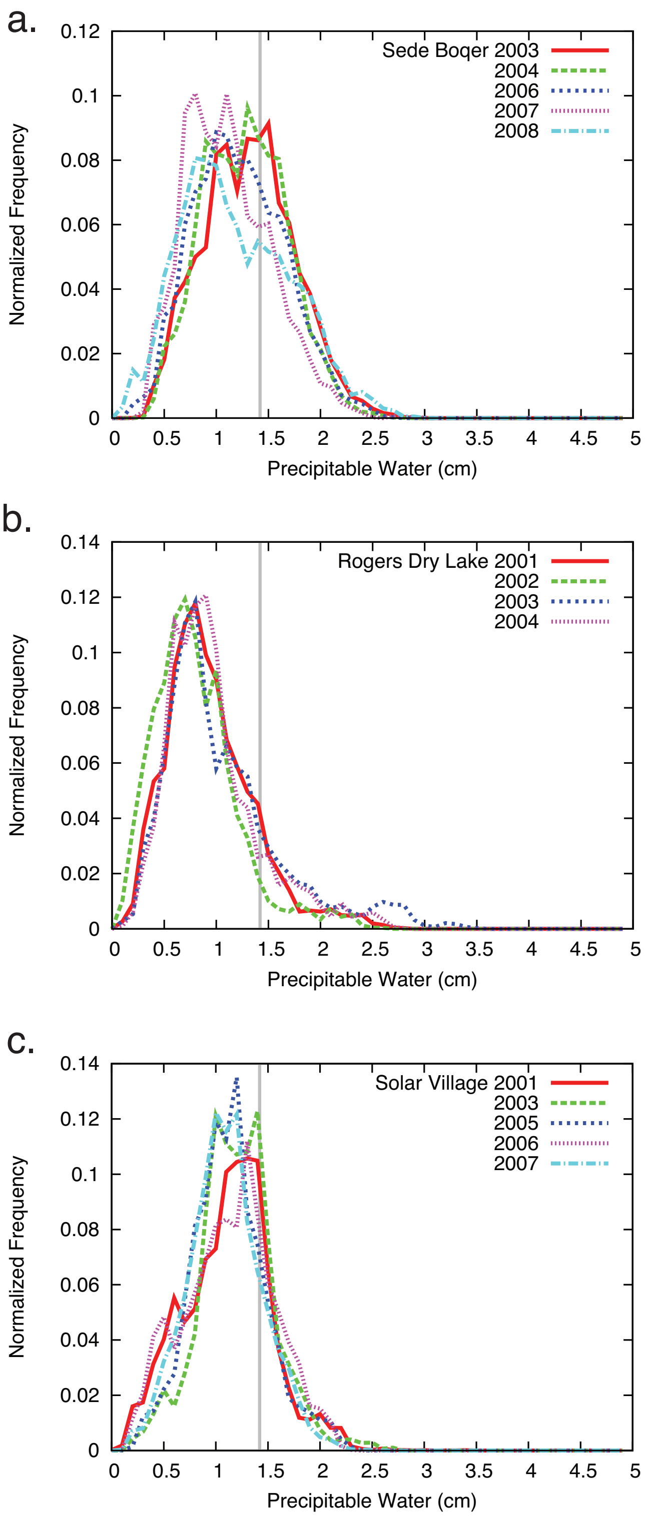

Figure 6.16: Normalised frequency distribution of precipitable water over multiple years, at (a)Sede Boqer; (b) Rogers Dry Lake and (c) Solar Village during the years indicated

spectrum illumination; $P_{AM}(n)$, $P_{PW}(n)$, $P_{AOD,\alpha_{440-870}}(m,n)$ represent the module power at parameter value n (in the case of aerosols, parameter values m and n). $f(n)$ and $f(m,n)$ represent the normalized frequency distribution associated with parameter value n (m and n in the aerosols case).

By varying the values of one parameter and calculating electrical power output of the system using the Syracuse simulation model, whilst at the same time keeping other parameters constant at AM1.5D reference values, the system responses to a single parameter can be calculated, providing the $[P_{AM1.5D}-P_{AM}(n)]$, $[P_{AM1.5D}-P_{PW}(n)]$ and $[P_{AM1.5D}-P_{AOD,\alpha_{440-870}}(m,n)]$ terms.

To obtain the expected change in power from each parameter, Equations 6.3 - 6.5 are applied to each value of n (or m and n, in the case of aerosols), multiplying the normalized frequency with power deviation. This is performed individually for air mass, aerosols and PW.

Since AOD and Angström Exponent are strongly correlated, a two-dimensional frequency distribution is required. It must be stressed that such a tool is far more useful when used to consider the relative importance of certain atmospheric parameters on a CPV module, rather than determining the exact power output. For that, detailed simulations as discussed in Section 6.5 are essential.

In Table 6.4 the calculated impact of each parameter on device power at the previously highlighted locations is shown. At Rogers Dry Lake, California, USA, air mass is revealed to be the parameter with the largest impact on power. In all other locations, particularly Jaipur, India, the impact of aerosols is comparable than air mass, whilst the impact of precipitable water is small for this particular system at all locations for the cell under consideration. In Chapter 5, precipitable water was shown to have a non-trivial impact on module efficiency, and this result is still consistent, but it is that a different metric (module power output) is examined here.

Location	$\Delta \mathbf{P}_{Airmass}$	$\Delta \mathbf{P}_{Aerosols}$	$\Delta \mathbf{P}_{PrecipitableWater}$
Rogers Dry Lake	-30.80 W	1.08 W	0.56 W
Tamanrasset	-29.99 W	-15.58 W	0.77 W
Sede Boqer	-30.71 W	-18.47 W	0.34 W
Solar Village	-30.95 W	-23.30 W	0.42 W
Jaipur	-30.65 W	-46.17 W	0.04 W

Table 6.2: Impact of air mass, precipitable water and aerosols on module power over an annual period, compared to calculations using the AM1.5D reference spectrum. In all locations except Rogers Dry Lake, aerosols are responsible for a substantial drop in rated power. Precipitable water causes little change in module power, due to the presence of an over-producing Ge junction.

Such results suggest that the variability in aerosol loading and characteristics can only be neglected in certain areas, such as the southwestern United States. In the other locations investigated here, aerosols must be accounted for if accurate estimates of performance are to be made.

In addition, aerosols and precipitable water have been examined separately here. Precipitable water is seen to have little impact on power, due to the presence of a Germanium bottom junction that overproduces current in comparison to the top and middle junctions. In devices that are better current-matched, for example where the Germanium bottom junction in the standard triple junction device is replaced with a higher band gap material, PW is expected to have a greater impact. Absorption in the relevant bands will decrease the available current to the bottom junction, increasing the impact of precipitable water. In those situations, any covariance between PW and aerosols due to the uptake of water will add complexity and must be accounted for.

6.5 Simulated Energy Yields - Data Denial

For the best estimates of energy yields from a CPV system at a particular location, a time-resolved set of simulations using all available atmospheric parameters should offer the highest accuracy. In some geographical locations, there may be very few sites measuring these parameters, or none at all. It is instructive to consider the potential errors that may arise, given various levels of knowledge regarding the atmosphere. Although satellite retrievals of atmospheric parameters can be used to supplement direct in-situ and ground based measurements orbital constraints mean that they are not always available at the desired timescales or locations. In addition, the inversion process, coupled with differences in the area being sampled can result in significant differences when the products are evaluated against direct measurements [243].

Cloudless AERONET data is used to obtain information on air mass, aerosols and precipitable water. Simulations are performed at the same time as AERONET measurements, ensuring cloudy conditions are filtered out.

6.5.1 Module Power Output Simulation Methodology

Over annual periods, the system performance for the module described in Section 2 is simulated using the Syracuse computer program. I-V characteristics are output for each simulation point and the maximum power point is found, with trapezoidal integration invoked to obtain an estimate of the energy yield. As before, the temperature is maintained at 298K (25oC) for all simulations, in order to isolate the effect of the solar spectrum on system output.

AERONET measurements are made approximately every 15 minutes given the air mass is less than 5. For Sede Boqer in 2006, it would have been possible for AERONET to make measurements for 98.0% of the DNI delivered. Similarly, for Tamaransset in 2007 and Solar Village in 2001, the equivalent figures are 97.6% and 98.6% respectively, indicating AERONET measurements are representative of a large proportion of the energy delivered. At higher air mass, horizon shading from mountains and structures may also affect any measurements.

Data collected is subject to a quality assurance process and a cloud filter, which examines the variation in the calculated aerosol optical depths [24]. Beyond a certain variation threshold, the measurement is treated as cloudy, leading to gaps in the cloudless data.

System performance is simulated whenever an AOD measurement is made, making the assumption that data gaps of 30 minutes or longer are due to cloudy conditions, not instrument error or downtime, and make no effort to include them in calculations of the energy output. A schematic of the integration method is given in Figure 6.17.

Although there is no measured system output to compare against at these locations, experience from Chapter 5 indicates that given the correct DNI and spectral distribution, system behaviour can be reproduced to an appropriate degree of accuracy, where the annual energy yield is within 2% of measured values.

The number of atmospheric parameters used in the simulation has been varied to investigate the effect of data denial on energy yield. At the lowest detail level, only air mass is known, and all other parameters are set to default AM1.5D conditions. Progressively more atmospheric parameters are added, until air mass, precipitable water, AOD_{500} and $\alpha_{440-870}$ are all included in the highest detail simulation.

6.5.2 Comparison of Predicted and Measured DNI

First, measured DNI data is compared with model estimates generated by SMARTS 2.9.5 at Tamanrasset and Sede Boqer. Observations were taken from the Baseline Surface Radiation Network (BSRN) [143] over a range of atmospheric conditions. From the results, during cloudless periods one can be reasonable confident that the modelled and actual broadband DNI are in good agreement. Examples of the measured and simulated broadband DNI on select days are given in Figure 6.18 - 6.21, where sudden dips in the measured irradiance are attributable to cloud cover. Red crosses indicate simulations where only the air mass is varied from reference conditions. Blue stars indicate simulations where all available atmospheric knowledge is used. DNI clearly varies substantially depending on atmospheric knowledge, particularly during periods with high aerosol loading.

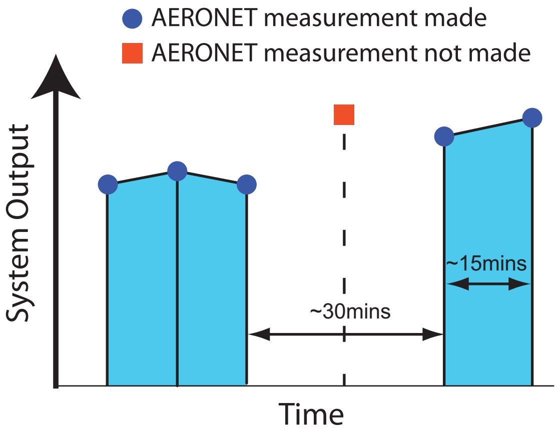

Figure 6.17: Schematic of energy yield integration approach - given an air mass value lower than 5, AERONET measurements are made approximately every 15 minutes. Data gaps of 30 minutes or greater are assumed to be due to cloudy conditions, and are not included in calculations of energy yield.

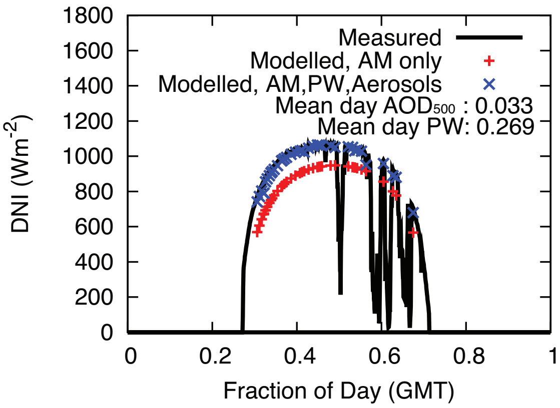

Figure 6.18: Measured DNI and modelled cloudless DNI on 2007-01-12 at Tamanrasset, with low aerosol loading.

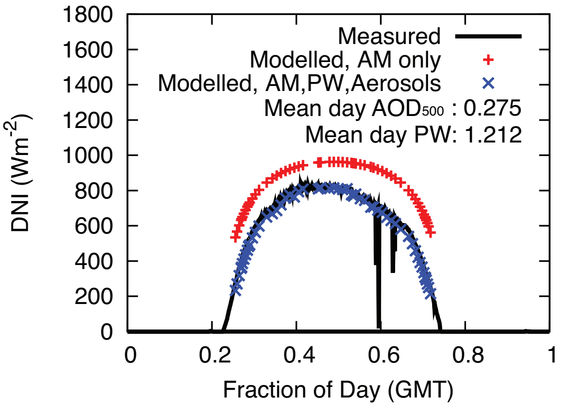

Figure 6.19: Measured DNI and modelled cloudless DNI on 2007-08-09 at Tamanrasset, with elevated aerosol loading.

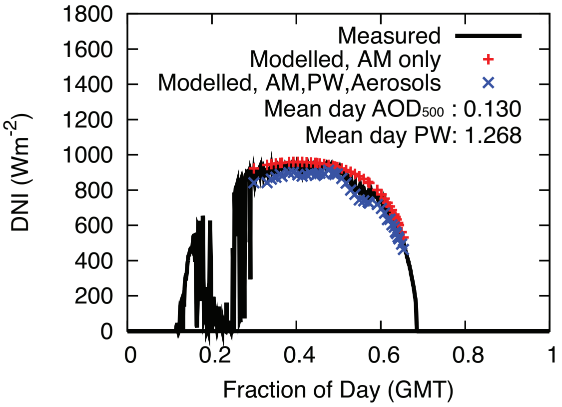

Figure 6.20: Measured DNI and modelled cloudless DNI on 2006-06-11 at Sede Boqer, with low aerosol loading.

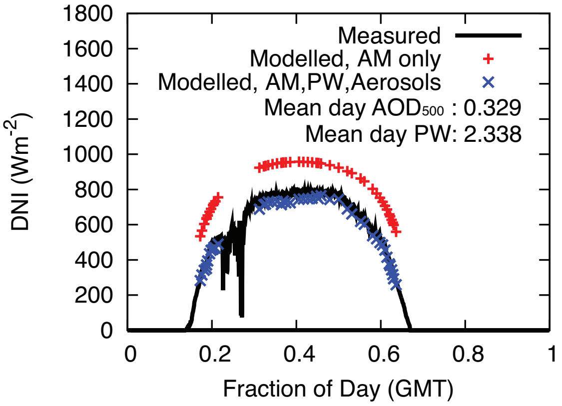

Figure 6.21: Measured DNI and modelled cloudless DNI on 2006-08-19 at Sede Boqer, with elevated aerosol loading.

6.5.3 Simulation Results

With this methodology, the set of candidate CPV locations has been investigated. By examining the module power output for the most basic and complex cases over the single days considered in Figures 6.22-6.25, clear differences in power exist depending on the atmospheric parameters included.

When examined over annual periods, such variations become apparent in the estimated cloudless electrical energy yields, listed in Table 6.5.3, with the percentage deviation from the best effort simulation in brackets. A graphical representation of the estimated annual electrical energy yields at different detail levels is given in Figure 6.26. Up to 75% deviation in energy yield can be noted between the most basic and complex simulations. In most locations, the difference is substantial - indicating a need to correctly capture the atmospheric state should any realistic estimates of energy yield need to be made.

Notably, at Rogers Dry Lake, the differences are much smaller, and knowledge of additional atmospheric parameters has no significant impact on the energy yield. Amonix CPV systems have shown agreement between measured and simulated energy yields of within 1% can be achieved in this geographical area [149], and such behaviour is observe this within the sim-

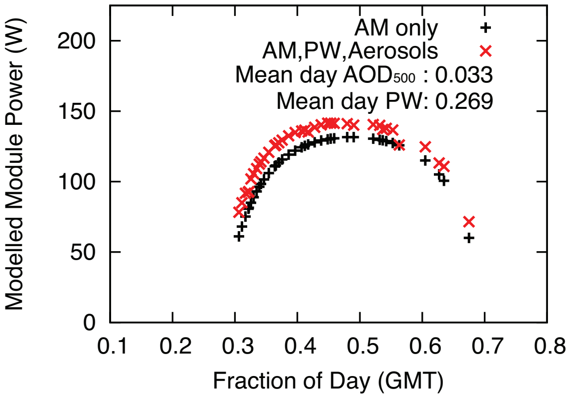

Figure 6.22: Modelled module power output on 2007-01-12 at Tamanrasset.

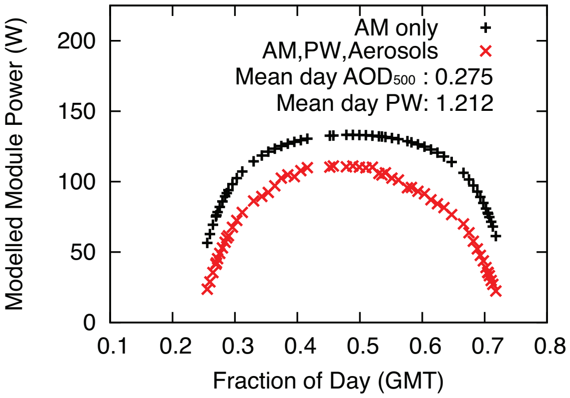

Figure 6.23: Modelled module power output on 2007-08-09 at Tamanrasset.

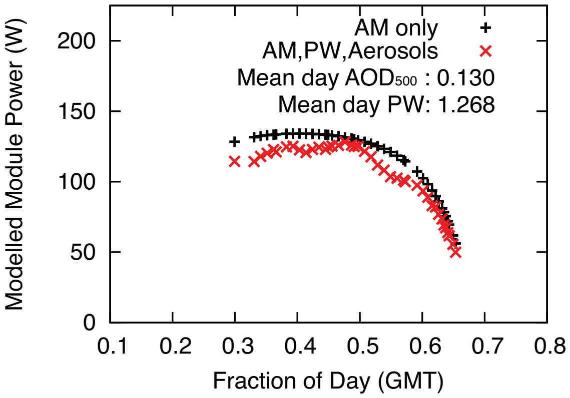

Figure 6.24: Modelled module power output on 2006-06-11 at Sede Boqer.

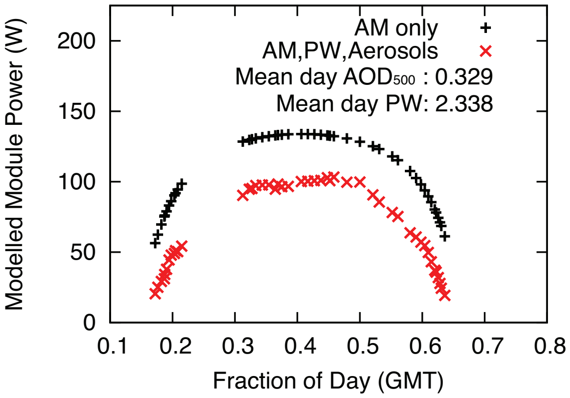

Figure 6.25: Modelled module power output on 2006-08-19 at Sede Boqer.

	Annual Energy Yield (kWh)				
Detail Level	**Rogers Dry Lake**	**Tamanrasset**	**Sede Boqer**	**Solar Village**	**Jaipur**
Air mass PW AOD$_{500}$ $\alpha_{440-870}$	237.55 (-)	201.18 (-)	180.40 (-)	202.93 (-)	95.51 (-)
Air mass PW AOD$_{500}$	238.97 (+0.6%)	206.09 (+2.4%)	184.52 (+2.3%)	208.36 (+2.7%)	74.93 (-27.5%)
Air mass PW	236.08 (-0.6%)	235.12 (+16.9%)	217.71 (+20.7%)	252.97 (+24.7%)	130.04 (+36.2%)
Air mass	235.38 (-0.9%)	234.00 (+16.3%)	217.15 (+20.4%)	252.50 (+24.4%)	167.12 (+75.0%)

Table 6.3: Simulated energy yields for a single module at five locations, with various levels of atmospheric data knowledge. Percentage deviation from the best effort yield in each location is shown in bracketed text. In the basic case, only air mass is known. In the most detailed simulations, air mass, precipitable water, AOD$_{500}$ and $\alpha_{440-870}$ are all used.

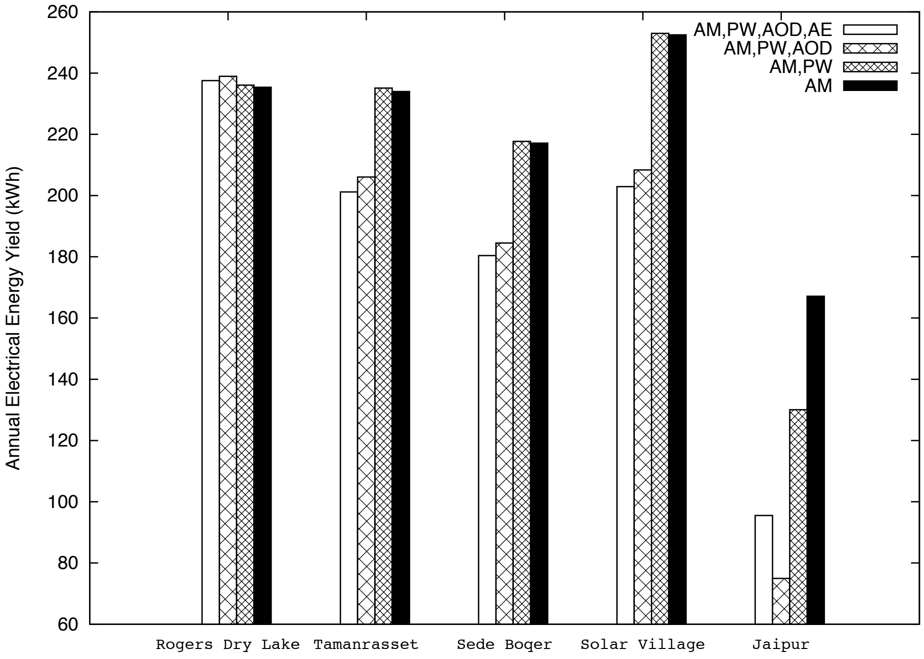

Figure 6.26: Simulated annual energy yields for a single CPV module at 5 locations, with various levels of atmospheric data knowledge.

ulations. This is to be expected as the AM1.5D reference conditions were selected to be representative of the southwestern United States, the geographical region of Rogers Dry Lake [217]. The frequency distribution for AOD_{500} shows a strong skew towards lower values, which from Figure 6.3 one would expect to result in a low impact on power for this system. In addition, as the average values for each parameter are close to the AM1.5D values, the availability of additional parameters does not result in large differences in the energy yield calculations.

At Jaipur, there is a dramatic difference of 75% in energy yield between the basic and most detailed simulations, due principally to higher AOD500 values. The Angström Exponent, related to aerosol size, is also shown to have a significant impact on energy yields. This highlights a need to consider all relevant atmospheric parameters if future CPV deployment in locations with significant and variable aerosol loading, such as the Indian subcontinent, is to be successful. It is however apparent that the energy yield at Jaipur is substantially lower than other locations in all cases, due to more frequent cloud cover at the site.

Jaipur has been identified as a site with high DNI potential [244, 245] and is in the same geographical region of many bids for the deployment of up to 500MW of photovoltaic systems under the Jawaharlal Nehru National Solar Mission [246], an initiative from the Government of India. Given these factors, CPV deployment has been considered as a possibility in the region.

Further, it must be noted that specifically for this solar cell structure, knowledge of precipitable water only has a small impact on the energy yield of this particular system, but the added knowledge of aerosol has a large effect, in agreement with the results in Table 6.4 .

6.6 Impact of Atmospheric Parameters on Cost of Energy

By examining the impact of atmospheric parameters on CPV systems and examining their relative importance, investors will be able to make informed decisions as to which measurements are required to accurately predict CPV system performance at a particular location. The suitability of a system to a certain location can be assessed, assuming no drastic and sudden changes in atmospheric conditions.

For any energy system, the metric of concern to investors and consumers is the cost of the energy produced. Levelised Cost of Energy (LCOE) is a widely accepted concept describing the cost at which energy must be sold to break-even over the technologys lifetime, in both flat-plate and concentrator photovoltaics [109, 221, 247] . A simplified version is presented in Equation 6.6, adapted from [247], to illustrate the need to consider atmospheric parameters in modelling when calculating energy production costs for CPV systems.

$$[H]LCOE = \frac{Lifecycle\ Cost}{Lifetime\ Energy\ Generation} = \frac{PC + \sum_{n=1}^{N} \frac{AO}{(1+DR)^n}}{\sum_{n=1}^{N} \frac{E_{initial}(1-SDR)^n}{(1+DR)^n}} \tag{6.6}$$

In this formalism, PC represents the project cost, DR is the discount rate, AO is the annual operation and maintenance cost, SDR is the system yield degradation rate, and N is the number of years of system operation. The project cost is assumed to be paid in full at the start of the project, and no assumptions have been made regarding the value of the system after 30 years. Values used in this calculation are given in Table 6.6, and are based on estimates made in other publications regarding commercially viable photovoltaic power plants [247–249]. The installed cost is the best estimate for the present installations, but this is expected to decrease as the technology matures. The energy yields used are taken from Table 6.5.3, assuming electrical power generated in North Africa is, in this case, exported to Europe, similar to the DESERTEC concept [250]. The resulting LCOE values are shown in Table 6.6 for different levels of atmospheric knowledge. Higher system power output naturally leads to lower LCOE, with the lowest generation costs associated with Rogers Dry Lake.

The average LCOE for each technology in the United States, Europe and India have been derived from publications by the International Energy

Parameter	**Value**
Installed Cost ($/W)	2.5
Size of Plant	500 MW
Operation and maintenance ($/W per year)	0.01
Project lifetime (years)	30
Discount rate (%)	5
Energy yield degradation rate (% per year)	0.5
Total capital cost ($USD)	3x10^{9}
Percentage of capital cost paid up front (%)	100
Annual insurance cost ($USD)	15x10^{6}

Table 6.4: List of values used in the LCOE calculations, the basis for these assumptions can be found in [247–249].

	Levelised Cost of Energy ($USD/kWh)		
Detail Level	**Rogers Dry Lake**	**Tamanrasset**	**Jaipur**
Air mass PW AOD_{500} $\alpha_{440-870}$	0.076	0.090	0.190
Air mass PW AOD_{500}	0.076	0.088	0.243
Air mass PW	0.077	0.077	0.140
Air mass	0.077	0.078	0.109
Δ LCOE	-1.3%	+15.4%	+74.3%

Table 6.5: Estimated Levelised Cost of Energy (LCOE) for CPV systems sited at Rogers Dry Lake, Tamanrasset and Jaipur. All costings are in $USD/kWh. Percentage difference in LCOE between the most basic and most detailed simulations give in the last row.

Agency [251] and the World Bank [252], and are compared to the estimated LCOE for CPV systems, depending on the amount of atmospheric data used in the simulation. Figures 6.27-6.29 indicate CPV can be cost competitive with both coal and gas in the United States regardless of atmospheric parameters availability and given the assumptions listed, but its competitiveness will change substantially in Europe and India depending on the simulation detail level. It is noteworthy that at Jaipur, CPV is much more competitive than off-grid diesel generation in all cases.

Having assumed that the cost for the system remains the same regardless of deployment location, the predicted energy generation term changes depending on the level of knowledge regarding atmospheric conditions, the difference in LCOE between the most basic (only air mass is known) and complex (air mass, aerosols and precipitable water are known) cases can be expressed as in Equation 6.7.

$$\Delta LCOE = \frac{LCOE_{AM} - LCOE_{AM,PW,AOD_{500},\alpha_{440-870}}}{LCOE_{AM,PW,AOD_{500},\alpha_{440-870}}} \times 100 \qquad (6.7)$$

For the years examined, in some locations LCOE can be up to +75%, leading to substantially higher LCOE when more atmospheric information is incorporated this is particularly important for locations with highly variable aerosol loading such as Jaipur, India. Little deviation in LCOE is seen for Rogers Dry Lake as expected, given its similarity to reference conditions.

6.7 Summary

An approach has been developed to quantify the impact of individual atmospheric parameters on the performance of CPV systems based on physical phenomena. It has been shown that in addition to air mass, aerosols can have a large impact on the power output of a system at many sites considered suitable for CPV. In many locations, it has been demonstrated that key atmospheric parameters must be considered for accurate energy yield estimates. Precipitable water is noted to have little impact on module power and energy yield for this particular triple-junction, but this is expected to change when other designs with better current-matching are considered.

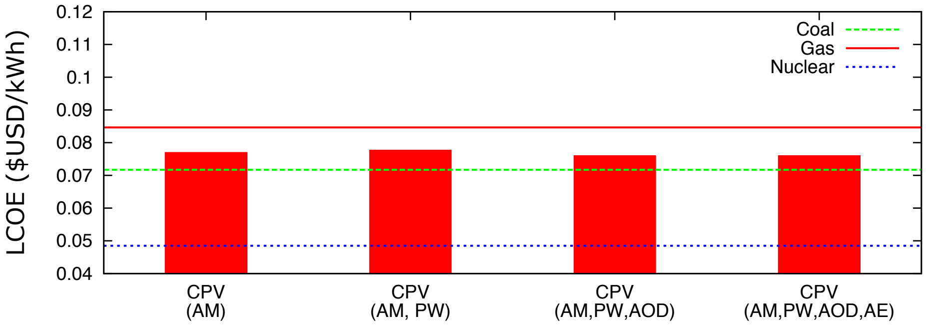

Figure 6.27: Levelised Cost of Energy from a hypothetical 500MW CPV power plant for the USA. Energy yields from Rogers Dry Lake used.

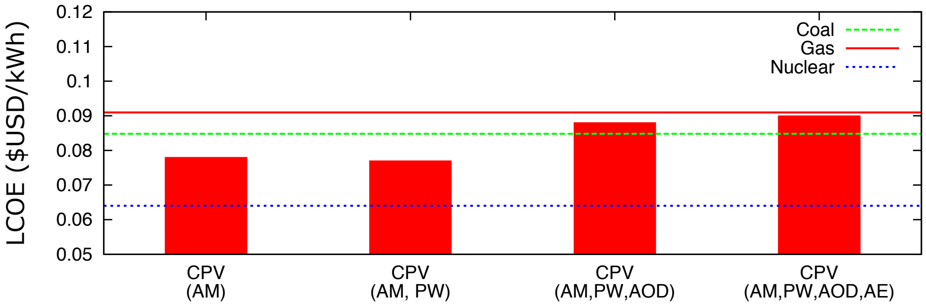

Figure 6.28: Levelised cost of energy from a hypothetical 500MW CPV power plant sited in North Africa, exporting energy to Europe. Energy yields from Tamanrasset used.

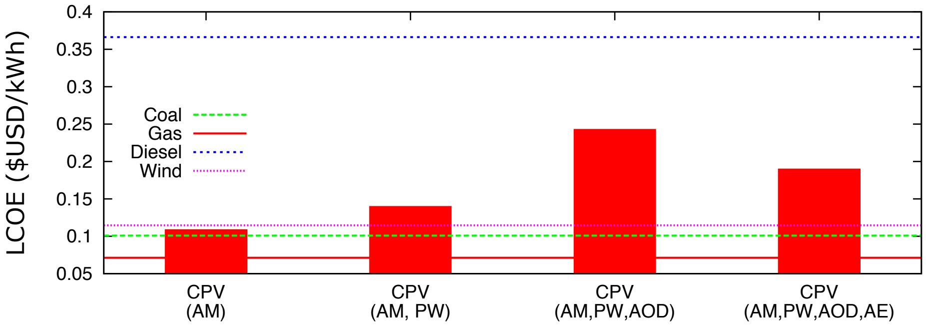

Figure 6.29: Levelised cost of energy from a hypothetical 500MW CPV power plant for India. Energy yields from Jaipur used. Diesel represents off-grid diesel generators.

The frequency distributions of air mass, aerosol optical depth, Angström Exponent and precipitable water have been calculated for several locations across the globe, showing substantial variation from the AM1.5D reference conditions.

Cloudless-sky simulations using atmospheric data from AERONET measurements with high temporal resolution were performed for several sites over annual periods. The simulated energy yield can vary by up to 75% between the most complex case where all available parameters are used, and the most basic simulation, where only air mass and the location is known. Notably, at Rogers Dry Lake in the southwestern US, the differences are small, and can be attributed to the similarity between the atmospheric parameters at this site and the AM1.5D reference conditions.

Further, difference in energy yields between the most basic and complex cases is shown to increase the levelised cost of energy by up to 25% for many locations with high solar irradiance. Locations with complex atmospheric conditions, such as Jaipur, show a difference of up 75% in LCOE depending on the atmospheric parameters available for energy yield modelling.

The results contained in this chapter demonstrate the need for system designers, developers and investors to obtain a sufficiently detailed understanding of the atmospheric conditions prior to deployment of any CPV system in a new location. Failure to account for these factors are likely to lead to significant differences between projected and realised energy production and cost of energy, and the profitability of a project.

7 Radiative Coupling

Management of photons emitted by a solar cell can lead to enhanced performance of the device - in particular, the radiative losses from one junction can be captured by a subsequent lower band gap junction - this is referred to as radiative coupling. Past publications have dealt with the enhancement offered when the effect is captured under detailed balance, and several studies have experimentally verified the presence of the radiative coupling effect in multijunction solar cells under laboratory conditions. To date, no studies have systematically evaluated the enhancement for cells that operate away from the detailed balance limit, and under realistic atmospheric conditions. The work contained in this chapter provides analysis of the power and energy yield enhancement from radiative coupling, and provides hints for why this effect has not been observed for deployed systems.

7.1 What is radiative coupling?

Radiative recombination losses from semiconductor materials results in the emission of light at the band gap energy of the material. This light can either: escape from the device; be reabsorbed by the junction from which it was emitted; or be escape to the adjacent junctions of a multijunction solar cell. Photon emission from radiative recombination from a higher band gap junction can be absorbed by a subsequent lower band gap junction. Once in the adjacent junction, this light can be absorbed and contribute to the photocurrent in that particular junction. In essence, the performance of one junction is coupled to that of another through the absorption of radiative recombination, giving rise to the *radiative coupling* effect. The concept is illustrated in Figure 7.1. This physical effect is referred to in a number of different publications using slightly different language, such as *optical coupling* [253], *luminescent coupling* [119,254] and *radiative coupling* [255,256].

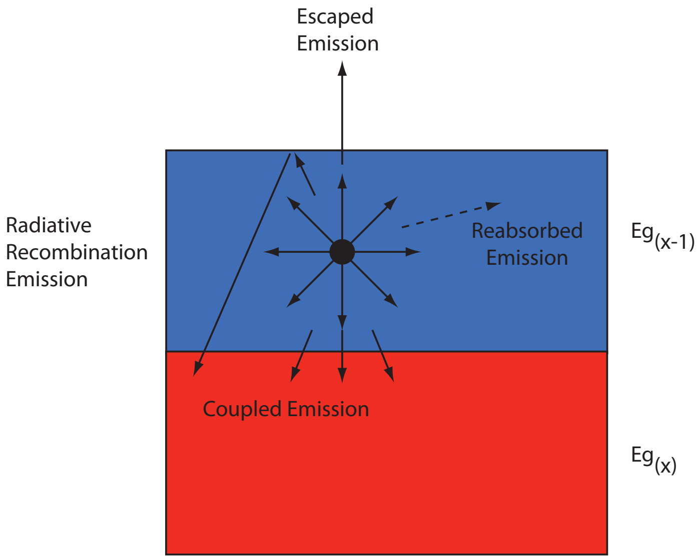

Figure 7.1: Radiative coupling concept - radiative recombination is emitted as light, either escaping from the device, reabsorbed by the same junction, or transmitted to a lower band gap junction, where it can be absorbed.

Marti et al. explored this concept in their publication on the detailed balance on the limiting efficiency of a MJSC [177], whilst Brown and Green expanded on this idea in their detailed-balance treatment of a 2-junction MJSC [256], showing theoretical efficiency enhancement due to radiative coupling depends on differences in refractive index of the device and its surroundings. In [256] it was calculated that by applying appropriate designs, strong radiative coupling in a 2-junction MJSC can result in a cell that offers relatively high efficiency across a range of air mass values, provided the cell is optimised for a higher air mass. Only radiative recombination (derived from the Generalised Planck equation, given in Equation 4.2) is considered, with unity absorption above the band gap energy, and zero absorption below. This is referred to as the *radiative limit*.

Yoon et al. [255] performed one of the first relevant experimental studies of this effect on a number of triple-junction InGaP/GaAs/Ge devices with isotype junctions (where the top junction is made photovoltaically inactive through doping techniques), noting the top cell can increase the middle cell photocurrent by 1-2% under 1-sun illumination conditions, with even greater enhancement under higher illumination. In multijunction solar cells this has been shown to enhance current production and is expected to increase device efficiency under laboratory testing conditions [119, 253].

More recently, Steiner et al. [254] and Derkacs et al. [119] have experimentally examined the usefulness of radiative coupling in state-of-the-art solar cells,but opinion remains divided on its usefulness in practical devices, particularly as MJSCs are sensitive to spectral conditions and the current balance between junctions. Additionally, Lee et al. experimentally demonstrates that 50% of the dark current of a multiple quantum well top junction can be coupled into the photocurrent of the subsequent junction. Brown et al., Yoon et al. and Derkacs et al. note that radiative coupling is likely to become more important as an effect in MJSCs with a greater number of junctions, due to its ability to assist with current-matching between junctions.

In the following sections, the enhancement that can be expected from radiative coupling for current and future MJSC designs is evaluated and quantified in terms of the expected *power enhancement* due to each atmospheric parameter, drawing on the previously presented frequency histograms of each parameter from Chapter 6. In addition, the expected enhancement in *energy yield* for three potential CPV deployment locations is examined for each MJSC design.

7.2 Radiative Coupling - Quantifying Power Enhancement under Realistic Atmospheric Conditions

Building on the optimal band gap investigation from Section 4.6 and atmospheric profiling detailed in Section 6.3 It is important to quantify the enhancement that can be expected for optimal devices under realistic atmospheric conditions.

In order to examine the practical limit of radiative coupling, no optical losses or parasitic resistances are included, and a single 1cm^2 solar cell under 1000X concentration is simulated. Spectral irradiance is simulated under various atmospheric conditions using SMARTS 2.9.5. The simulation approach detailed in 4.4, has been adapted to estimate the effect of radiative coupling on the current-voltage relationship. The quantum efficiency has been set at 0.98 at wavelengths above band gap and below the band gap of the previous junction. Radiative efficiency as a function of lattice mismatch is estimated using the 2013 fit identified in Figure 4.4. An important modification has been made, in that a proportion of the radiative recombination from a high band gap junction (*x-1*) can now be coupled into subsequent junction (x), provided $E_g(x-1) > E_g(x)$. The full mathematical expressions of the modifications are given in Equation 7.1 and 7.2.

$$J_{Total,x}(V_x) = J_{SC,x} - J_{01,x}(e^{\frac{qV_x}{k_BT}} - 1) - J_{02}(e^{\frac{qV_x}{2k_BT}} - 1) + J_{coupled} \tag{7.1}$$

$$J_{coupled} = F_c J_{01,x-1}(e^{\frac{qV_{x-1}}{k_BT}} - 1) \tag{7.2}$$

where F_c is the proportion of the radiative recombination that is absorbed by the subsequent junction, referred to as radiative coupling ratio, and all other symbols have their usual meanings.

From Equation 7.2 it is apparent that the coupling current is dependent on the bias of the emitting junction (*x-1*). Hence, it is important to calculate the current-voltage characteristics beginning from the junction with the highest band gap. The highest experimentally demonstrated value for F_c is 35% by Derkacs [119], who also note the theoretical maximum coupling efficiency to be 48%, based on the geometry and refractive indices of semiconductor MJSCs.

To quantify the potential power enhancement available from strong radiative coupling, F_c values of 0% and 48% are used in the simulations for the non-coupled and radiatively-coupled cases respectively. The percentage difference in estimated output power is given by $\Delta \mathrm{P}_{coupling}$, where:

$$\Delta P_{coupling} = 100 \times \frac{P_{48\%\ coupling} - P_{0\%\ coupling}}{P_{0\%\ coupling}} \tag{7.3}$$

By considering Kirchoff's Current law for a monolithic tandem MJSC where the junctions are electrically series-connected, the performance enhancement form the radiative coupling effect is strongest where light is coupled *into a junction that limits the flow of current through the entire device*, i.e. the junction that produces the least current. It is least useful when light is coupled into a junction that already overproduces current.

Two optimum state-of-the-art cell structures identified earlier in Section 4.6 - the upright MM and the IMM MJSCs - have been investigated for the performance enhancement that can be expected from radiative coupling. In addition, the industry standard LM triple junction structure and a future MJSC design based on the IMM structure with four junctions described by Stan et al [257] are examined with the same rigour. The band gaps for each of the four structures and the short circuit current calculated under 1000X AM1.5D reference conditions for a 1cm^2 device is detailed in Figure 7.2.

The enhancement in module power as a function of key atmospheric pa-

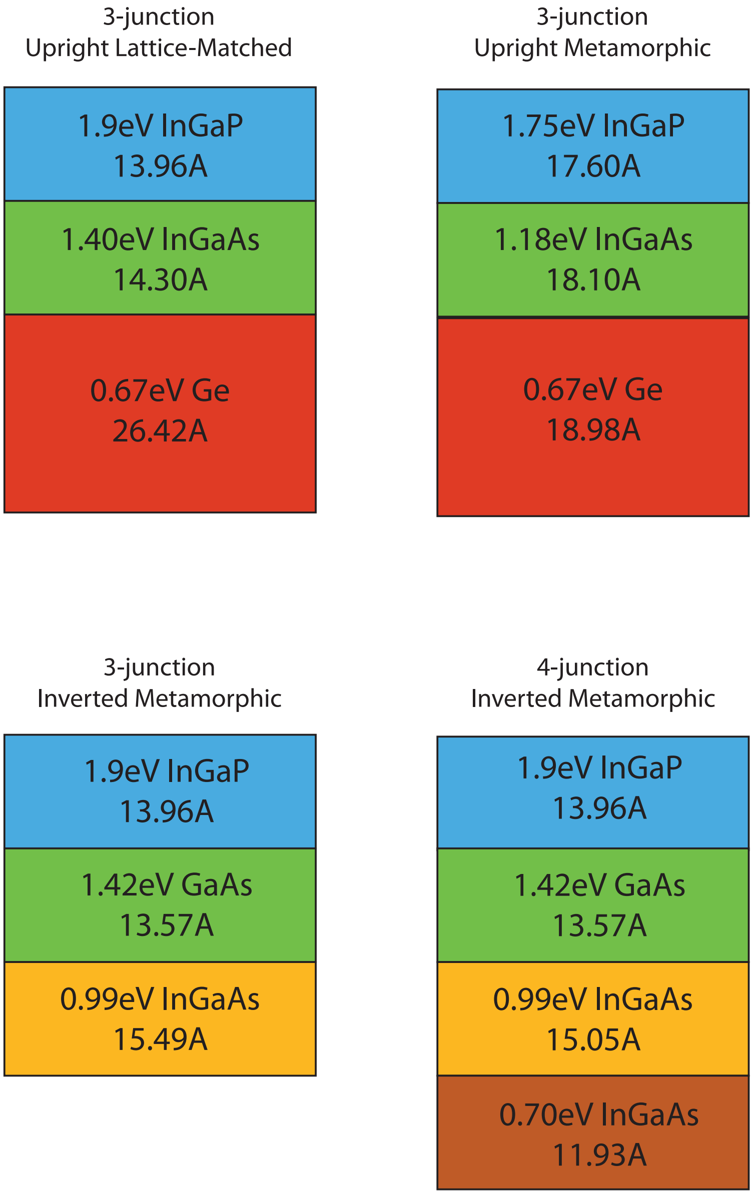

Figure 7.2: Band gaps and short circuit current for simulated MJSC structures in the radiative coupling investigations, under 1000X AM1.5D illumination on a $1cm^2$ device.

rameters are expressed graphically in Figures 7.3 - 7.8. Unless otherwise stated, all other variables are set at the CSTC reference values described in Table 3.1. In addition, the short circuit current of each junction is given for specific points, demonstrating that radiative coupling provides the greatest enhancement when higher band gap junctions possess the greatest short circuit current, followed by the next highest, and so on. It can be seen from Figures 6.2 - 6.16, however, that these conditions are rarely observed for the locations examined. Air mass values of less than 1 are only likely to occur at very high altitudes, whilst there are relative few instances of aerosols with low Angström exponent, associated with large particles.

As expected, radiative coupling enhancement is greatest when light is coupled into the current-limiting junction, as illustrated by the insets in Figures 7.3 - 7.8. The effect is particularly strong for aerosol conditions where the aerosol optical depth is high, and the Angström exponent is low. It must be noted in these instances, the output power of the CPV system is substantially reduced when compared to CSTC reference conditions, and whilst the relative enhancement in power is large, the absolute enhancement will be small.

To calculate an expected value for the enhancement due to radiative coupling from each individual atmospheric parameter, the enhancement values in 7.3 - 7.8 are convolved with the normalised frequency distribution for each parameter for the three locations identified.

$$\Delta P_{coupling,AM} = \sum_{n} \Delta P_{coupling,AM}(n) \times f_{AM}(n) \tag{7.4}$$

$$\Delta P_{coupling,PW} = \sum_{n} P_{coupling,PW}(n) \times f_{PW}(n) \tag{7.5}$$

$$\Delta P_{coupling,Aerosols} = \sum_{m} \sum_{n} P_{coupling,AOD,\alpha_{440-870}}(m,n) \times f_{AOD,\alpha_{440-870}}(m,n) \tag{7.6}$$

The resulting values for the maximum expected enhancement from radiative coupling, given the upright metamorphic and inverted metamorphic

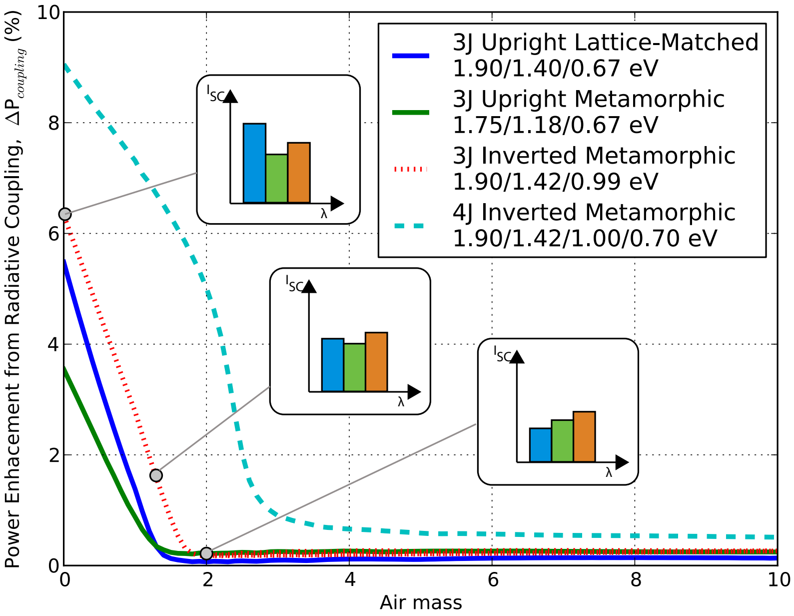

Figure 7.3: Power enhancement from radiative coupling, as a function of air mass. Greater enhancement is noted at low air mass values, where shorter wavelengths receive proportionally more irradiance.

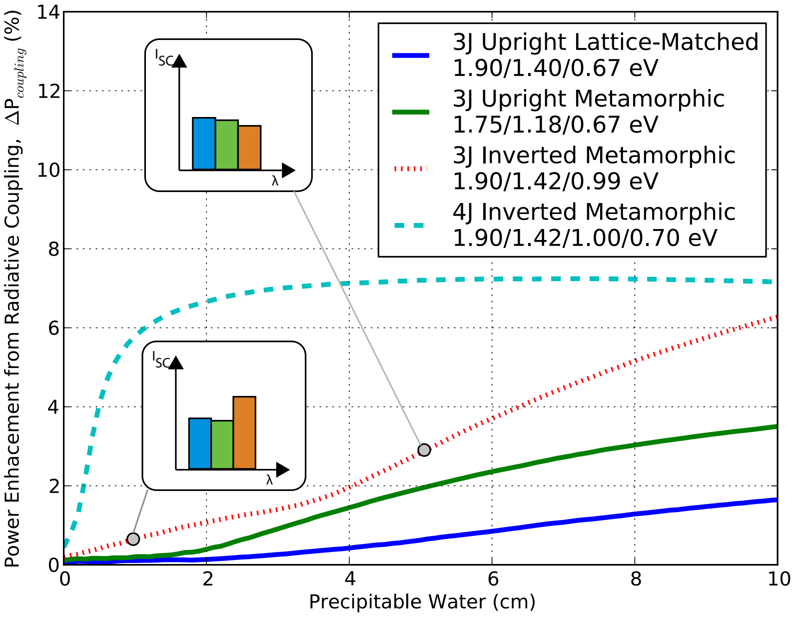

Figure 7.4: Power enhancement from radiative coupling, as a function of precipitable water. Of the two state-of-the-art MJSCs, the triple-junction IMM structure is more sensitive to irradiance losses due to precipitable water, due to its current-matched short circuit currents. The 4-junction IMM solar cells exhibits greater enhancement over a wide range of precipitable water values, as the current balance is particularly sensitive to changes in the solar spectrum.

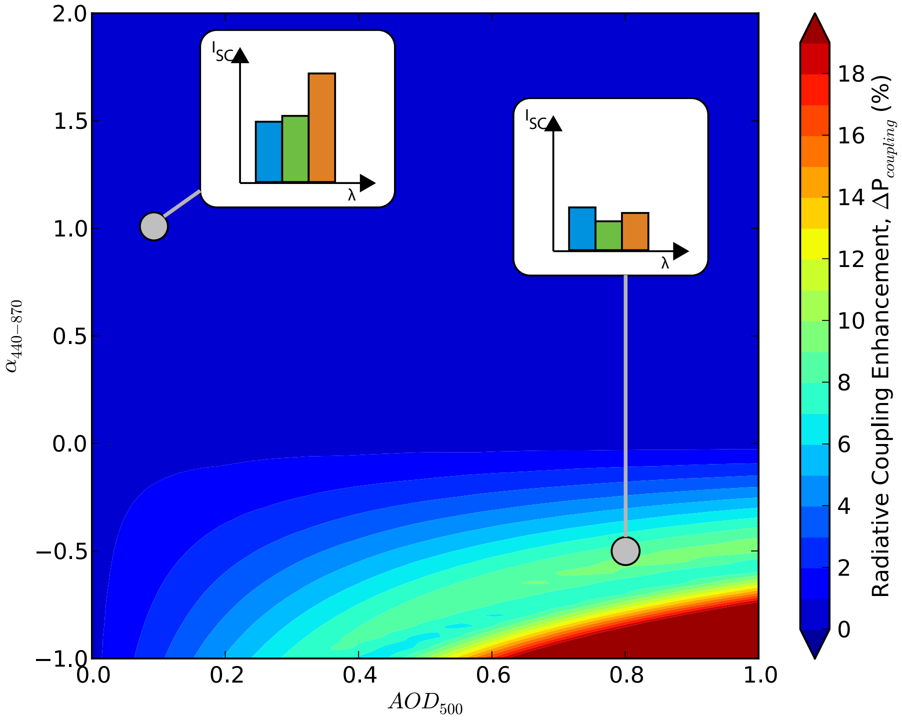

Figure 7.5: Power enhancement from radiative coupling, as a function of AOD and Angström Exponent for a 3-junction upright Lattice-Matched structure.

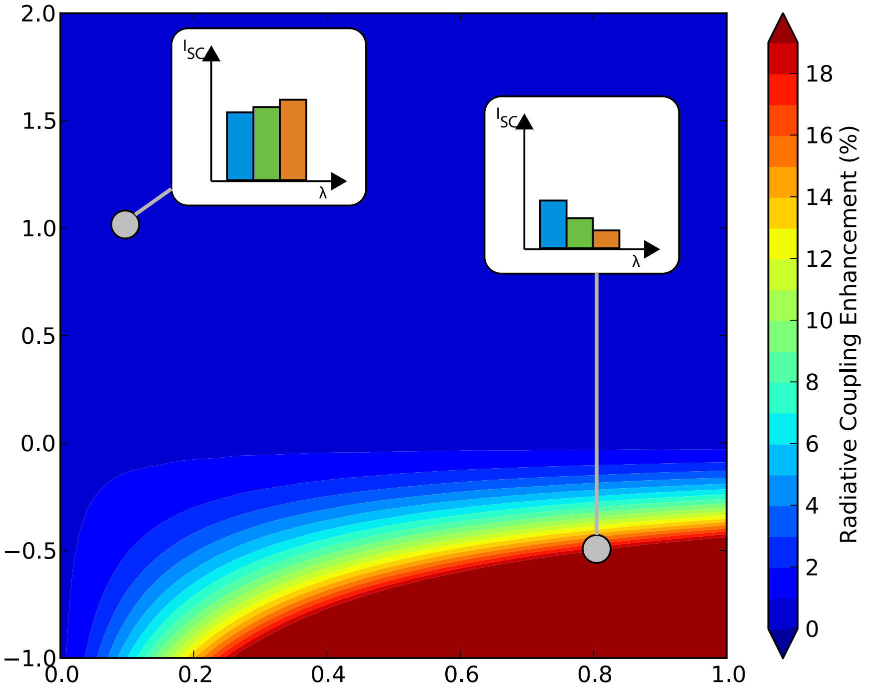

Figure 7.6: Power enhancement from radiative coupling, as a function of AOD and Angström Exponent for a 3-junction upright Metamorphic structure.

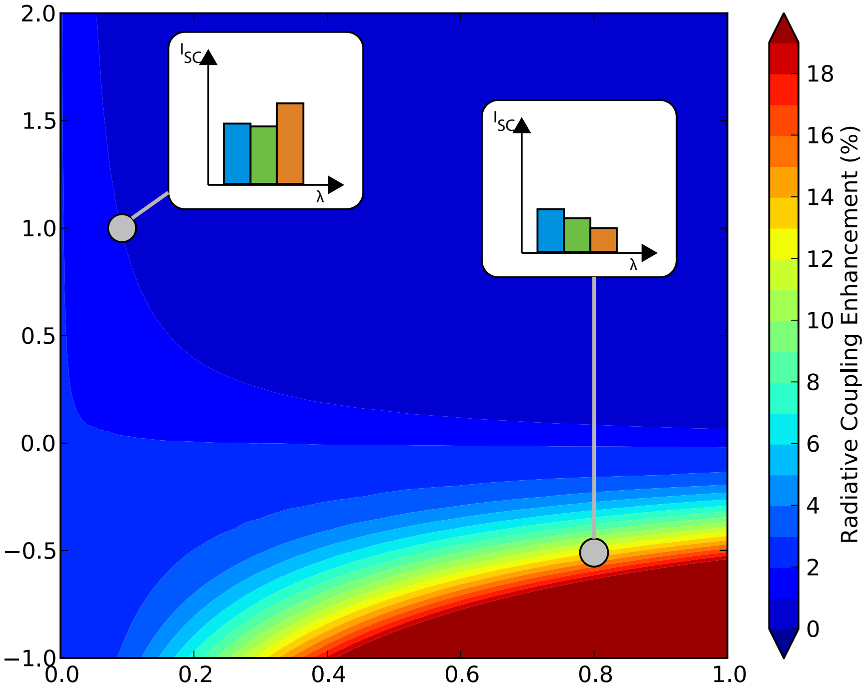

Figure 7.7: Power enhancement from radiative coupling, as a function of AOD and Angström Exponent for a 3-junction Inverted Metamorphic structure.

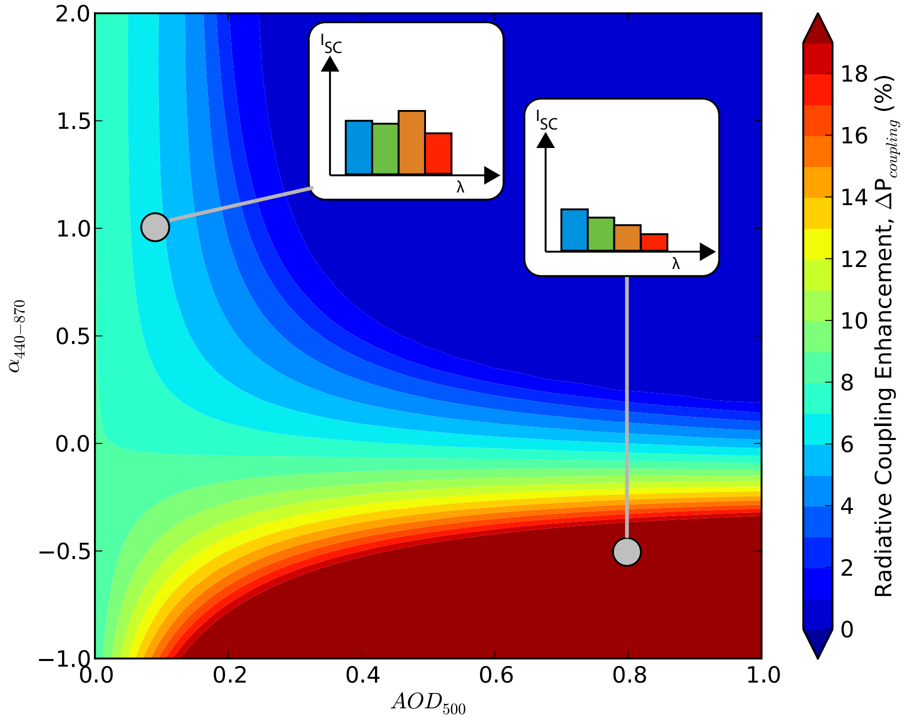

Figure 7.8: Power enhancement from radiative coupling, as a function of AOD and Angström Exponent for a 4-junction Inverted Metamorphic structure.

growth techniques and band gaps, are presented in Tables 7.1 - 7.4.

The highest calculated value for radiative coupling enhancement is +6.54%, associated with aerosols at Rogers Dry Lake using the 4-junction inverted metamorphic device. The lowest enhancement is expected for aerosols at Jaipur, at +0.08%, with the triple-junction lattice-matched MJSC. Across all devices, radiative coupling does not appear to be hugely beneficial for Jaipur's aerosol conditions, due to the high Angström exponent of the aerosols present. This results in spectra that attenuate strongly at lower wavelengths, thus reducing the photogeneration in high band gap junctions and causing them to be current limiting.

In triple-junction MJSCs, the upright metamorphic structure exhibit low enhancement from radiative coupling, due to the lower junction voltages at maximum power point, leading to lower radiative recombination. The overproducing Germanium bottom junction of the lattice-matched triple-junction device means low enhancement is to be expected with increases in precipitable water, although it has reasonable response at low air mass values. The triple-junction inverted metamorphic device exhibits the highest enhancement, due to a combination of high junction bias and the use of junctions that produce similar short circuit currents.

Inverted metamorphic devices show the highest enhancement with increasing precipitable water - this is due to their well-current matched junctions and high junction bias. In the 4-junction design, the bottom junction possesses a 0.7eV InGaAs bottom junction that is current limiting under CSTC reference conditions, hence its relatively high $\Delta P_{coupling,PW}$ across a large range of precipitable water values, as seen in Figure 7.4.

Location	$\Delta\mathbf{P}_{coupling,AM}$	$\Delta\mathbf{P}_{coupling,PW}$	$\Delta\mathbf{P}_{coupling,Aerosols}$
Rogers Dry Lake 2001	+0.29%	+0.10%	+0.26%
Sede Boqer 2006	+0.25%	+0.11%	+0.16%
Jaipur 2010	+0.21%	+0.16%	+0.08%

Table 7.1: Expected power enhancement from radiative coupling, triple-junction upright lattice-matched structure.

Location	$\Delta\mathbf{P}_{coupling,AM}$	$\Delta\mathbf{P}_{coupling,PW}$	$\Delta\mathbf{P}_{coupling,Aerosols}$
Rogers Dry Lake 2001	+0.33%	+0.21%	+0.37%
Sede Boqer 2006	+0.31%	+0.24%	+0.26%
Jaipur 2010	+0.29%	+0.43%	+0.17%

Table 7.2: Expected power enhancement from radiative coupling, triple-junction upright metamorphic structure.

Location	$\Delta\mathbf{P}_{coupling,AM}$	$\Delta\mathbf{P}_{coupling,PW}$	$\Delta\mathbf{P}_{coupling,Aerosols}$
Rogers Dry Lake 2001	+0.87%	+0.64%	+1.21%
Sede Boqer 2006	+0.78%	+0.77%	+0.80%
Jaipur 2010	+0.66%	+0.96%	+0.28%

Table 7.3: Expected Power Enhancement from radiative coupling, triple-junction inverted metamorphic structure.

Location	$\Delta\mathbf{P}_{coupling,AM}$	$\Delta\mathbf{P}_{coupling,PW}$	$\Delta\mathbf{P}_{coupling,Aerosols}$
Rogers Dry Lake 2001	+4.13%	+5.04%	+6.54%
Sede Boqer 2006	+3.95%	+5.69%	+5.06%
Jaipur 2010	+3.63%	+5.91%	+2.09%

Table 7.4: Expected Power Enhancement from radiative coupling, 4-junction inverted metamorphic structure.

7.3 Radiative Coupling - Annual Energy Yield Enhancement

In order to examine the combined impact of these effects on the cell structures identified, time-resolved simulations have been performed using atmospheric parameters for air mass, aerosol optical depth, Angström exponent and precipitable water from AERONET sites, using the methodology established in Section 6.5.

The predicted energy yields for radiative coupled (F_c=48%) and uncoupled (F_c=0%) cells are calculated and given in Table 7.5, along with the relative difference in energy yields, ΔE, given by Equation 7.7 and displayed graphically in Figure 7.9.

$$\Delta E = 100 \times \frac{E_{48\%\ coupling} - E_{0\%\ coupling}}{E_{0\%\ coupling}} \tag{7.7}$$

		Annual Energy Yield (kWh)			
Location	F_c	**3J LM**	**3J MM**	**3J IMM**	**4J IMM**
Rogers Dry Lake 2001	48%	86.53	96.47	91.99	100.21
	0%	86.18	96.17	90.93	95.53
Sede Boqer 2006	48%	66.74	74.43	71.01	77.26
	0%	66.49	74.18	70.28	74.08
Jaipur 2010	48%	48.78	55.35	52.36	58.37
	0%	48.68	55.20	52.08	57.25

Table 7.5: Simulated annual energy yield, with (F_c=48%) and without (F_c=0%) radiative coupling.

		Annual Energy Yield per kWp PV (kWh/kWp)			
Location	F_c	**3J LM**	**3J MM**	**3J IMM**	**4J IMM**
Rogers Dry Lake 2001	48%	1985	2016	2000	2067
	0%	1980	2015	1997	2099
Sede Boqer 2006	48%	1531	1555	1544	1594
	0%	1527	1554	1544	1628
Jaipur 2010	48%	1119	1156	1138	1204
	0%	1118	1156	1144	1258

Table 7.6: Simulated annual energy yield per rated kWp of installed CPV, with (F_c=48%) and without (F_c=0%) radiative coupling.

For the locations examined, the distribution in air mass is similar due to their latitudes, and so the key differences lie in the how the aerosols and precipitable water affect the current-balance of each design.

For the MJSC structures investigated, the largest impact is noted at Rogers Dry Lake for the 4-junction IMM (4J IMM) device, with an expected enhancement of +4.90% in energy yield over the course of a year. At that location, the high Angström exponent of the aerosols and the relatively high enhancement from even low values of precipitable water combine to give a high energy yield enhancement for the 4J IMM device. The lowest enhancement from radiative coupling is expected for the upright Lattice-Matched device at Jaipur, with +0.20% gain. This is likely due to a combination of the high Angström Exponent of the aerosol, the high precipitable water values and a Germanium bottom junction that overproduces current.

The results show that although the energy yield enhancement is on the same order of magnitude as the expected power enhancement when radiative coupling effects are considered, there is covariance between the relevant atmospheric parameters not captured by considering the parameters separately, and highlights the importance of time-resolved simulations.

The greater enhancement from the 4J MJSC is to be expected, as the

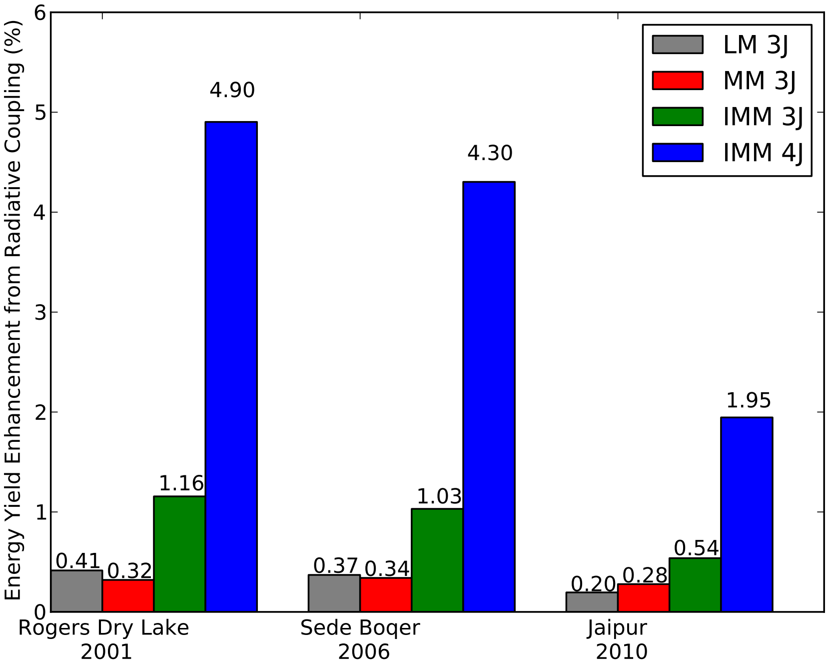

Figure 7.9: Energy yield enhancement from radiative coupling over annual periods for the locations and periods identified, with state-of-the-art and future MJSC designs.

short circuit current of each junction is lower with each additional junction, due to further splitting of the solar spectrum. Hence, the current gain from radiative coupling is a greater fraction of the photocurrent for any given bias. It is expected that the radiative coupling effect will be of at least comparable importance for the performance of MJSCs with 5 or more junctions.

As the quantum efficiencies (98% above band gap) used in this work are idealised, the enhancement from real devices with lower photocurrents may differ. The analysis here is based on the assumption that the photon absorption is maximised for each junction, and together with radiative efficiency calculations provide a practical limit to radiative coupling enhancement, assuming no parasitic resistance.

7.4 Summary and Further Considerations

Enhancement of multijunction solar cell power output and energy yield potentially providable by radiative coupling has been investigated in this section for a number of state-of-the-art and future device structures and band gaps at the practical limit. MJSC designs with junctions that possess similar short-circuit currents are shown to benefit most from radiative coupling. The radiative coupling enhancement is calculated as a function of air mass, precipitable water and aerosol properties, and the expected *power* enhacement from each parameter is quantified.

Time-resolved calculations have been performed, showing up to 4.90% enhancement in annual energy yield for the 4-junction inverter metamorphic design. The energy yields of current industry standard of upright lattice-matched and optimal upright metamorphic designs are shown to only benefit slightly (<0.4 %) from radiative coupling, due to large current mismatches in the former and low junction bias in the latter. Current triple-junction inverted metamorphic MJSCs can expect an annual energy yield enhancement of around 1% from radiative coupling.

The idealised quantum efficiencies used in this investigation provide the practical limit of photocurrent generation, but it must be noted that the balance in current between junctions is crucial, and that a small change in the short circuit current can affect the radiative coupling enhancement. The possibility of using quantum well structures to enhance both radiative coupling and the photocurrent in a junction remains to be explored in detail.

It is recognised that the coupling ratio, F_c, was set at 48%, providing the practical limit for MJSCs. The latest measurements indicate that F_c=35% has been achieved, and that this figure is dependent on the internal bias of the emitting junction. A more in depth investigation would model this dependence on bias and provide a greater resemblance to measured data.

Series resistance has not been considered here at the practical limit, as it does not affect the radiative recombination emission, as that is dependent on the internal bias in each junction. In MJSCs where series resistance play a large role, the enhancement due to radiative coupling may become even more pronounced.

Optimal band gaps identified from a previous section, state-of-the-art and future expected band MJSC band gaps have been investigated here. Further analysis would examine the effect of radiative coupling on the selection of optimal band gaps, and validate the statement by Brown and Green [256], using real atmospheric data, that a solar cell optimised to perform at a high air mass has greater spectral robustness across the entire range of spectral conditions.

This chapter contains the first analysis of the enhancement due to radiative coupling that can be expected from a solar cell with realistic material quality under realistic atmospheric conditions, providing cell and system designers with a practical limit. It will assist in the design of future solar cells, which due to the increased spectral sensitivity, are expected to benefit from radiative coupling.

8 Conclusions

In this thesis, a prediction technique and computer model incorporating advanced radiative transfer modelling has been developed to accurately predict energy yields from concentrator photovoltaic systems, by estimating the solar spectrum from measured atmospheric parameters. In the validation undertaken here, agreement to within 2% was noted between the measured and modelled energy yield over an annual period for a deployed system in Toyohashi, Japan. In addition, air mass, aerosols and precipitable water are shown to be the atmospheric parameters with the greatest impact on CPV system efficiency.

The impact of individual atmospheric parameters on device power and energy yield have been assessed using the validated model for multiple locations around the world where CPV can expect to be deployed. Aerosols have been shown to have substantial impact on energy yields in most areas - in certain cases, the impact of aerosols is comparable to or greater than that of air mass. It is demonstrated that understanding of the atmospheric conditions are crucial and cannot be neglected if accurate estimates of energy production and cost of energy are to be made.

The optimal band gaps for multijunction solar cells, accounting for realistic material quality, have been calculated. Large variations between the theoretical optimum and the practical optimum are shown, on the order of 100s of milli-electron-volts. This has implications for design of next generation multijunction solar cells and road maps for achieving higher conversion efficiency, allowing for more accurate predictions for achievable performance.

In the first analysis of its kind, the performance enhancement available from radiative coupling between junctions has been calculated for state-of-the-art and future optimal multijunction solar cell designs under a range of spectral conditions for devices with material quality. Currently, devices operating in the field can expect an enhancement of below 1% in annual energy yield due to the effect. Next generation devices, using four or more junctions, can expect enhancement of up to 5%. Future designs with additional junctions can expect to benefit from greater enhancement due to the radiative coupling effect. This has important ramifications for solar cell designers who wish to maximise their product's energy production for a given location.

9 Acknowledgements

The author would like to gratefully acknowledge a studentship from the Grantham Institute for Climate Change, without which this project would not have been possible; the invaluable guidance of his supervisors and constructive criticism offered at all stages; the staff and students of the Quantum Photovoltaics Group at Imperial College London, which made for an excellent supportive environment in which ideas can develop, tested and argued; collaborators and coauthors on publications and members of the community for the myriad of interesting conversations and making this journey so fulfilling; friends, for being there; and his family, for their tireless effort over the years.

Bibliography

[1] V. Smil, *Energy In World History.* Essays in World History Series, Perseus Books Group, 1994.

[2] Department of Economic and Social Affairs - Population Division, "World population to 2300," tech. rep., United Nations, 2004.

[3] World Bank, "World population growth," tech. rep., 2004.

[4] Intergovernmental Panel on Climate Change, *Fourth Assessment Report: Climate Change 2007: Working Group III Report: Mitigation of Climate Change.* Geneva: IPCC, 2007.

[5] International Energy Agency, "Key world energy statistics," tech. rep., 2012.

[6] International Energy Agency, "International energy agency - statistics, electricity/heat in world in 2009." Accessed on, January 2013.

[7] Intergovernmental Panel on Climate Change, *Fourth Assessment Report: Climate Change 2007: The AR4 Synthesis Report.* Geneva: IPCC, 2007.

[8] R. J. Stouffer, S. Manabe, and K. Y. Vinnikov, "Model assessment of the role of natural variability in recent global warming," *Nature*, vol. 367, pp. 634–646, 1994.

[9] M. Parry and I. P. on Climate Change. Working Group I., *Climate Change 2007: Impacts, Adaptation and Vulnerability : Working Group I Contribution to the Fourth Assessment Report of the IPCC.* Climate Change 2007, Cambridge University Press, 2007.

[10] B. Metz, O. Davidson, H. de Coninck, M. Loos, and L. Meyer, *IPCC special report on carbon dioxide capture and storage.* Other Informa-

tion: IEACR LIB 700, 2005. (eds.) Other Information: IEACR LIB 700.

[11] R. S. Haszeldine, “Carbon capture and storage: How green can black be?,” *Science*, vol. 325, no. 5948, pp. 1647–1652, 2009.

[12] X. Lu, M. B. McElroy, and J. Kiviluoma, “Global potential for wind-generated electricity,” *Proceedings of the National Academy of Sciences*, vol. 106, no. 27, pp. 10933–10938, 2009.

[13] Intergovernmental Panel on Climate Change, *IPCC Special Report on Renewable Energy Sources and Climate Change Mitigation.* Cambridge University Press, 2011.

[14] C. Breyer and G. Knies, “Global energy supply potential of concentrating solar power,”

[15] S. A. Kalogirou, “Solar thermal collectors and applications,” *Progress in energy and combustion science*, vol. 30, no. 3, pp. 231–295, 2004.

[16] H. Müller-Steinhagen and F. Trieb, “Concentrating solar power,” *References Industrial Engineering*, 2004.

[17] J. Han, A. P. Mol, and Y. Lu, “Solar water heaters in China: A new day dawning,” *Energy Policy*, vol. 38, no. 1, pp. 383 – 391, 2010.

[18] W. Li, T. H. Rubin, and P. A. Onyina, “Comparing solar water heater popularization policies in China, Israel and Australia: The roles of governments in adopting green innovations,” *Sustainable Development*, pp. n/a–n/a, 2012.

[19] D. Mills, “Advances in solar thermal electricity technology,” *Solar Energy*, vol. 76, no. 1-3, pp. 19 – 31, 2004.

[20] International Energy Agency, “Technology roadmap, concentrating solar power,” tech. rep., 2010.

[21] A.-E. Becquerel, “Memoire sur les effets electriques produits sous l’influence des rayons solaires,” *Compt. Rend. Acad. Sci.*, vol. 9, p. 561, 1839.

[22] R. E. Day and W. G. Adams, “The action of light on selenium,” *Proceedings of the Royal Society*, vol. A25, pp. 113–117, 1876.

[23] C. E. Fritts, “On a new form of selenium photocell,” *American Journal of Science*, vol. 26, p. 465, 1883.

[24] D. M. Chapin, C. S. Fuller, and G. L. Pearson, “A new silicon p-n junction photocell for converting solar radiation into electrical power,” *Journal of Applied Physics*, vol. 25, no. 5, pp. 676–677, 1954.

[25] J. Zhao, A. Wang, M. A. Green, and F. Ferrazza, “19.8% efficient honeycomb textured multicrystalline and 24.4% monocrystalline silicon solar cells,” *Applied Physics Letters*, vol. 73, pp. 1991 –1993, oct 1998.

[26] L. Partain and L. Fraas, *Solar Cell Electricity Market History, Public Policy, Projected Future, and Estimated Costs*, pp. 17–42. John Wiley & Sons, Inc., 2010.

[27] L. Rubin, *Crystalline Silicon Solar Cells and Modules*, pp. 111–136. John Wiley & Sons, Inc., 2010.

[28] National Renewable Energy Agency, “2010 Solar Technologies Market Report, November 2011, Energy Efficiency & Renewable Energy (EERE),” Dec. 2011.

[29] W. Shockley and H. J. Queisser, “Detailed balance limit of efficiency of p-n junction solar cells,” *Journal of Applied Physics*, vol. 32, no. 3, pp. 510–519, 1961.

[30] A. Feltrin and A. Freundlich, “Material considerations for terawatt level deployment of photovoltaics,” *Renewable Energy*, vol. 33, no. 2, pp. 180 – 185, 2008. E-MRS 2006 Symposium M: Materials, Devices and Prospects for Sustainable Energy, 2006 Spring Meeting of the European Materials Research Society.

[31] N. S. Fatemi, H. Pollard, H. Q. Hou, and P. Sharps, “Solar array trades between very high-efficiency multi-junction and Si space solar cells,” in *Photovoltaic Specialists Conference, 2000. Conference Record of the Twenty-Eighth IEEE*, pp. 1083–1086, 2000.

[32] P. Iles, “Evolution of space solar cells,” *Solar Energy Materials and Solar Cells*, vol. 68, no. 1, pp. 1 – 13, 2001. Solar cells in space.

[33] T. Takamoto, T. Agui, H. Washio, N. Takahashi, K. Nakamura, O. Anzawa, M. Kaneiwa, K. Kamimura, K. Okamoto, and M. Yamaguchi, “Future development of InGaP/(In)GaAs based multijunction solar cells,” in *Photovoltaic Specialists Conference, 2005. Conference Record of the Thirty-first IEEE*, pp. 519–524, 2005.

[34] B. Kayes, H. Nie, R. Twist, S. Spruytte, F. Reinhardt, I. Kizilyalli, and G. Higashi, “27.6% conversion efficiency, a new record for single-junction solar cells under 1 sun illumination,” in *Photovoltaic Specialists Conference (PVSC), 2011 37th IEEE*, pp. 4–8, June 2011.

[35] K. L. Chopra, P. D. Paulson, and V. Dutta, “Thin-film solar cells: an overview,” *Progress in Photovoltaics: Research and Applications*, vol. 12, no. 2-3, pp. 69–92, 2004.

[36] A. Shah, P. Torres, R. Tscharner, N. Wyrsch, and H. Keppner, “Photovoltaic technology: The case for thin-film solar cells,” *Science*, vol. 285, no. 5428, pp. 692–698, 1999.

[37] D. Cusano, “CdTe solar cells and photovoltaic heterojunctions in II-VI compounds,” *Solid-State Electronics*, vol. 6, no. 3, pp. 217 – 218, 1963.

[38] K. Ramanathan, M. A. Contreras, C. L. Perkins, S. Asher, F. S. Hasoon, J. Keane, D. Young, M. Romero, W. Metzger, R. Noufi, J. Ward, and A. Duda, “Properties of 19.2% efficiency ZnO/CdS/CuInGaSe2 thin-film solar cells,” *Progress in Photovoltaics: Research and Applications*, vol. 11, no. 4, pp. 225–230, 2003.

[39] J. Nelson, “Organic photovoltaic films,” *Current Opinion in Solid State and Materials Science*, vol. 6, no. 1, pp. 87 – 95, 2002.

[40] B. O’Regan and M. Graetzel, “A low-cost, high-efficiency solar cell based on dye-sensitized colloidal TiO2 films,” *Nature*, vol. 353, pp. 737–740, Oct. 1991.

[41] M. O. Reese, A. J. Morfa, M. S. White, N. Kopidakis, S. E. Shaheen, G. Rumbles, and D. S. Ginley, "Pathways for the degradation of organic photovoltaic P3HT:PCBM based devices," *Solar Energy Materials and Solar Cells*, vol. 92, no. 7, pp. 746 – 752, 2008. Degradation and Stability of Polymer and Organic Solar Cells.

[42] F. C. Krebs and K. Norrman, "Analysis of the failure mechanism for a stable organic photovoltaic during 10 000h of testing," *Progress in Photovoltaics: Research and Applications*, vol. 15, no. 8, pp. 697–712, 2007.

[43] L. C. Hirst and N. J. Ekins-Daukes, "Fundamental losses in solar cells," *Progress in Photovoltaics: Research and Applications*, vol. 19, no. 3, pp. 286–293, 2011.

[44] C. A. Gueymard, "The sun's total and spectral irradiance for solar energy applications and solar radiation models," *Solar Energy*, vol. 76, no. 4, pp. 423 – 453, 2004.

[45] A. Beer, "Bestimmung der absorption des rothen lichts in farbigen flüssigkeiten," *Annalen der Physik und Chemie*, vol. 86, pp. 78–88, 1852.

[46] C. A. Gueymard, "Parameterized transmittance model for direct beam and circumsolar spectral irradiance," *Solar Energy*, vol. 71, no. 5, pp. 325–346, 2001.

[47] K. Liou, *Radiation and cloud processes in the atmosphere. Theory, observation, and modeling.* Oxford University Press, 1992.

[48] American Society for Testing and Materials, "E490-00a(2006) standard solar constant and zero air mass solar spectral irradiance tables." Accessed on, February 2013.

[49] G. L. Schuster, O. Dubovik, and B. N. Holben, "Angstrom exponent and bimodal aerosol size distributions," *Journal of Geophysical Research: Atmospheres*, vol. 111, no. D7, 2006.

[50] P. B. Russell, R. W. Bergstrom, Y. Shinozuka, A. D. Clarke, P. F. DeCarlo, J. L. Jimenez, J. M. Livingston, J. Redemann, O. Dubovik,

and A. Strawa, “Absorption angstrom exponent in aeronet and related data as an indicator of aerosol composition,” *Atmospheric Chemistry and Physics*, vol. 10, no. 3, pp. 1155–1169, 2010.

[51] C. A. Gueymard, “Daily spectral effects on concentrating pv solar cells as affected by realistic aerosol optical depth and other atmospheric conditions,” pp. 741007–741007–14, 2009.

[52] D. M. Gates, “Infrared determination of precipitable water vapor in a vertical column of the earth’s atmosphere,” *Journal of Meteorology*, vol. 13, pp. 369–375, 1956.

[53] D. Daumont, J. Brion, J. Charbonnier, and J. Malicet, “Ozone UV spectroscopy I: Absorption cross-sections at room temperature,” *Journal of Atmospheric Chemistry*, vol. 15, pp. 145–155, 1992.

[54] J. A. Davidson, C. A. Cantrell, A. H. McDaniel, R. E. Shetter, S. Madronich, and J. G. Calvert, “Visible-ultraviolet absorption cross sections for NO2 as a function of temperature,” *Journal of Geophysical Research: Atmospheres*, vol. 93, no. D6, pp. 7105–7112, 1988.

[55] W. SCHNEIDER, G. MOORTGAT, G. TYNDALL, and J. BURROWS, “Absorption cross-sections of NO2 in the UV and visible region (200-700 nm) at 298 K,” *Journal of Photochemistry and Photobiology A-chemistry*, vol. 40, pp. 195–217, 1987.

[56] N. Ekins-Daukes, J. Barnes, K. Barnham, J. Connolly, M. Mazzer, J. Clark, R. Grey, G. Hill, M. Pate, and J. Roberts, “Strained and strain-balanced quantum well devices for high-efficiency tandem solar cells,” *Solar Energy Materials and Solar Cells*, vol. 68, no. 1, pp. 71 – 87, 2001.

[57] J. Nelson, *The Physics of Solar Cells.* Imperial College Press, 2003.

[58] C. H. Henry, “Limiting efficiencies of ideal single and multiple energy gap terrestrial solar cells,” *Journal of Applied Physics*, vol. 51, no. 8, pp. 4494–4500, 1980.

[59] A. D. Vos, “Detailed balance limit of the efficiency of tandem solar cells,” *Journal of Physics D: Applied Physics*, vol. 13, no. 5, p. 839, 1980.

[60] N. Chan, N. Ekins-Daukes, J. Adams, M. Lumb, M. Gonzalez, P. Jenkins, I. Vurgaftman, J. Meyer, and R. Walters, "Optimal bandgap combinations - does material quality matter?," *Photovoltaics, IEEE Journal of*, vol. 2, pp. 202 –208, april 2012.

[61] T. Takamoto, E. Ikeda, T. Agui, H. Kurita, T. Tanabe, S. Tanaka, H. Matsubara, Y. Mine, S. Takagishi, and M. Yamaguchi, "Ingap / gaas and ingaas mechanically-stacked triple-junction solar cells," in *Photovoltaic Specialists Conference, 1997., Conference Record of the Twenty-Sixth IEEE*, pp. 1031 –1034, sep-3 oct 1997.

[62] J. M. Zahler, F. Morral, C.-G. Ahn, H. A. Atwater, M. W. Wanlass, C. Chu, and P. A. Iles, "Wafer bonding and layer transfer processes for high efficiency solar cells," in *NCPV and Solar Program Review Meeting*, vol. 723, 2003.

[63] D. Law, D. Bhusari, S. Mesropian, J. C. Boisvert, W. Hong, A. Boca, D. C. Larrabee, C. Fetzer, R. King, and N. H. Karam, "Semiconductor-bonded III-V multijunction space solar cells," in *Photovoltaic Specialists Conference (PVSC), 2009 34th IEEE*, pp. 002237–002239, 2009.

[64] M. A. Green and A. Ho-Baillie, "Forty three per cent composite split-spectrum concentrator solar cell efficiency," *Progress in Photovoltaics: Research and Applications*, vol. 18, no. 1, pp. 42–47, 2010.

[65] A. Barnett, D. Kirkpatrick, C. Honsberg, D. Moore, M. Wanlass, K. Emery, R. Schwartz, D. Carlson, S. Bowden, D. Aiken, A. Gray, S. Kurtz, L. Kazmerski, M. Steiner, J. Gray, T. Davenport, R. Buelow, L. Takacs, N. Shatz, J. Bortz, O. Jani, K. Goossen, F. Kiamilev, A. Doolittle, I. Ferguson, B. Unger, G. Schmidt, E. Christensen, and D. Salzman, "Very high efficiency solar cell modules," *Progress in Photovoltaics: Research and Applications*, vol. 17, no. 1, pp. 75–83, 2009.

[66] G. Flamand and J. Poortmans, "Towards highly efficient 4-terminal mechanical photovoltaic stacks," *III-Vs Review*, vol. 19, no. 7, pp. 24 – 27, 2006.

[67] S. R. Kurtz, P. Faine, and J. M. Olson, “Modeling of two-junction, series-connected tandem solar cells using top-cell thickness as an adjustable parameter,” *Journal of Applied Physics*, vol. 68, no. 4, pp. 1890–1895, 1990.

[68] S. Bedair, M. Lamorte, J. Hauser, and K. Mitchell, “Growth and characterization of a two-junction, stacked solar cell,” in *Electron Devices Meeting, 1978 International*, vol. 24, pp. 250 – 253, 1978.

[69] B. Chung, G. F. Virshup, and J. G. Werthen, “High efficiency, one sun (22.3% at air mass 0; 23.9% at air mass 1.5) monolithic two junction cascade solar cell grown by metalorganic vapor phase epitaxy,” *Applied Physics Letters*, vol. 52, pp. 1889 –1891, may 1988.

[70] J. Gee and G. Virshup, “A 31%-efficient GaAs/Silicon mechanically stacked, multijunction concentrator solar cell,” in *Photovoltaic Specialists Conference, 1988., Conference Record of the Twentieth IEEE*, pp. 754 –758 vol.1, 1988.

[71] J. Yang, R. Ross, T. Glatfelter, R. Mohr, G. Hammond, C. Bernotaitis, E. Chen, J. Burdick, M. Hopson, and S. Guha, “High efficiency multi-junction solar cells using amorphous silicon and amorphous silicon-germanium alloys,” in *Photovoltaic Specialists Conference, 1988., Conference Record of the Twentieth IEEE*, pp. 241 –246 vol.1, sept. 1988.

[72] J. M. Olson, S. R. Kurtz, A. E. Kibbler, and P. Faine, “A 27.3% efficient $\mathrm{Ga_{0.5}In_{0.5}P/GaAs}$ tandem solar cell,” *Applied Physics Letters*, vol. 56, no. 7, pp. 623–625, 1990.

[73] M. A. Green, K. Emery, Y. Hishikawa, W. Warta, and E. D. Dunlop, “Solar cell efficiency tables (version 40),” *Progress in Photovoltaics: Research and Applications*, vol. 20, no. 5, pp. 606–614, 2012.

[74] R. Jones, P. Hebert, P. Pien, R. King, D. Bhusari, R. Brandt, O. Al Taher, C. Fetzer, J. Ermer, A. Boca, D. Larrabee, X. Liu, and N. Karam, “Status of 40% production efficiency concentrator cells at Spectrolab,” in *Photovoltaic Specialists Conference (PVSC), 2010 35th IEEE*, pp. 000189 –000195, june 2010.

[75] J. Ermer, R. Jones, P. Hebert, P. Pien, R. King, D. Bhusari, R. Brandt, O. Al-Taher, C. Fetzer, G. Kinsey, and N. Karam, "Status of C3MJ and C4MJ production concentrator solar cells at Spectrolab," *Photovoltaics, IEEE Journal of*, vol. 2, pp. 209 –213, april 2012.

[76] W. Guter, J. Schone, S. P. Philipps, M. Steiner, G. Siefer, A. Wekkeli, E. Welser, E. Oliva, A. W. Bett, and F. Dimroth, "Current-matched triple-junction solar cell reaching 41.1% conversion efficiency under concentrated sunlight," *Applied Physics Letters*, vol. 94, pp. 223504 –223504–3, jun 2009.

[77] R. R. King, D. C. Law, K. M. Edmondson, C. M. Fetzer, G. S. Kinsey, H. Yoon, R. A. Sherif, and N. H. Karam, "40% efficient metamorphic GaInP/GaInAs/Ge multijunction solar cells," *Applied Physics Letters*, vol. 90, no. 18, p. 183516, 2007.

[78] T. Takamoto, T. Agui, A. Yoshida, K. Nakaido, H. Juso, K. Sasaki, K. Nakamora, H. Yamaguchi, T. Kodama, H. Washio, M. Imaizumi, and M. Takahashi, "World's highest efficiency triple-junction solar cells fabricated by inverted layers transfer process," in *Photovoltaic Specialists Conference (PVSC), 2010 35th IEEE*, pp. 000412 –000417, june 2010.

[79] J. F. Geisz, S. Kurtz, M. W. Wanlass, J. S. Ward, A. Duda, D. J. Friedman, J. M. Olson, W. E. McMahon, T. E. Moriarty, and J. T. Kiehl, "High-efficiency GaInP/GaAs/InGaAs triple-junction solar cells grown inverted with a metamorphic bottom junction," *Applied Physics Letters*, vol. 91, no. 2, p. 023502, 2007.

[80] K. Barnham, I. Ballard, J. Connolly, N. Ekins-Daukes, B. Kluftinger, J. Nelson, and C. Rohr, "Quantum well solar cells," *Physica E: Low-dimensional Systems and Nanostructures*, vol. 14, no. 1-2, pp. 27 – 36, 2002.

[81] K. Barnham, I. Ballard, J. Barnes, J. Connolly, P. Griffin, B. Kluftinger, J. Nelson, E. Tsui, and A. Zachariou, "Quantum well solar cells," *Applied Surface Science*, vol. 113-114, no. 0, pp. 722 – 733, 1997. Proceedings of the Eighth International Conference on Solid Films and Surfaces.

[82] N. J. Ekins-Daukes, K. W. J. Barnham, J. P. Connolly, J. S. Roberts, J. C. Clark, G. Hill, and M. Mazzer, “Strain-balanced GaAsP/InGaAs quantum well solar cells,” *Applied Physics Letters*, vol. 75, pp. 4195 –4197, dec 1999.

[83] N. Ekins-Daukes, J. Barnes, K. Barnham, J. Connolly, M. Mazzer, J. Clark, R. Grey, G. Hill, M. Pate, and J. Roberts, “Strained and strain-balanced quantum well devices for high-efficiency tandem solar cells,” *Solar Energy Materials and Solar Cells*, vol. 68, no. 1, pp. 71 – 87, 2001.

[84] M. Mazzer, K. Barnham, I. Ballard, A. Bessiere, A. Ioannides, D. Johnson, M. Lynch, T. Tibbits, J. Roberts, G. Hill, and C. Calder, “Progress in quantum well solar cells,” *Thin Solid Films*, vol. 511-512, no. 0, pp. 76 – 83, 2006.

[85] A. Nozik, “Quantum dot solar cells,” *Physica E: Low-dimensional Systems and Nanostructures*, vol. 14, no. 1-2, pp. 115 – 120, 2002.

[86] C. G. Bailey, D. V. Forbes, R. P. Raffaelle, and S. M. Hubbard, “Near 1 v open circuit voltage InAs/GaAs quantum dot solar cells,” *Applied Physics Letters*, vol. 98, no. 16, p. 163105, 2011.

[87] B. Kayes, H. Nie, R. Twist, S. Spruytte, F. Reinhardt, I. Kizilyalli, and G. Higashi, “27.6% conversion efficiency, a new record for single-junction solar cells under 1 sun illumination,” in *Photovoltaic Specialists Conference (PVSC), 2011 37th IEEE*, pp. 000004 –000008, june 2011.

[88] S. Burroughs, R. Conner, B. Furman, E. Menard, A. Gray, M. Meitl, S. Bonafede, D. Kneeburg, K. Ghosal, R. Bukovnik, W. Wagner, S. Seel, and M. Sullivan, “A new approach for a low cost CPV module design utilizing micro-transfer printing technology,” *AIP Conference Proceedings*, vol. 1277, no. 1, pp. 163–166, 2010.

[89] A. Gombert, S. Wanka, E. Gerster, S. van Riesen, M. Neubauer, G. Lange, A. Hamidi, T. Burke, J. Stor, W. Aipperspach, C. Taliercio, L. Mader, A. Valli, M. Ziegler, S. Hepp, I. Heile, T. Gerstmaier, and K.-F. Haarburger, “From a 32 m^2 system with 90 CPV modules

to a 105 m^2 system with 12 cpv modules - Soitec's new CPV system CX-S530," *AIP Conference Proceedings*, vol. 1477, no. 1, pp. 200–203, 2012.

[90] K. Araki, H. Uozumi, T. Egami, M. Hiramatsu, Y. Miyazaki, Y. Kemmoku, A. Akisawa, N. J. Ekins-Daukes, H. S. Lee, and M. Yamaguchi, "Development of concentrator modules with dome-shaped fresnel lenses and triple-junction concentrator cells," *Progress in Photovoltaics: Research and Applications*, vol. 13, no. 6, pp. 513–527, 2005.

[91] P. Verlinden, A. Lewandowski, C. Bingham, G. Kinsey, R. Sherif, and J. Lasich, "Performance and reliability of multijunction III-V modules for concentrator dish and central receiver applications," in *Photovoltaic Energy Conversion, Conference Record of the 2006 IEEE 4th World Conference on*, vol. 1, pp. 592 –597, may 2006.

[92] K. Araki, T. Yano, and Y. Kuroda, "30 kw concentrator photovoltaic system using dome-shaped fresnel lenses," *Opt. Express*, vol. 18, pp. A53–A63, Apr 2010.

[93] P. Zamora, P. Benitez, Y. Li, J. C. Minano, J. Mendes-Lopes, and K. Araki, "The dome-shaped Fresnel-Köhler concentrator," *AIP Conference Proceedings*, vol. 1477, no. 1, pp. 69–72, 2012.

[94] J. M. Gordon, "Aplanatic optics for solar concentration," *Opt. Express*, vol. 18, pp. A41–A52, Apr 2010.

[95] P. Espinet-Gonzalez, R. Mohedano, I. Garcia, P. Zamora, I. Rey-Stolle, P. Benitez, C. Algora, A. Cvetkovic, M. Hernandez, J. Chaves, J. C. Minano, and Y. Li, "Triple-junction solar cell performance under fresnel-based concentrators taking into account chromatic aberration and off-axis operation," *AIP Conference Proceedings*, vol. 1477, no. 1, pp. 81–84, 2012.

[96] T. Hornung, A. Bachmaier, P. Nitz, and A. Gombert, "Temperature dependent measurement and simulation of fresnel lenses for concentrating photovoltaics," *AIP Conference Proceedings*, vol. 1277, no. 1, pp. 85–88, 2010.

[97] D. C. Miller, M. D. Kempe, C. E. Kennedy, and S. R. Kurtz, “Analysis of transmitted optical spectrum enabling accelerated testing of CPV designs,” pp. 74070G–74070G–12, 2009.

[98] T. Hornung, A. Bachmaier, P. Nitz, and A. Gombert, “Temperature and wavelength dependent measurement and simulation of fresnel lenses for concentrating photovoltaics,” pp. 77250A–77250A–6, 2010.

[99] R. French, J. Rodriguez-Parada, M. Yang, R. Derryberry, and N. Pfeiffenberger, “Optical properties of polymeric materials for concentrator photovoltaic systems,” *Solar Energy Materials and Solar Cells*, vol. 95, no. 8, pp. 2077 – 2086, 2011. Solar Energy Materials and Thin Films.

[100] T. Hornung, M. Steiner, and P. Nitz, “Estimation of the influence of fresnel lens temperature on energy generation of a concentrator photovoltaic system,” *Solar Energy Materials and Solar Cells*, vol. 99, no. 0, pp. 333 – 338, 2012. 9th International Meeting on Electrochromism.

[101] R. Lockenhoff, T. Kubera, and K. D. Rasch, “Water cooled TJ dense array modules for parabolic dishes,” *AIP Conference Proceedings*, vol. 1277, no. 1, pp. 43–46, 2010.

[102] P. Verlinden, A. Lewandowski, H. Kendall, S. Carter, K. Cheah, I. Varfolomeev, D. Watts, M. Volk, I. Thomas, P. Wakeman, A. Neumann, P. Gizinski, D. Modra, D. Turner, and J. Lasich, “Update on two-year performance of 120 kWp concentrator PV systems using multi-junction III-V solar cells and parabolic dish reflective optics,” in *Photovoltaic Specialists Conference, 2008. PVSC ’08. 33rd IEEE*, pp. 1–6, 2008.

[103] H. Chayet, I. Lozovsky, O. Kost, R. Loeckenhoff, and K.-D. Rasch, “High efficiency, low cost parabolic dish system for cogeneration of electricity and heat,” *AIP Conference Proceedings*, vol. 1277, no. 1, pp. 175–178, 2010.

[104] G. Mittelman, A. Kribus, and A. Dayan, “Solar cooling with concentrating photovoltaic/thermal (CPVT) systems,” *Energy Conversion and Management*, vol. 48, no. 9, pp. 2481 – 2490, 2007.

[105] G. Mittelman, A. Kribus, O. Mouchtar, and A. Dayan, "Water desalination with concentrating photovoltaic/thermal (CPVT) systems," *Solar Energy*, vol. 83, no. 8, pp. 1322 – 1334, 2009.

[106] International Electrotechnical Commission, "IEC 62670-1 Ed.1: Concentrator photovoltaic (CPV) module and assembly performance testing and energy rating - Part 1: Performance measurements and power rating - irradiance and temperature," 2011.

[107] S. Kurtz, M. Muller, B. Marion, K. Emery, R. McConnell, S. Surendran, and A. Kimber, "Considerations for how to rate CPV," tech. rep., National Renewable Energy Laboratory, 2010.

[108] S. Surendran, "CPV standard conditions." Accessed on, February 2013.

[109] W. Nishikawa and S. Horne, "Key advantages of concentrating photovoltaics (CPV) for lowering levelized cost of electricity (LCOE)," in *European Photovoltaics Solar Energy Conference*, 2008.

[110] B. Prior, "Cost and LCOE by generation technology, 2009-2020," tech. rep., GreenTechMedia Research, 2011.

[111] V. M. Fthenakis and H. C. Kim, "Life cycle assessment of high-concentration photovoltaic systems," *Progress in Photovoltaics: Research and Applications*, pp. n/a–n/a, 2012.

[112] V. M. Fthenakis, H. C. Kim, and E. Alsema, "Emissions from photovoltaic life cycles," *Environmental Science and Technology*, vol. 42, no. 6, pp. 2168–2174, 2008. PMID: 18409654.

[113] H. C. Kim, V. Fthenakis, J.-K. Choi, and D. E. Turney, "Life cycle greenhouse gas emissions of thin-film photovoltaic electricity generation," *Journal of Industrial Ecology*, vol. 16, pp. S110–S121, 2012.

[114] G. A. Heath and M. K. Mann, "Background and reflections on the life cycle assessment harmonization project," *Journal of Industrial Ecology*, vol. 16, pp. S8–S11, 2012.

[115] M. Whitaker, G. A. Heath, P. O'Donoughue, and M. Vorum, "Life cycle greenhouse gas emissions of coal-fired electricity generation," *Journal of Industrial Ecology*, vol. 16, pp. S53–S72, 2012.

[116] S. Kurtz, D. Myers, W. E. McMahon, J. Geisz, and M. Steiner, "A comparison of theoretical efficiencies of multi-junction concentrator solar cells," *Progress in Photovoltaics: Research and Applications*, vol. 16, no. 6, pp. 537–546, 2008.

[117] D. Aiken, I. Aeby, B. Clevenger, F. Newman, P. Patel, P. Sharps, M. Stan, T. Varghese, and J. Wood, "Concentrator solar cell production capability and laboratory results at emcore," *AIP Conference Proceedings*, vol. 1277, no. 1, pp. 7–10, 2010.

[118] A. Cornfeld, D. Aiken, B. Cho, A. Ley, P. Sharps, M. Stan, and T. Varghese, "Development of a four sub-cell inverted metamorphic multi-junction (IMM) highly efficient AM0 solar cell," in *Photovoltaic Specialists Conference (PVSC), 2010 35th IEEE*, pp. 000105 –000109, june 2010.

[119] D. Derkacs, D. Bilir, and V. Sabnis, "Luminescent coupling in GaAs/GaInNAsSb multijunction solar cells," *Photovoltaics, IEEE Journal of*, vol. 3, pp. 520 –527, January 2013.

[120] J. Adams, V. Elarde, A. Hains, C. Stender, F. Tuminello, C. Youtsey, A. Wibowo, and M. Osowski, "Demonstration of multiple substrate reuses for inverted metamorphic solar cells," in *Photovoltaic Specialists Conference (PVSC), 2012 38th IEEE*, June 2011.

[121] C. Keavney, V. Haven, and S. Vernon, "Emitter structures in MOCVD InP solar cells," in *Photovoltaic Specialists Conference, 1990., Conference Record of the Twenty First IEEE*, pp. 141 –144 vol.1, may 1990.

[122] R. Walters, M. Gonzalez, J. Tischler, M. Lumb, J. Meyer, I. Vurgaftman, J. Abell, M. Yakes, N. Ekins-Daukes, J. Adams, N. Chan, P. Stavrinou, and P. Jenkins, "Design of an achievable, all lattice-matched multijunction solar cell using InGaAlAsSb," in *Photovoltaic Specialists Conference (PVSC), 2011 37th IEEE*, pp. 000122 –000126, june 2011.

[123] M. S. Leite, R. L. Woo, W. D. Hong, D. C. Law, and H. A. Atwater, “Wide-band-gap InAlAs solar cell for an alternative multijunction approach,” *Applied Physics Letters*, vol. 98, no. 9, p. 093502, 2011.

[124] K. W. J. Barnham and G. Duggan, “A new approach to high efficiency multi bandgap solar cells,” *Journal of Applied Physics*, vol. 67, pp. 3490 –3493, apr 1990.

[125] A. Nozik, “Quantum dot solar cells,” *Physica E: Low-dimensional Systems and Nanostructures*, vol. 14, no. 12, pp. 115 – 120, 2002.

[126] M. Yamaguchi, K.-I. Nishimura, T. Sasaki, H. Suzuki, K. Arafune, N. Kojima, Y. Ohsita, Y. Okada, A. Yamamoto, T. Takamoto, and K. Araki, “Novel materials for high-efficiency III-V multi-junction solar cells,” *Solar Energy*, vol. 82, no. 2, pp. 173 – 180, 2008.

[127] R. Oshima, A. Takata, and Y. Okada, “Strain-compensated InAs/GaNAs quantum dots for use in high-efficiency solar cells,” *Applied Physics Letters*, vol. 93, no. 8, p. 083111, 2008.

[128] H. A. Atwater and A. Polman, “Plasmonics for improved photovoltaic devices,” *Nature Materials*, vol. 9, p. 205213, 2010.

[129] A. Polman, “Plasmonics applied,” *Science*, vol. 322, no. 5903, pp. 868–869, 2008.

[130] S. Mokkapati and K. R. Catchpole, “Nanophotonic light trapping in solar cells,” *Journal of Applied Physics*, vol. 112, no. 10, p. 101101, 2012.

[131] V. Giannini, A. I. Fernandez-Dominguez, S. C. Heck, and S. A. Maier, “Plasmonic nanoantennas: Fundamentals and their use in controlling the radiative properties of nanoemitters,” *Chemical Reviews*, vol. 111, no. 6, pp. 3888–3912, 2011.

[132] G. Kosmadakis, D. Manolakos, and G. Papadakis, “Simulation and economic analysis of a CPV/thermal system coupled with an organic Rankine cycle for increased power generation,” *Solar Energy*, vol. 85, no. 2, pp. 308 – 324, 2011.

[133] A. Kribus, D. Kaftori, G. Mittelman, A. Hirshfeld, Y. Flitsanov, and A. Dayan, "A miniature concentrating photovoltaic and thermal system," *Energy Conversion and Management*, vol. 47, no. 20, pp. 3582 – 3590, 2006. Heat Transfer in Components and Systems for Sustainable Energy Technologies: Heat-SET 2005, 5-7 April 2005, Grenoble, France.

[134] G. Barbose, N. Darghouth, and R. Wiser, "Tracking the sun V: An historical summary of the installed price of photovoltaics in the United States from 1998 to 2011," tech. rep., Lawrence Berkeley National Laboratory, November 2012.

[135] M. Woodhouse, A. Goodrich, R. Margolis, T. James, R. Dhere, T. Gessert, T. Barnes, R. Eggert, and D. Albin, "Perspectives on the pathways for cadmium telluride photovoltaic module manufacturers to address expected increases in the price for tellurium," *Solar Energy Materials and Solar Cells*, no. 0, 2012.

[136] R. McConnell, V. Garboushian, J. Brown, C. Crawford, K. Darban, D. Dutra, S. Geer, V. Ghassemian, R. Gordon, G. Kinsey, K. Stone, and G. Turner, "Assuring long-term reliability of concentrator PV systems," pp. 741208–741208–5, 2009.

[137] N. Bosco, C. Sweet, and S. Kurtz, "Reliability testing the die-attach of CPV cell assemblies," in *Photovoltaic Specialists Conference (PVSC), 34th IEEE*, pp. 000917–000922, 2009.

[138] J. Gonzalez, M. Vazquez, C. Algora, and N. Nunez, "Real-time reliability test for a CPV module based on a power degradation model," *Progress in Photovoltaics: Research and Applications*, vol. 19, no. 1, pp. 113–122, 2011.

[139] E. Gerster, A. Gombert, and S. Wanka, "Reliability of Concentrix CPV modules," *AIP Conference Proceedings*, vol. 1477, no. 1, pp. 294–296, 2012.

[140] B. Depuydt, E. Bergman, V. Khorenko, R. Leutz, J. Melia, and A. Hoflich, "Scalability of CPV towards multi-gigawatt deployment," *AIP Conference Proceedings*, vol. 1477, no. 1, pp. 376–382, 2012.

[141] C. Candelise, M. Winskel, and R. Gross, "Implications for cdte and cigs technologies production costs of indium and tellurium scarcity," *Progress in Photovoltaics: Research and Applications*, vol. 20, no. 6, pp. 816–831, 2012.

[142] R. Mueller, K. Dagestad, P. Ineichen, M. Schroedter-Homscheidt, S. Cros, D. Dumortier, R. Kuhlemann, J. Olseth, G. Piernavieja, C. Reise, L. Wald, and D. Heinemann, "Rethinking satellite-based solar irradiance modelling: The SOLIS clear-sky module," *Remote Sensing of Environment*, vol. 91, no. 2, pp. 160 – 174, 2004.

[143] A. Ohmura, H. Gilgen, H. Hegner, G. Muller, M. Wild, E. G. Dutton, B. Forgan, C. Freunhlich, R. Philipona, A. Heimo, G. Koenig-Langlo, B. McArthur, R. Pinker, C. H. Whitlock, and K. Dehne, "Baseline surface radiation network (BSRN/WCRP): New precision radiometry for climate research," *Bulletin of the American Meteorological Society*, vol. 79, no. 10, pp. 2115–2136, 1998.

[144] T. Cebecauer, M. Suri, and C. A. Gueymard, "Uncertainty sources in satellite-derived direct normal irradiance: How can prediction accuracy be improved globally?," in *SolarPACES Conference, Granada, Spain*, September 2011.

[145] A. Nottrott and J. Kleissl, "Validation of the NSRDB-SUNY global horizontal irradiance in California," *Solar Energy*, vol. 84, no. 10, pp. 1816 – 1827, 2010.

[146] R. Perez, J. Schlemmer, D. Renne, S. Cowlin, R. George, and B. Bandyopadhyay, "Validation of the SUNY satellite model in a Meteosat environment," in *ASES Annual Conference, Buffalo, New York*, 2009.

[147] R. Posselt, R. Mueller, R. Stckli, and J. Trentmann, "Remote sensing of solar surface radiation for climate monitoring - the CM-SAF retrieval in international comparison," *Remote Sensing of Environment*, vol. 118, no. 0, pp. 186 – 198, 2012.

[148] G. Kinsey, A. Nayak, M. Liu, and V. Garboushian, "Increasing power and energy in Amonix CPV solar power plants," *Photovoltaics, IEEE Journal of*, vol. 1, pp. 213 –218, oct. 2011.

[149] G. S. Kinsey, K. Stone, J. Brown, and V. Garboushian, "Energy prediction of Amonix CPV solar power plants," *Progress in Photovoltaics: Research and Applications*, vol. 19, no. 7, pp. 794–796, 2011.

[150] T. Gerstmaier, S. van Riesen, A. Gombert, A. Mermoud, T. Lejeune, and E. Duminil, "Software modeling of FLATCON CPV systems," *AIP Conference Proceedings*, vol. 1277, no. 1, pp. 183–186, 2010.

[151] F. J. Gomez-Gil, X. Wang, and A. Barnett, "CPV energy production analysis," *AIP Conference Proceedings*, vol. 1407, no. 1, pp. 358–361, 2011.

[152] C. Cameron, C. Crawford, J. Foresi, D. King, R. McConnell, D. Riley, A. Sahm, and J. Stein, "Performance model assessment for multi-junction concentrating photovoltaic systems," *AIP Conference Proceedings*, vol. 1277, no. 1, pp. 290–293, 2010.

[153] M. Steiner, G. Siefer, A. Bosch, T. Hornung, and A. W. Bett, "Realistic power output modeling of CPV modules," *AIP Conference Proceedings*, vol. 1477, no. 1, pp. 309–312, 2012.

[154] R. E. Bird and C. Riordan, "Simple solar spectral model for direct and diffuse irradiance on horizontal and tilted planes at the earth's surface for cloudless atmospheres," *Journal of Climate and Applied Meteorology*, vol. 25, no. 1, pp. 87–97, 1986.

[155] R. E. Bird, C. Riordan, and D. Myers, "Bird simple spectral model: Spctral2." Accessed at http://rredc.nrel.gov/solar/models/spectral/SPCTRAL2/, January 2013.

[156] S. Wilcox, "Completing production of the updated national solar radiation database for the United States," tech. rep., National Renewable Energy Laboratory, 2007.

[157] R. Chen, E. Kang, X. Ji, J. Yang, and J. Wang, "An hourly solar radiation model under actual weather and terrain conditions: A case study in Heihe river basin," *Energy*, vol. 32, no. 7, pp. 1148 – 1157, 2007.

[158] R. P. Tomas Cebecauer, Marcel Suri, “High performance MSG satellite model for operational solar energy applications,” in *ASES Annual Conference, Phoenix, AZ*, 2010.

[159] C. A. Gueymard, “Direct solar transmittance and irradiance predictions with broadband models. part II: validation with high-quality measurements,” *Solar Energy*, vol. 74, no. 5, pp. 381 – 395, 2003.

[160] A. Berk, G. P. Anderson, P. K. Acharya, L. S. Bernstein, L. Muratov, J. Lee, M. Fox, S. M. Adler-Golden, J. H. Chetwynd, M. L. Hoke, R. B. Lockwood, J. A. Gardner, T. W. Cooley, C. C. Borel, and P. E. Lewis, “MODTRAN 5: a reformulated atmospheric band model with auxiliary species and practical multiple scattering options: update,” pp. 662–667, 2005.

[161] C. A. Gueymard, “Prediction and validation of cloudless shortwave solar spectra incident on horizontal, tilted, or tracking surfaces,” *Solar Energy*, vol. 82, no. 3, pp. 260 – 271, 2008.

[162] D. Kaskaoutis and H. Kambezidis, “The role of aerosol models of the smarts code in predicting the spectral direct-beam irradiance in an urban area,” *Renewable Energy*, vol. 33, no. 7, pp. 1532 – 1543, 2008.

[163] C. A. Gueymard, “Clear-sky irradiance predictions for solar resource mapping and large-scale applications: Improved validation methodology and detailed performance analysis of 18 broadband radiative models,” *Solar Energy*, vol. 86, no. 8, pp. 2145 – 2169, 2012.

[164] C. A. Gueymard, “Rest2: High-performance solar radiation model for cloudless-sky irradiance, illuminance, and photosynthetically active radiation validation with a benchmark dataset,” *Solar Energy*, vol. 82, no. 3, pp. 272 – 285, 2008.

[165] V. Lyubansky, “Meteorological synoptical observations from station Sede Boqer (2012-01).”

[166] B. N. Holben, T. F. Eck, I. Slutsker, D. Tanr, J. P. Buis, A. Setzer, E. Vermote, J. A. Reagan, Y. J. Kaufman, T. Nakajima, F. Lavenu, I. Jankowiak, and A. Smirnov, “AERONET-A Federated Instrument

Network and Data Archive for Aerosol Characterization," *Remote Sensing of Environment*, vol. 66, pp. 1–16, 1998.

[167] A. Smirnov, B. Holben, T. Eck, O. Dubovik, and I. Slutsker, "Cloud-screening and quality control algorithms for the AERONET database," *Remote Sensing of Environment*, vol. 73, no. 3, pp. 337 – 349, 2000.

[168] M. Victoria, C. Domínguez, I. Antón, and G. Sala, "Comparative analysis of different secondary optical elements for aspheric primary lenses," *Opt. Express*, vol. 17, pp. 6487–6492, Apr 2009.

[169] M. Buljan, P. Benitez Gimenez, J. C. Minano Dominguez, and R. Mohedano del Pozo, "Improving performances of fresnel CPV system: Fresnel-RXI Köhler concentrator," in *Proceedings of the 25th European Photovoltaic Solar Energy Conference and Exhibition / 5th World Conference on Photovoltaic Energy Conversion*, September 2010.

[170] T. F. Eck, B. N. Holben, J. S. Reid, O. Dubovik, A. Smirnov, N. T. O'Neill, I. Slutsker, and S. Kinne, "Wavelength dependence of the optical depth of biomass burning, urban, and desert dust aerosols," *Journal of Geophysical Research: Atmospheres*, vol. 104, no. D24, pp. 31333–31349, 1999.

[171] National Renewable Energy Laboratory, "Solar radiation research laboratory."

[172] T. Takamura and T. Nakajima, "Overview of SKYNET and its activities," *Opt. Pura Apl*, vol. 37, no. 3, pp. 3303–3308, 2004.

[173] P. T. Landsberg, "Non-radiative transitions in semiconductors," *physica status solidi (b)*, vol. 41, no. 2, pp. 457–489, 1970.

[174] G. Letay and A. Bett, "EtaOpt - a program for calculating limiting efficiency and optimum bandgap structure for multi-bandgap solar cells and tpv cells.," in *17th European Photovoltaic Solar Energy Conference*, 2001.

[175] R. R. King, D. Bhusari, A. Boca, D. Larrabee, X.-Q. Liu, W. Hong, C. M. Fetzer, D. C. Law, and N. H. Karam, "Band gap-voltage offset

and energy production in next-generation multijunction solar cells," *Progress in Photovoltaics: Research and Applications*, vol. 19, no. 7, pp. 797–812, 2011.

[176] J. C. Fan, "Theoretical temperature dependence of solar cell parameters," *Solar Cells*, vol. 17, no. 2-3, pp. 309 – 315, 1986.

[177] A. Marti and G. L. Araujo, "Limiting efficiencies for photovoltaic energy conversion in multigap systems," *Solar Energy Materials and Solar Cells*, vol. 43, no. 2, pp. 203 – 222, 1996.

[178] A. S. Brown and M. A. Green, "Limiting efficiency for current-constrained two-terminal tandem cell stacks," *Progress in Photovoltaics: Research and Applications*, vol. 10, no. 5, pp. 299–307, 2002.

[179] K. Nishioka, T. Sueto, M. Uchida, and Y. Ota, "Detailed analysis of temperature characteristics of an InGaP/InGaAs/Ge triple-junction solar cell," *Journal of Electronic Materials*, vol. 39, pp. 704–708, 2010.

[180] P. Wurfel, "The chemical potential of radiation," *Journal of Physics C: Solid State Physics*, vol. 15, no. 18, p. 3967, 1982.

[181] M. Gonzalez, N. Chan, N. J. Ekins-Daukes, J. G. J. Adams, P. Stavrinou, I. Vurgaftman, J. R. Meyer, J. Abell, R. J. Walters, C. D. Cress, and P. P. Jenkins, "Modeling and analysis of multijunction solar cells," pp. 79330R–79330R–12, 2011.

[182] S. Tobin, S. Vernon, C. Bajgar, S. Wojtczuk, M. Melloch, A. Keshavarzi, T. Stellwag, S. Venkatensan, M. Lundstrom, and K. Emery, "Assessment of MOCVD- and MBE-growth GaAs for high-efficiency solar cell applications," *Electron Devices, IEEE Transactions on*, vol. 37, pp. 469 –477, feb 1990.

[183] S. Wojtczuk, P. Chiu, X. Zhang, D. Pulver, C. Harris, and B. Siskavich, "42% 500x bi-facial growth concentrator cells," *AIP Conference Proceedings*, vol. 1407, no. 1, pp. 9–12, 2011.

[184] A. L. Gray, M. Stan, T. Varghese, A. Korostyshevsky, J. Doman, A. Sandoval, J. Hills, C. Griego, M. Turner, P. Sharps, A. Haas,

J. Wilcox, J. Gray, and R. Schwartz, "Multi-terminal dual junction InGaP2/GaAs solar cells for hybrid system," in *Photovoltaic Specialists Conference, 2008. PVSC '08. 33rd IEEE*, pp. 1 –4, may 2008.

[185] T. Agui, T. Takamoto, and M. Kaneiwa, "Investigation on AlInGaP solar cells for current matched multijunction cells," in *Photovoltaic Energy Conversion, 2003. Proceedings of 3rd World Conference on*, vol. 1, pp. 670 –672 Vol.1, may 2003.

[186] A. B. Cornfeld, M. Stan, T. Varghese, J. Diaz, A. Ley, B. Cho, A. Korostyshevsky, D. J. Aiken, and P. R. Sharps, "Development of a large area inverted metamorphic multi-junction (IMM) highly efficient AM0 solar cell," in *Photovoltaic Specialists Conference, 2008. PVSC '08. 33rd IEEE*, pp. 1 –5, may 2008.

[187] Y.-A. Chang, Z.-Y. Li, H.-C. Kuo, T.-C. Lu, S.-F. Yang, L.-W. Lai, L.-H. Lai, and S.-C. Wang, "Efficiency improvement of single-junction InGaP solar cells fabricated by a novel micro-hole array surface texture process," *Semiconductor Science and Technology*, vol. 24, no. 8, p. 085007, 2009.

[188] T. Takamoto, E. Ikeda, H. Kurita, and M. Ohmori, "High efficiency InGaP solar cells for InGaP/GaAs tandem cell application," in *Photovoltaic Energy Conversion, 1994., Conference Record of the Twenty Fourth. IEEE Photovoltaic Specialists Conference - 1994, 1994 IEEE First World Conference on*, vol. 2, pp. 1729 –1732 vol.2, dec 1994.

[189] G. J. Bauhuis, P. Mulder, and J. J. Schermer, "High efficiency thin film GaAs solar cells with improved radiation hardness," *Photovoltaic Solar*, 2005.

[190] D. M. Wilt, N. S. Fatemi, J. Richard W. Hoffman, P. P. Jenkins, D. J. Brinker, D. Scheiman, R. Lowe, M. Fauer, and R. K. Jain, "High efficiency indium gallium arsenide photovoltaic devices for thermophotovoltaic power systems," *Applied Physics Letters*, vol. 64, no. 18, pp. 2415–2417, 1994.

[191] B. Chung, H. C. Hamaker, G. F. Virshup, and J. G. Werthen, "15% efficiency (1 sun, air mass 1.5), large-area, 1.93 ev $\mathrm{Al}_x\mathrm{Ga}_{1-x}\mathrm{As}$ (x=0.37)

n-p solar cell grown by metalorganic vapor phase epitaxy," *Applied Physics Letters*, vol. 52, pp. 631 –633, feb 1988.

[192] P. Patel, D. Aiken, A. Boca, B. Cho, D. Chumney, M. B. Clevenger, A. Cornfeld, N. Fatemi, Y. Lin, J. McCarty, F. Newman, P. Sharps, J. Spann, M. Stan, J. Steinfeld, C. Tourino, and T. Varghese, "Performance improvement and radiation hardening of inverted metamorphic multi-junction solar cells," in *Photovoltaic Specialists Conference (PVSC), 2011 37th IEEE*, June 2011.

[193] J. D. Mccambridge, M. A. Steiner, B. L. Unger, K. A. Emery, E. L. Christensen, M. W. Wanlass, A. L. Gray, L. Takacs, R. Buelow, T. A. Mccollum, J. W. Ashmead, G. R. Schmidt, A. W. Haas, J. R. Wilcox, J. Van Meter, J. L. Gray, D. T. Moore, A. M. Barnett, and R. J. Schwartz, "Compact spectrum splitting photovoltaic module with high efficiency," *Progress in Photovoltaics: Research and Applications*, vol. 19, pp. 352–360, Sept. 2010.

[194] P. Chiu, S. Wojtczuk, X. Zhang, C. Harris, D. Pulver, and M. Timmons, "42.3% efficient InGaP/GaAs/InGaAs concentrators using bifacial epigrowth," in *Photovoltaic Specialists Conference (PVSC), 2011 37th IEEE*, pp. 000771 –000774, June 2011.

[195] T. Takamoto, E. Ikeda, H. Kurita, and M. Ohmori, "Over 30% efficient InGaP/GaAs tandem solar cells," *Applied Physics Letters*, vol. 70, no. 3, pp. 381–383, 1997.

[196] J. Boisvert, D. Law, R. King, D. Bhusari, X. Liu, A. Zakaria, W. Hong, S. Mesropian, D. Larrabee, R. Woo, A. Boca, K. Edmondson, D. Krut, D. Peterson, K. Rouhani, B. Benedikt, and N. Karam, "Development of advanced space solar cells at Spectrolab," in *Photovoltaic Specialists Conference (PVSC), 2010 35th IEEE*, pp. 000123 –000127, june 2010.

[197] A. D. Vos, "Detailed balance limit of the efficiency of tandem solar cells," *Journal of Physics D: Applied Physics*, vol. 13, no. 5, p. 839, 1980.

[198] J. R. Wilcox, A. W. Haas, J. L. Gray, and R. J. Schwartz, "Estimating saturation current based on junction temperature and bandgap," *AIP Conference Proceedings*, vol. 1407, no. 1, pp. 30–33, 2011.

[199] R. King, A. Boca, W. Hong, X.-Q. Liu, D. Bhusari, D. Larrabee, K. Edmondson, D. Law, C. Fetzer, S. Mesropian, and N. Karam, "Band-gap-engineered architectures for high-efficiency multijunction concentrator solar cells," in *24th European Photovoltaic Solar Energy Conference, Hamburg, Germany*, September 2009.

[200] D. L. King, J. A. Kratochvil, and W. E. Boyson, *Photovoltaic array performance model.* United States. Department of Energy, 2004.

[201] W. D. Soto, S. Klein, and W. Beckman, "Improvement and validation of a model for photovoltaic array performance," *Solar Energy*, vol. 80, no. 1, pp. 78 – 88, 2006.

[202] A. Mermoud and T. Lejeune, "Performance assessment of a simulation model for PV modules of any available technology," in *25th European Photovoltaic Solar Energy Conference and Exhibition / 5th World Conference on Photovoltaic Energy Conversion, Valencia, Spain*, September 2010.

[203] M. Šúri, T. Cebecauer, and A. Skoczek, "SolarGIS: solar data and online applications for PV planning and performance assessment," in *Proceeding of the EUPVSEC 2011 Conference, Hamburg, Germany*, 2011.

[204] M. Suri, T. Huld, E. Dunlop, and T. Cebecauer, "Geographic aspects of photovoltaics in europe: contribution of the PVGIS website," *Selected Topics in Applied Earth Observations and Remote Sensing, IEEE Journal of*, vol. 1, no. 1, pp. 34–41, 2008.

[205] R. M. Swanson, "The promise of concentrators," *Progress in Photovoltaics: Research and Applications*, vol. 8, no. 1, pp. 93–111, 2000.

[206] P. Faine, S. R. Kurtz, C. Riordan, and J. Olson, "The influence of spectral solar irradiance variations on the performance of selected single-junction and multijunction solar cells," *Solar Cells*, vol. 31, no. 3, pp. 259 – 278, 1991.

[207] S. Kurtz, D. Myers, and J. Olson, "Projected performance of three- and four-junction devices using GaAs and GaInP," in *Photovoltaic*

Specialists Conference, 1997., Conference Record of the Twenty-Sixth IEEE, pp. 875 –878, sep-3 oct 1997.

[208] W. McMahon, S. Kurtz, K. Emery, and M. Young, “Criteria for the design of GaInP/GaAs/Ge triple-junction cells to optimize their performance outdoors,” in *Photovoltaic Specialists Conference, 2002. Conference Record of the Twenty-Ninth IEEE*, pp. 931 – 934, may 2002.

[209] M. Muller, B. Marion, S. Kurtz, and J. Rodriguez, “An investigation into spectral parameters as they impact CPV module performance,” *AIP Conference Proceedings*, vol. 1277, no. 1, pp. 307–311, 2010.

[210] G. Letay, C. Baur, and A. W. Bett, “Theoretical investigations of III-V multi-junction concentrator cells under realistic spectral conditions,” in *19th European Photovoltaic Solar Energy Conference, Paris, France*, pp. 4–8, June 2011.

[211] S. Philipps, G. Peharz, R. Hoheisel, T. Hornung, N. Al-Abbadi, F. Dimroth, and A. Bett, “Energy harvesting efficiency of III-V triple-junction concentrator solar cells under realistic spectral conditions,” *Solar Energy Materials and Solar Cells*, vol. 94, no. 5, pp. 869 – 877, 2010.

[212] A. L. Dobbin, M. P. Lumb, and T. N. D. Tibbits, “How important is the resolution of atmospheric data in calculations of spectral irradiance and energy yield for (III-V) triple-junction cells?,” *AIP Conference Proceedings*, vol. 1277, no. 1, pp. 303–306, 2010.

[213] K. Araki and M. Yamaguchi, “Influences of spectrum change to 3-junction concentrator cells,” *Solar Energy Materials and Solar Cells*, vol. 75, no. 3-4, pp. 707 – 714, 2003. PVSEC 12, PART III.

[214] G. S. Kinsey and K. M. Edmondson, “Spectral response and energy output of concentrator multijunction solar cells,” *Progress in Photovoltaics: Research and Applications*, vol. 17, no. 5, pp. 279–288, 2009.

[215] P. Verlinden and J. Lasich, “Energy rating of concentrator PV systems using multi-junction III-V solar cells,” in *Photovoltaic Specialists Conference, 2008. PVSC ’08. 33rd IEEE*, pp. 1 –6, may 2008.

[216] M. Muller, B. Marion, J. Rodriguez, and S. Kurtz, "Minimizing variation in outdoor CPV power ratings," in *7th International Conference on Concentrating Photovoltaic Systems (CPV-7)*, April 2011.

[217] K. Emery, D. Myers, and S. Kurtz, "What is the appropriate reference spectrum for characterizing concentrator cells?," in *Photovoltaic Specialists Conference, 2002. Conference Record of the Twenty-Ninth IEEE*, pp. 840–843, May.

[218] P. Gilman, N. Blair, M. Mehos, C. Christensen, S. Janzou, and C. Cameron, *Solar advisor model user guide for version 2.0.* National Renewable Energy Laboratory, 2008.

[219] C. P. Cameron, W. E. Boyson, and D. M. Riley, "Comparison of PV system performance-model predictions with measured PV system performance," in *Photovoltaic Specialists Conference, 2008. PVSC'08. 33rd IEEE*, pp. 1–6, IEEE, 2008.

[220] F. Rubio, M. Martinez, J. Perea, D. Sanchez, and P. Banda, "Comparison of the different CPV rating procedures: Real measurements in ISFOC," in *Photovoltaic Specialists Conference (PVSC), 2009 34th IEEE*, pp. 000800–000805, IEEE, 2009.

[221] L. Fraas and L. Partain, *Solar Cells and Their Applications.* Wiley Series in Microwave and Optical Engineering, Wiley, 2010.

[222] National Renewable Energy Laboratory, "National solar radiation database - 1991- 2010 update: Typical meteorological year 3."

[223] T. Gerstmaier, M. Gomez, A. Gombert, A. Mermoud, and T. Lejeune, "Validation of the PVSyst performance model for the Concentrix CPV technology," *AIP Conference Proceedings*, vol. 1407, no. 1, pp. 366–369, 2011.

[224] Y. Kemmoku, K. Araki, *et al.*, "Examination of the output characteristic curve of a 500x concentrator PV system considering seasonal variation of the system characteristic," in *Proc. 22nd European Photovoltaic Solar Energy Conference*, 2007.

[225] H. Lee, N. Ekins-Daukes, K. Araki, Y. Kemmoku, and M. Yamaguchi, "Field test and analysis: the behavior of 3-J concentrator cells under

the control of cell temperature," in *Photovoltaic Specialists Conference, 2005. Conference Record of the Thirty-first IEEE*, pp. 754–757, IEEE, 2005.

[226] J. Garrison, "Estimation of atmospheric precipitable water over australia for application to the division of solar radiation into its direct and diffuse components," *Solar Energy*, vol. 48, no. 2, pp. 89 – 96, 1992.

[227] C. Gueymard, "Analysis of monthly average atmospheric precipitable water and turbidity in Canada and northern United States," *Solar Energy*, vol. 53, no. 1, pp. 57 – 71, 1994.

[228] N. Ekins-Daukes, T. Betts, Y. Kemmoku, K. Araki, H. Lee, R. Gottschalg, M. Boreland, D. Infield, and M. Yamaguchi, "Syracuse-a multi-junction concentrator system computer model," in *Photovoltaic Specialists Conference, 2005. Conference Record of the Thirty-first IEEE*, pp. 651–654, IEEE, 2005.

[229] N. Ekins-Daukes, Y. Kemmoku, K. Araki, T. Betts, R. Gottschalg, D. Infield, and M. Yamaguchi, "The design specification for syracuse; a multi-junction concentrator system computer model," *Power*, vol. 50, p. 100, 1929.

[230] S. Adachi, "GaAs, AlAs, and $\mathrm{Al}_x\mathrm{Ga}_{1-x}\mathrm{As}$@B: Material parameters for use in research and device applications," *Journal of Applied Physics*, vol. 58, no. 3, pp. R1–R29, 1985.

[231] E. D. Palik, *Handbook of optical constants of solids II.* Academic Press, 1991.

[232] Y. Varshni, "Temperature dependence of the energy gap in semiconductors," *Physica*, vol. 34, no. 1, pp. 149 – 154, 1967.

[233] P. Antognetti, G. Massobrio, and G. Massobrio, *Semiconductor device modeling with SPICE.* McGraw-Hill, Inc., 1993.

[234] L. Castaner and S. Silvestre, *Modelling photovoltaic systems using PSpice.* Wiley, 2003.

[235] K. Nishioka, T. Takamoto, T. Agui, M. Kaneiwa, Y. Uraoka, and T. Fuyuki, "Evaluation of InGaP/InGaAs/Ge triple-junction solar cell under concentrated light by simulation program with integrated circuit emphasis," *Japanese journal of applied physics*, vol. 43, p. 882, 2004.

[236] American Society for Testing and Materials, "Tables for terrestrial direct normal solar spectral irradiance tables for air mass 1.5," 1992.

[237] J. J. Michalsky, "The Astronomical Almanac's algorithm for approximate solar position (1950 - 2050)," *Solar Energy*, vol. 40, pp. 227–235, 1988.

[238] G. Peharz, G. Siefer, and A. Bett, "A simple method for quantifying spectral impacts on multi-junction solar cells," *Solar Energy*, vol. 83, no. 9, pp. 1588 – 1598, 2009.

[239] M. Meusel, R. Adelhelm, F. Dimroth, A. Bett, and W. Warta, "Spectral mismatch correction and spectrometric characterization of monolithic III-V multi-junction solar cells," *Progress in Photovoltaics: Research and Applications*, vol. 10, no. 4, pp. 243–255, 2002.

[240] C. Gueymard, "Latitude and climate dependent optimal siting and spectral effects of concentrating pv technologies: Preliminary analysis; CPV Workshop, Marburg," 2007.

[241] S. Ramachandran, R. Rengarajan, A. Jayaraman, M. M. Sarin, and S. K. Das, "Aerosol radiative forcing during clear, hazy, and foggy conditions over a continental polluted location in north india," *Journal of Geophysical Research: Atmospheres*, vol. 111, no. D20, pp. n/a–n/a, 2006.

[242] S. Jade, M. Vijayan, V. Gaur, T. P. Prabhu, and S. Sahu, "Estimates of precipitable water vapour from GPS data over the Indian subcontinent," *Journal of Atmospheric and Solar-Terrestrial Physics*, vol. 67, no. 6, pp. 623 – 635, 2005.

[243] D. A. Chu, Y. J. Kaufman, C. Ichoku, L. A. Remer, D. Tanre, and B. N. Holben, "Validation of MODIS aerosol optical depth retrieval

over land," *Geophysical Research Letters*, vol. 29, no. 12, pp. MOD2–1–MOD2–4, 2002.

[244] National Renewable Energy Laboratory, "India solar resource maps," February 2013.

[245] R. Perez, J. Schlemmer, D. Renne, S. Cowlin, R. George, and B. Bandyopadhyay, "Validation of the SUNY Satellite Model in a Meteosat Environment," in *ASES Annual Conference, Buffalo, New York.*, 2009.

[246] Ministry of New and Renewable Energy, Government of India, "Jawaharlal Nehru National Solar Mission - Towards Building Solar India."

[247] S. B. Darling, F. You, T. Veselka, and A. Velosa, "Assumptions and the levelized cost of energy for photovoltaics," *Energy & Environmental Science*, vol. 4, no. 9, pp. 3133–3139, 2011.

[248] D. Faiman, "The triple sustainability of CPV within the framework of the Raviv Model," in *20th European PV Conference, Barcelona, Spain*, 2005.

[249] K. Branker, M. Pathak, and J. Pearce, "A review of solar photovoltaic levelized cost of electricity," *Renewable and Sustainable Energy Reviews*, 2011.

[250] F. Trieb and H. Müller-Steinhagen, "The DESERTEC Concept-Sustainable Electricity and Water for Europe, Middle East and North Africa," *Whitebook of TREC and Club of Rome-Clean Power from Deserts*, pp. 23–43, 2007.

[251] M. S. Salvadore and J. H. Keppler, "Projected costs of generating electricity: 2010 edition," 2010.

[252] G. Sargsyan, M. Bhatia, S. G. Banerjee, K. Raghunathan, and R. Soni, *Unleashing the potential of renewable energy in India.* World Bank Publications, 2011.

[253] C. Baur, M. Hermle, F. Dimroth, and A. W. Bett, "Effects of optical coupling in III-V multilayer systems," *Applied Physics Letters*, vol. 90, no. 19, p. 192109, 2007.

[254] M. A. Steiner and J. F. Geisz, “Non-linear luminescent coupling in series-connected multijunction solar cells,” *Applied Physics Letters*, vol. 100, no. 25, p. 251106, 2012.

[255] H. Yoon, R. King, G. Kinsey, S. Kurtz, and D. Krut, “Radiative coupling effects in GaInP/GaAs/Ge multijunction solar cells,” in *Photovoltaic Energy Conversion, 2003. Proceedings of 3rd World Conference on*, vol. 1, pp. 745 –748 Vol.1, may 2003.

[256] A. S. Brown and M. A. Green, “Radiative coupling as a means to reduce spectral mismatch in monolithic tandem solar cell stacks theoretical considerations,” in *Photovoltaic Specialists Conference, 2002. Conference Record of the Twenty-Ninth IEEE*, pp. 868–871, IEEE, 2002.

[257] M. Stan, D. Aiken, B. Cho, A. Cornfeld, V. Ley, P. Patel, P. Sharps, and T. Varghese, “High-efficiency quadruple junction solar cells using omvpe with inverted metamorphic device structures,” *Journal of Crystal Growth*, vol. 312, no. 8, pp. 1370 – 1374, 2010. The 17th American Conference on Crystal Growth and Epitaxy/The 14th US Biennial Workshop on Organometallic Vapor Phase Epitaxy/The 6th International Workshop on Modeling in Crystal Growth.